



The
University
Of
Sheffield.

**Formation of ZrCu-based Bulk Metallic Glasses
and Composites with Enhanced Glass Forming
Ability and Mechanical Properties**

MR HAOTIAN NAN

Department of Materials Science and Engineering

This thesis is submitted to the University of Sheffield for the degree of

Doctor of Philosophy, October 2019

Declaration

The work presented in this thesis is that of the Author and has not been submitted for any other award or degree at the University of Sheffield or any other university or institution.

Acknowledgement

First and foremost, I want to express my sincere gratitude to my supervisor Prof. Iain Todd. He has supported me since I am an undergraduate student. He gave me the courage to start my PhD, without his help and guidance I could not have completed this thesis. He has provided freedom and invaluable suggestions throughout my studies. The discussions with him always gave me inspiration and encouragement. I could not have imagined having a better supervisor and really appreciate his contributions.

I would like to thank my second supervisor, Prof. Mark Rainforth for his continuous support, patience, motivation, enthusiasm and advice for my research and life.

I would like to take this opportunity to thank my group members and colleagues, Dr. Junheng Gao who always gives me the advice and guidance not only for my research works but also for my daily life, Dr. Yuhe Huang who always lends me a hand whenever I need his help, and also Dr. Phillip Mahoney, Dr. Yidong Xu, Dr. Dikai Guan, Dr. Jake Corteen, Dr Zhaoyuan Leong, Dr. Norhuda Hidayah Nordin. I am lucky to have such great friends and colleagues during my study.

I would also like to thank the Technical staffs of the Materials Science department, Dr. Le Ma, Neil Hind, Dean Haylock, Dr. Oday Hussein for their training and help.

I am so thankful to my girlfriend for her constant company. She has brought infinite happiness, comfort, support and love to me. She always encouraged me when I encountered

obstacles. She takes good care of every aspect of me. She is the best girlfriend in the world.

I could not imagine my life without her.

Finally, I would like to express the most profound gratitude to my parents for their love, comfort, encouragement and support for my life and studies. My parents are the most important people in my life. They kept me going and they taught me everything. Everything they have given me, I will always keep it inside. I love them forever.

Abstract

Bulk metallic glasses (BMGs) have shown a unique combination of mechanical, chemical, and physical properties, but their room-temperature brittleness has been the stumbling block for real structural applications. To respond to this challenge, the concept of developing composite microstructures by combining the glassy matrix with crystalline phases at different length scales has been developed, through which an improvement in compression and tensile ductility has been obtained in several Zr- and Ti-based BMG composites. However, these BMG composites showed a macroscopic strain-softening phenomenon with an early onset of necking (i.e., the maximum strength occurs at the yield point) because of a lack of work hardening mechanisms (endows the materials with minute damage tolerance), which would give rise to serious engineering problems therefrom. In this thesis, three series of ZrCu-based BMGs and Bulk Metallic Glass Matrix Composites (BMGMCs) were designed which are Zr-Cu-Al-Ag, Zr-Cu-Al-Ag-Ti and Zr-Cu-Al-Nb. All these alloys were prepared and characterised in terms of thermal behaviour, phase formation and mechanical properties.

The $Zr_{50}Cu_{45-x}Al_5Ag_x$ ($x = 0, 0.5, 1$ and 2.0 at. %) alloy systems were designed based on the Zr-Cu-Al BMGMC system. The effect of the Ag element addition to the base alloy system has been studied. It is found that the cooling rate (sample size) strongly affects the phase formation and the mechanical properties of the alloy, exhibiting big differences due to the formation of the brittle phases, the volume fraction and size of the B2-CuZr phase.

By investigating these alloys, it also provides a scope for preparing medium/large-sized single B2-CuZr phase BMGMCs in the following chapters.

In addition, a new series composition of the $Zr_{50-x}Cu_{44}Al_5Ag_1Ti_x$ ($x = 0.5, 1, 2, 3, 4$ and 5 at. %) alloy has been designed based on the Zr-Cu-Al-Ag alloy system. By carefully controlling the Ti content of the alloy compositions, the 6 mm $Zr_{49.5}Cu_{44}Al_5Ag_1Ti_{0.5}$ and $Zr_{49}Cu_{44}Al_5Ag_1Ti_1$ alloys have exhibited good work-hardening ability and plasticity during compression tests. The martensitic transformation from the metastable B2-CuZr phase to the monolithic B19' martensitic phase was observed after the compression tests. The deformation-induced martensitic transformation process leads to a significant improvement of compressive plasticity, with plastic strain of 12.3 % and obvious work hardening behaviour.

Finally, the glass forming ability (GFA), thermal properties, kinetics and mechanical properties of $Zr_{50}Cu_{45-x}Al_5Nb_x$ ($x = 0.2, 0.4, 0.6,$ and 0.8 at. %) BMGs have been investigated. The alloy displayed a significant compressive strain of 7.1 % at room temperature. The results showed that the GFA is enhanced with an increase of Nb content. The plastic strain exhibits a trend of increasing with the Nb content.

The current findings offer a new paradigm for developing BMGMCs with improved ductility for practical engineering materials. These studies and observations provide an understanding of the formation, deformation and microstructural optimisation of the ZrCu-based BMGs and BMGMCs.

Table of Contents

| | |
|--|-----|
| Declaration..... | ii |
| Acknowledgement | iii |
| Abstract..... | v |
| Nomenclature..... | xi |
| List of Tables | xiv |
| List of Figures | xv |
| Chapter 1 Introduction | 1 |
| 1.1 Introduction..... | 1 |
| 1.2 Thesis Outline | 4 |
| Chapter 2 Literature Review..... | 6 |
| 2.1 Introduction to Metallic Glass | 6 |
| 2.2 Theories of Bulk Metallic Glass Formation | 8 |
| 2.2.1 Structure of Bulk Metallic Glasses | 8 |
| 2.2.2 Thermodynamics of Metallic Glass Formation | 11 |
| 2.2.3 Kinetics of Metallic Glass Formation..... | 13 |
| 2.2.4 Alloying Element Effect to the Glass Forming Ability | 14 |
| 2.3 Introduction of Metallic Glass Composites | 18 |
| 2.4 Deformation Behaviour | 25 |
| 2.4.1 Homogeneous and Inhomogeneous Deformation..... | 25 |
| 2.4.2 Shear Band Nucleation and Propagation | 28 |
| 2.5 Methods for Plasticity and Work Hardening Improvement..... | 32 |

| | |
|---|----|
| 2.5.1 Phase separation..... | 32 |
| 2.5.2 Increase in Poisson's ratio | 35 |
| 2.5.3 Phase Transformation Induced Plasticity..... | 37 |
| 2.6 Summary of literature review | 49 |
| Chapter 3 Experimental Methods | 50 |
| 3.1 Materials Preparation | 50 |
| 3.1.1 Alloy Preparation | 50 |
| 3.1.2 Arc Melting..... | 50 |
| 3.1.3 Copper Mould Suction Casting..... | 52 |
| 3.2 Characterisation | 53 |
| 3.2.1 X-Ray Diffraction (XRD)..... | 53 |
| 3.2.2 Thermal Analysis | 54 |
| 3.2.3 Compression Test | 54 |
| 3.2.4 Tensile Test..... | 55 |
| 3.2.5 Scanning Electron Microscopy | 56 |
| 3.2.6 Transmission Electron Microscopy and High-resolution Transmission Electron Microscopy..... | 57 |
| Chapter 4 Experimental Methods Investigation of the Effect of Ag Element to the Zr- Cu-Al Bulk Metallic Glass Composites | 59 |
| 4.1 Introduction..... | 59 |
| 4.2 Experimental Work..... | 61 |
| 4.3 Results and Discussions..... | 62 |

| | | |
|-----------|--|-----|
| 4.3.1 | Microstructure features of as-cast samples | 62 |
| 4.3.2 | Thermal properties of as-cast samples | 66 |
| 4.3.3 | Mechanical properties | 68 |
| 4.4 | Conclusion | 73 |
| | | |
| Chapter 5 | Formation of Zr-Cu-Al-Ag-Ti Bulk Metallic Glass Composites with Enhanced Work-Hardening Ability and Plasticity | 74 |
| 5.1 | Introduction..... | 74 |
| 5.2 | Experimental Work..... | 76 |
| 5.3 | Results and Discussion | 77 |
| 5.3.1 | Microstructures of as-cast samples | 77 |
| 5.3.2 | Thermal properties of as-cast samples | 83 |
| 5.3.3 | Mechanical Properties..... | 88 |
| 5.4 | Conclusion | 99 |
| | | |
| Chapter 6 | The Effect of minor Nb Addition on the Glass-Forming Ability and Mechanical Properties of Zr-Cu-Al-Nb Bulk Metallic Glasses | 100 |
| 6.1 | Introduction..... | 100 |
| 6.2 | Experimental Work..... | 102 |
| 6.3 | Results and Discussions..... | 103 |
| 6.3.1 | Microstructure features of as-cast samples | 103 |
| 6.3.2 | Glass forming ability and thermal stability of as-cast samples | 104 |
| 6.3.2 | Mechanical properties..... | 116 |
| 6.4 | Conclusions..... | 125 |

| | |
|---|-----|
| Chapter 7 Conclusion and Future Works | 126 |
| 7.1 Conclusion | 126 |
| 7.2 Future works | 128 |
| References..... | 129 |

Nomenclature

Acronyms

| | |
|-------|--|
| BMG | Bulk Metallic Glass |
| BMGCs | Bulk Metallic Glass Composites |
| GFA | Glass Forming Ability |
| DSC | Differential Scanning Calorimetry |
| DTA | Differential Thermal Analysis |
| XRD | X-Ray Diffraction |
| SEM | Scanning Electron Microscopy |
| TEM | Transmission Electron Microscopy |
| HRTEM | High Resolution Transmission Electron Microscopy |
| STEM | Scanning Transmission Electron Microscope |
| SAED | Selected Area Diffraction Pattern |
| STZ | Shear Transformation Zone |
| FV | Free Volume |

Symbols

| | |
|-------|---------------|
| B | bulk modulus |
| C | constant |
| C_p | heat capacity |

| | |
|-----------|--|
| d_c | critical casting diameter |
| D | stress concentration factor |
| E | Young's modulus |
| E_g | activation energy of glass transition |
| E_x | activation energy of crystallization |
| E_p | activation energy of peak crystallization |
| f | volume fraction |
| f_0 | frequency of atomic vibration |
| G | shear modulus |
| G^{mix} | Gibbs free energy of the liquid |
| K | thermal conductivity |
| m | fragility parameter |
| n_D | number of jumps required to annihilate a free volume |
| Q | activation energy associated with serration event |
| R | gas constant |

Greek

| | |
|------------|-----------------|
| η | viscosity |
| γ_t | surface tension |
| Ω | atomic volume |
| ρ | density |

| | |
|-------------------------|---|
| ζ | pressure gradient |
| ν | Poisson's ratio |
| ε_c | critical strain rate |
| ε_p | plastic strain |
| ψ | stability parameter |
| χ | geometrical factor between 0.5 and 1 |
| θ_c | shear fracture angle under compression |
| θ_t | shear fracture angle under tension |
| λ_s | particle spacing |
| τ | average structural relaxation time |
| τ_0 | shear stress |
| σ_0 | normal stress |
| σ_f | fracture strength |
| ΔT_x | supercooled liquid region |
| ΔT_s | temperature increase in a single shear band |
| ΔG_m | activation barrier |
| ΔH^{mix} | heat of mixing |

List of Tables

| | |
|---|-----|
| Table 5. 1: Heat of mixing (kJ/mol) for the binary systems of the Zr, Cu, Al, Ag and Ti elements [131]. | 77 |
| Table 5. 2: Thermodynamic properties of $Zr_{50-x}Cu_{44}Al_5Ag_1Ti_x$ ($x=0.5, 1, 2, 3, 4$ and 5 at %) alloys as-cast rods obtained from DSC and DTA..... | 87 |
| Table 6. 1: $T_g, T_x, T_l, T_x, T_{rg}$ and γ values of the $Zr_{50}Cu_{45-x}Al_5Nb_x$ ($x = 0.2, 0.4, 0.6$ and 0.8 at. %) BMG samples at a heating rate of 20 K/min..... | 109 |
| Table 6. 2: The T_g values of the as-cast 2 mm $Zr_{50}Cu_{45-x}Al_5Nb_x$ ($x = 0.2, 0.4, 0.6$ and 0.8 at. %) BMG samples at heating rates of 10 K/min, 20 K/min, 40 K/min and 60 K/min. . | 109 |
| Table 6. 3: The T_x values of the as-cast 2 mm $Zr_{50}Cu_{45-x}Al_5Nb_x$ ($x = 0.2, 0.4, 0.6$ and 0.8 at. %) BMG samples at heating rates of 10 K/min, 20 K/min, 40 K/min and 60 K/min. . | 110 |
| Table 6. 4: The change in enthalpy prior to the glass transition process and the fragility parameter of $Zr_{50}Cu_{45-x}Al_5Nb_x$ ($x = 0.2, 0.4, 0.6$ and 0.8 at. %) BMGs. | 120 |

List of Figures

| | |
|---|----|
| Figure 2. 1: The three cluster models and corresponding arrangements [50]. | 9 |
| Figure 2. 2: The ECP of the FCC structure for the Zr-Cu-Ni-Al bulk metallic glass. (a) and (b) show the {100} and {110} plane view respectively [51]. | 11 |
| Figure 2. 3: The Angell plot of Gibbs free energy variation between the liquid and crystalline state for different glass-forming materials [53]. | 12 |
| Figure 2. 4: The Angell plot of different types of metallic-glass-forming liquids [53]. | 14 |
| Figure 2. 5: Classified BMGMCs manufacture processes [73]. | 19 |
| Figure 2. 6: Tensile test of Ti-Zr-Be-V-Cu and Ti-Zr-Be-V-Cu-Be alloy system. (A) The room temperature tensile test strength-strain curve for 6 different compositions compared with commercial pure titanium and Ti-6Al-4V alloy. (B) The necking image of Ti-6Al-4V and commercial pure titanium. (C) Shear band morphology of one test sample. (D) Necking SEM images of test samples (E) The corresponding microstructure of necking images [82]. | 24 |
| Figure 2. 7: Schematic of the shear transformation zone [3]. | 26 |
| Figure 2. 8: Effect of the composition of the Zr-Cu-Ni-Al system to Poisson's ratio and Young's modulus [85]. | 30 |
| Figure 2. 9: (a) BF- TEM micrograph showing a typical microstructure formed by phase separation in as-melt spun alloy, (b) Corresponding SAED pattern showing double halo rings, and (c) DF-TEM micrograph obtained using inner diffuse halo ring marked in (b). | 35 |
| Figure 2. 10: The Correlation between the Poisson's ratio and the fragility index [104]. | 37 |
| Figure 2. 11: The transformation process of (a) The Crystal structure of B2-CuZr to (b) B19'-CuZr martensitic structure [107]. | 38 |

Figure 2. 12: (a) The TEM images of deformed $\text{Cu}_{47.5}\text{Zr}_{47.5}\text{Al}_5$ alloy with typical twins contrast. (b) HRTEM images of the lattice planes, the twins and B2 CuZr phase were examined. The inset shows the corresponding SADP patterns of the twins and B2 phase. 40

Figure 2. 13: The deformation process in the CuZr based alloy systems. (a) The glassy matrix is shown in blue and the local stress concentrations shown in red to yellow will generate at the beginning of loading. (b) A variety of nanocrystal morphologies are formed due to stress. The STZs start to develop in this region at the same time and are blocked by the nanocrystals. (C) The STZs will band together to form a nascent shear band which will absorb the stress and hinder the fracture propagation.....40

Figure 2. 14: (a) The SEM image of tensile test sample, (b) Martensite phase after the TRIP process, (c) Tensile engineering stress-strain curve for different stress conditions, inset shows the true stress-strain curve [106].42

Figure 2. 15: The tensile test curves and SEM images of TRIP reinforced BMGMCs and bcc dendrite reinforced BMGMCs [22].42

Figure 2. 16: The microstructure changes with different Al content and diameters [110].44

Figure 2. 17: The B2-CuZr phase stacking fault energy dependence of the electronegativity and atomic radius difference with different alloying elements [84]......46

Figure 2. 18: The schematic of the heterogeneous nucleation process for developing large-sized BMGMCs. (a) The suitable alloying elements have increased the GFA of the matrix. (b) The alloying elements will form intermetallic with the main elements due to the decrease in temperature. (c) The high melting point intermetallic will contribute to the formation of the homogeneous distributed metastable phase. (d) The remaining molten materials will form the amorphous matrix [113]......47

Figure 3. 1: (a) MAM1 arc melter configurations for melting. (b) Melting mould.....51

Figure 3. 2: (a) MAM1 arc melter configurations for casting. (b) Casting mould.....52

| | |
|--|----|
| Figure 3. 3: Tensile test specimen. | 56 |
| Figure 4. 1: XRD patterns of the as-cast $Zr_{50}Cu_{45-x}Al_5Ag_x$ ($x = 0, 0.5, 1, \text{ and } 2$ at. %) alloys with different cooling rate (sample size): (a) $x = 0$, (b) $x = 0.5$ (c) $x = 1$, (d) $x = 2$ | 65 |
| Figure 4. 2: Microstructure variations with Ag content and sample size (cooling rate) of $Zr_{50}Cu_{45-x}Al_5Ag_x$ ($x = 0, 0.5, 1, \text{ and } 2$ at. %) alloy system..... | 66 |
| Figure 4. 3: DSC curves of the as-cast $Zr_{50}Cu_{45-x}Al_5Ag_x$ ($x = 0, 0.5, 1, \text{ and } 2$ at. %) alloy system. | 68 |
| Figure 4. 4: Room-temperature compression test curves of as-cast 2 mm $Zr_{50}Cu_{45}Al_5$ base alloy and 2–6 mm $Zr_{50}Cu_{44}Al_5Ag_1$ alloys..... | 70 |
| Figure 4. 5: SEM images of the as-cast (a) 3 mm (b) 4 mm (c) 5 mm $Zr_{50}Cu_{44}Al_5Ag_1$ BMGMCs. | 72 |
| Figure 5. 1: XRD patterns of as-cast 3 mm $Zr_{50-x}Cu_{44}Al_5Ag_1Ti_x$ ($x=0.5, 1, 2, 3, 4$ and 5 at %) alloys..... | 79 |
| Figure 5. 2: XRD patterns of as-cast 6 mm $Zr_{50-x}Cu_{44}Al_5Ag_1Ti_x$ ($x=0.5, 1, 2, 3, 4$ and 5 at %) alloys..... | 79 |
| Figure 5. 3: (a) The HRTEM images of the as-cast 3 mm $Zr_{49}Cu_{44}Al_5Ag_1Ti_1$ sample with lattice feature marked by yellow circles. (b) The enlarged area of the lattice structure and the corresponding SAED. | 80 |
| Figure 5. 4: (a) The BF-TEM image of the B2-CuZr phase embedded on the amorphous matrix. (b) HR-TEM micrograph of as-cast 6 mm Ti_1 alloy, shows the interface between the amorphous matrix and crystalline B2-CuZr phase. (c) The HR-TEM image of the B2-CuZr phase. The inset shows the SAED pattern of B2-CuZr phase taken from zone-axis $[1\ 1\ 0]$. (d) SEM image of the B2-CuZr particles and the amorphous matrix. | 82 |

| | |
|---|-----|
| Figure 5. 5: DSC trace of as-cast $Zr_{50-x}Cu_{44}Al_5Ag_1Ti_x$ ($x=0.5, 1, 2, 3, 4$ and 5 at %) specimens. | 84 |
| Figure 5. 6: DTA trace of as-cast $Zr_{50-x}Cu_{44}Al_5Ag_1Ti_x$ ($x=1, 2, 3, 4$ and 5 at %) specimens. | 87 |
| Figure 5. 7: True stress-strain compression curve of the 6 mm $Zr_{50-x}Cu_{44}Al_5Ag_1Ti_x$ ($x=0.5, 1, 2, 3, 4$ and 5 at %) alloys. | 89 |
| Figure 5. 8: (a)-(f) SEM images of fracture surfaces for all the 6 mm specimens from $Ti_{0.5}$ to Ti_5 | 91 |
| Figure 5. 9: SEM images of the longitudinal surface of the deformed 6 mm (a) $Ti_{0.5}$ (b) Ti_1 specimens. Large shear bands aggregations are observed..... | 92 |
| Figure 5. 10: (a) TEM images of the deformed 6 mm Ti_1 samples after the compression tests. (b) The HRTEM image of the B19' martensitic phase. | 94 |
| Figure 5. 11: (a) and (b) The nano-sized B2-CuZr crystalline phases with twinning feature. | 94 |
| Figure 5. 12: Tensile test stress-strain curve of the 3 mm and 6 mm Ti_1 sample..... | 97 |
| Figure 5. 13: (a)–(b) SEM images of 6 mm Ti_1 sample fracture surface after the tensile tests. The ‘block effect’ due to the B2-CuZr phase is observed. The alloy presents ductile features after the tensile tests. | 98 |
| Figure 6. 1: XRD patterns of the as-cast $Zr_{50}Cu_{45-x}Al_5Nb_x$ ($x = 0.2, 0.4, 0.6$ and 0.8 at. %) alloys..... | 104 |
| Figure 6. 2: DSC curves of the as-cast 2 mm $Zr_{50}Cu_{45-x}Al_5Nb_x$ ($x = 0.2, 0.4, 0.6$ and 0.8 at. %) BMG samples, (a) $Nb_{0.2}$, (b) $Nb_{0.4}$ (c) $Nb_{0.6}$ and (d) $Nb_{0.8}$ at heating rates of 10 K/min, 20 K/min, 40 K/min and 60 K/min respectively. | 106 |

| | |
|---|-----|
| Figure 6. 3: DTA curves of the as-cast 2 mm $Zr_{50}Cu_{45-x}Al_5Nb_x$ ($x = 0.2, 0.4, 0.6$ and 0.8 at. %) BMG samples..... | 107 |
| Figure 6. 4: The Kissinger plots of $Zr_{50}Cu_{45-x}Al_5Nb_x$ ($x = 0.2, 0.4, 0.6$ and 0.8 at. %) BMG samples at temperature (a) T_g (b) T_x | 111 |
| Figure 6. 5: The Ozawa plots of $Zr_{50}Cu_{45-x}Al_5Nb_x$ ($x = 0.2, 0.4, 0.6$ and 0.8 at. %) BMG samples at temperature (a) T_g (b) T_x | 113 |
| Figure 6. 6: The compressive stress-strain curves of $Zr_{50}Cu_{45-x}Al_5Nb_x$ ($x = 0.2, 0.4, 0.6$ and 0.8 at. %) BMGs..... | 116 |
| Figure 6. 7: SEM images of the fracture surfaces of the (a) $Zr_{50}Cu_{44.8}Al_5Nb_{0.2}$, (b) $Zr_{50}Cu_{44.6}Al_5Nb_{0.4}$, (c) $Zr_{50}Cu_{44.4}Al_5Nb_{0.6}$, (d)-(f) $Zr_{50}Cu_{44.2}Al_5Nb_{0.8}$ | 118 |
| Figure 6. 8: HRTEM images of the as-cast $Zr_{50}Cu_{44.2}Al_5Nb_{0.8}$ alloys with corresponding SAED..... | 119 |
| Figure 6. 9: Correlation of plasticity with (a) change in enthalpy prior to the glass transition process (b) fragility parameter of $Zr_{50}Cu_{45-x}Al_5Nb_x$ ($x = 0.2, 0.4, 0.6$ and 0.8 at. %) BMGs. | 122 |
| Figure 6. 10: The tensile test stress-strain curves of $Zr_{50}Cu_{45-x}Al_5Nb_x$ ($x = 0.2, 0.4, 0.6$ and 0.8 at. %) BMGs..... | 124 |

Chapter 1

Introduction

1.1 Introduction

Since the discovery of the first Bulk Metallic Glasses (BMGs), these materials have attracted much scientific interest and commercial attention [1]–[3]. BMGs exhibit excellent properties such as high strength, high elastic limits, high hardness and good corrosion and wear resistance, which are certainly desirable properties for real-life applications [2], [4]–[6]. These advantages provide them the potential for high-performance engineering and structural applications. These unique materials can be fabricated by solidification of liquid alloys with sufficiently high cooling rates, which will inhibit the nucleation and growth of the crystalline phases.

Various BMG systems have been successfully developed such as Mg- [7], Pd- [8], Ti- [9], Fe- [10], Al- [11], Ca- [12], Zr- [13], La- [14] and Cu-based systems [15]. Among these BMGs, ZrCu-based BMGs are currently well recognised due to their enhanced glass forming ability (GFA) and mechanical properties [13], [16]–[18]. However, along with the development of BMGs, some disadvantages have strongly hindered the wider application of BMGs in engineering and structural applications. The drawbacks of BMGs are room temperature brittleness under deformation and strain-softening behaviour [2][19]. In order to overcome these problems, several concepts have been introduced: (a) increase in the

Poisson's ratio of the alloy systems [20], (b) chemical and microstructural inhomogeneity such as phase separation or in-situ formation of Bulk Metallic Glasses Matrix Composites (BMGMCs) [21]–[23], (c) control of the sample size and cooling rate effect of the alloys [24]–[26] (d) ex-situ introduction of the second phase into the BMG matrix and formation BMGMCs [27]–[29] Methods (a) and (b) are based on the intrinsic properties of BMGs and (c) and (d) are generally controlled by external factors.

Forming BMGMCs has been proven to be an effective way to improve mechanical properties among the methods mentioned above. BMGMCs are formed based on the glassy matrix and combined with different reinforcement materials or second phase particles. During the development of BMGMCs, they have presented a lot of advantages compared with the traditional BMGs such as enhanced room-temperature compressive plasticity. The combination of multiple phases and glassy matrix contribute to changes in microstructure features after deformation, which significantly improves the mechanical performance of BMGs. The main drawbacks for the current BMGMCs are strain softening and early necking [30]. In order to solve these problems, a new concept of transformation-induced plasticity (TRIP) reinforced BMGMCs has been introduced [22], [31], [32]. According to recent research, the TRIP method has been introduced into Ti-based and ZrCu-based BMGMCS. These alloy systems can form a metastable crystalline phase during the fast cooling process and can be transformed into a martensitic phase during the plastic transformation process. This method has intensively improved the compressive plasticity, tensile ductility and work-

hardening behaviour during deformation. However, the main problems for the current TRIP reinforced BMGMCs is that they cannot form large-sized samples because the microstructure is very sensitive to cooling rate and alloy compositions. The GFA, dimensions and volume fraction of the metastable phase in the glassy matrix should also be carefully controlled [33]. An alloy system should be carefully designed and tested to fulfil these requirements.

Current works are established on the ZrCu-based BMGs and BMGMCs. Three alloy systems, namely Zr-Cu-Al-Ag, Zr-Cu-Al-Ag-Ti and Zr-Cu-Al-Nb have been designed and studied, mainly focusing on the microstructure, GFAs and formation mechanisms. The aim of this thesis is to get a better knowledge of the ZrCu-based BMGs and BMGMCs by investigating the relationship between the microstructure, alloy composition, sample size and mechanical properties. New alloy systems with enhanced plasticity and sample size mechanical properties will be designed. A detailed thesis outline of each chapter is given below.

The objectives of this thesis are: 1. Design new TRIP reinforced Zr-Cu-Al-based BMGMCs; 2. Increase the sample size of the new alloy system. 3. Investigate the glass forming ability and mechanical properties of the alloys. 4. Investigate the alloying element effect to the alloy system.

1.2 Thesis Outline

This thesis is composed of seven chapters which mainly study the ZrCu-based BMGs and BMGMCs

Chapter 2 provides a literature review of BMGs and BMGMCs, including the formation mechanisms, structural nature and mechanical properties of BMGs and BMGMCs. Methods which enhance and improve the mechanical performance of the BMGs and BMGMCs are also introduced.

Chapter 3 presents detailed experimental methods.

Chapter 4 introduces the Ag element to the Zr-Cu-Al BMGMC system. The microstructures, GFAs and mechanical properties are carefully examined for the alloy systems. The sample size and cooling rate effect to the alloy systems are studied and provide a scope for Chapter 5.

Chapter 5 investigates the effect of the Ti element on the Zr-Cu-Al-Ag alloy systems by replacing the Zr content. Large-sized single B2-CuZr phase BMGMCs with enhanced plasticity and work-hardening property are fabricated. The microstructure details are also investigated.

Chapter 6 investigates the effect of minor Nb addition to the Zr-Cu-Al BMGs systems. The GFAs of the alloy systems are assessed. The mechanical properties and deformation mechanisms are also studied.

Chapter 7 presents an overall conclusion and lists the main findings of the thesis, as well as giving suggestions for future work.

Chapter 2

Literature Review

2.1 Introduction to Metallic Glass

Traditional metallic materials are commonly formed by their constituent atoms having an ordered crystalline structure. When the solid materials exhibit random atomic arrangement, this is referred to as an amorphous or glassy structure. It is also known that when the molten liquid is undercooled into a solid, with sufficiently high cooling rates, the nucleation of the crystalline phase is limited [2]. Using these theories, scientists have started to investigate ways and methods of making amorphous alloys. The Duwez group applied the rapid quenching technique with a very high cooling rate (approximately 10^6 K/s), successfully making the amorphous structure $\text{Au}_{75}\text{Si}_{25}$ alloy in the 1960s, which was the first metallic glass (MG) [34]. Following the discovery of this alloy, researchers started to focus on making ribbon and foil shaped MGs. Pond et al. have made MG foils that are meters long using the rolling method [35], and Turnbull's group have introduced a concept to assess the Glass Forming Ability (GFA) of MGs based on classical nucleation theory and experiments [26]. They indicated that when the Reduced Glass Transition Temperature (T_{rg}), the ratio between the Glass Transition Temperature (T_g) and Melting Temperature (T_m), is $1/2$, the nucleation rate will reach $10^6 \text{ cm}^{-3} \text{ s}^{-1}$ and the glass formation becomes difficult. When $T_{rg} > 2/3$, the nucleation rate is $10^{-30} \text{ cm}^{-3} \text{ s}^{-1}$, and under a proper cooling rate the MGs can be formed. When $T_{rg} = 1$, the crystallisation will never occur.

The commercial casting manufacturing process has driven the rapid development of metallic glasses, and MG films with thicknesses under 50 μm can be fabricated [36][2]. Further investigations of metallic glasses revealed more compositions. However, the ribbon, foil and film-shaped MGs have limited MG developments in structural applications. The demands of obtaining large-sized MGs for real-life applications became very popular. The term Bulk Metallic Glasses (BMGs) has been defined by scientists as MGs with diameter or section thickness over millimetres. The $\text{Pd}_{77.5}\text{Cu}_6\text{Si}_{16.5}$ rod-shaped BMGs were developed by Chen et al. with a cooling rate of 10^3 K/s in 1974 [37]. A year later they discovered Pt-Ni-P and Au-Si-Ge BMG systems [38] [39]. In the early 1980s, Turnbull *et al.* fabricated centimetre sized Pd-Ni-P BMGs using boron oxide to purify the molten materials and further suppress the heterogeneous nucleation [8][40]. The problem at this stage was the high cost of Pd and Au, so the researchers started to look for the low-cost BMGs.

Since the 1990s, a lot of BMG compositions with general elements have been discovered by Inoue's group and Johnson's group. This has been a huge step for BMG development. Multiple component BMGs, such as the most famous Ti-Zr-Cu-Ni, Zr-Ti-Cu-Ni-Be and Zr-Al-Ni-Cu systems were fabricated [9], [41]–[43]. They have established a variety of methods and theories for BMG research. More and more alloy systems have been reported since the year 2000, such as Cu-, Ti-, Ni-, Co-, Mg- Fe-, La- and Ca-based BMGs [12], [14], [44], [45]. The Zr-TiCu-Ni-Be alloy system exhibits excellent GFA which can be fabricated into rods up to 14 mm diameter. These BMGs have excellent properties, such as

high yield strength, high hardness, high elastic limit, high fatigue resistance, very good corrosion resistance and magnetic properties. These properties make BMGs applicable in industrial applications and many of them are considered for the potential of structural applications. After decades' development, a lot of them have already been applied in commercial applications: the Fe-based BMGs have been used to fabricate 'current sensors', the Zr-Cu-based BMGs have been made for wear-resistant gear, Ni-based BMGs have been applied to make 'micro geared motors', and Mg- and Ca-based BMGs, which have very good biocompatibility, have the potential for medical applications [2].

2.2 Theories of Bulk Metallic Glass Formation

In order to have a deeper understanding of BMGs' formation mechanisms, scientists have done a lot research into thermodynamic, kinetic and structural aspects. These are the key factors to understand the formation of BMGs, especially for multi-component BMGs.

2.2.1 Structure of Bulk Metallic Glasses

The structure of BMGs has been investigated for decades due to their unique atomic arrangement. Many theories and models have been developed to investigate the structural nature of BMGs [46], [47]. Turnbull suggested that when designing MGs, the large size differences of the constituent elements contribute to enhance GFA [48]. Frank and Kasper studied the dense packing of the MGs and they found three different clusters of 12 atoms surrounding the 1 central atom [49], [50]. The three arrangements are shown in Figure 2. 1,

they represent the FCC (Face-Centred Cubic) structure, HCP (Hexagonal Close Packing) and an icosahedral packing respectively. Miracle *et al.* suggested the efficient packing is the fundamental principle of the MGs and BMGs [50]. They assumed that each solute atom is surrounded by a first coordination shell of solvent atoms.

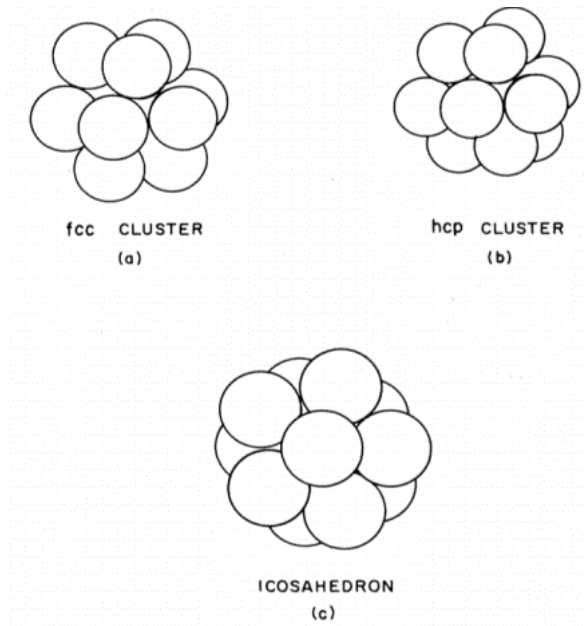


Figure 2.1: The three cluster models and corresponding arrangements [50].

Sun et al. [51] examined the nature of microstructure of the Zr-Cu-Ni-Al alloys. They used synchrotron radiation HE-X-Ray Diffraction (XRD) to investigate diffraction patterns. The icosahedral short-range order (ISRO) was considered to analyse the XRD curves. They found that the stable ISRO structure can hinder the diffusion of the atom to form crystalline nuclei. The atomic pair distribution function (PDF) was found by taking the Fourier transformation of the scattering function $S(Q)$. In order to get the results, they used several compositions of this alloy system. They also demonstrated that the radial distribution

function (RDF) $J(r)$ or pair distribution function (PDF) $g(r)$ can provide structural information for the amorphous materials. The PDF is shown in Equation 2.1

$$g(r) = \sum_{i,j} w_{i,j} g_{i,j}(r) \quad (2.1)$$

In this equation $g(r)$ indicates the total PDF and $g_{i,j}(r)$ shows the partial pair distribution function, which is between the range of the i th and j th atomic pairs. The alloy gets more stable with an increase in Cu atoms in this alloy system and the glass forming ability can be improved. The bond length of the Zr-Zr bond can also be significantly increased. They also noticed that efficient cluster packing (ECP) is another factor to influence the structure of amorphous materials. The FCC structure of the Zr-Cu-Ni-Al system is shown in Figure 2.

2. They treated this alloy system as a pseudo-ternary Ω - α - β alloy system. The solvent atom is Ω , the solute atoms are α and β . Comparing different compositions of this alloy system, the Cu atoms play a very important role. The stability of the ECP model can be enhanced when the small Cu atoms substitute the large Zr atoms in the alloy and the glass forming ability of this alloy system can be improved. That means that small changes in the atomic structure of the bulk metallic glass can lead to significant differences in glass forming ability. The mechanical properties can also be changed.

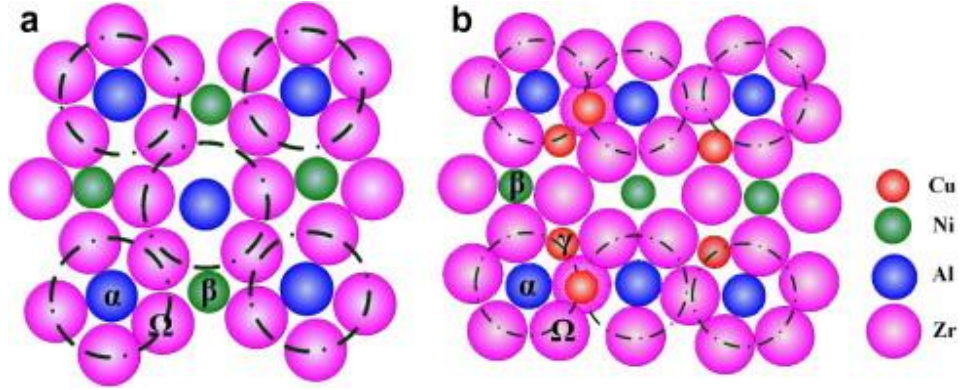


Figure 2.2

Figure 2.2: The ECP of the FCC structure for the Zr-Cu-Ni-Al bulk metallic glass. (a) and (b) show the {100} and {110} plane view respectively [51].

2.2.2 Thermodynamics of Metallic Glass Formation

For the thermodynamic aspects, the driving force for the nucleation of crystallisation is the Gibbs free energy difference (ΔG) between the supercooled liquid phase and nucleus. BMGs naturally exhibit small ΔG between the supercooled liquid phase and crystalline phase, which results in a low nucleation rate and contribute to high GFA [2]. Free energy can be expressed as:

$$\Delta G = \Delta H_f - T\Delta S_f \quad (2.2)$$

where H_f and S_f are the enthalpy of fusion and entropy of fusion respectively. When ΔG is negative, the whole system will become thermodynamically stable.

The crystallisation temperature of BMGs is strongly depending on the heating rate due to the nucleation process is a thermally activated process [52]. The BMGs are formed during

the rapid quenching due to the low driving force for the crystallisation in the supercooled liquid. The nucleation and growth rate are both low and lead to the suppression of the crystallisation. The driving force for crystallisation (ΔG) is obtained by the Gibbs free energy difference ΔG_{l-s} between the supercooled liquid and the crystals. Equation 2.3 indicates that the specific heat capacity $\Delta C_p(T)$ has a strong relationship with free energy.

$$\Delta G_{l-s}(T) = \Delta H_f - \Delta S_f T_0 - \int_T^{T_0} \Delta C_P^{l-s}(T) dT + \int_T^{T_0} \frac{\Delta C_P^{l-s}(T)}{T} dT \quad (2.3)$$

where ΔH_f and ΔS_f are the enthalpy and entropy of fusion respectively at temperature T_0 , where the crystal phase and the liquid are in equilibrium. Busch *et al* [53]–[55]. reported that the thermodynamic functions of different BMGs were determined by ΔS_f and $\Delta C_p(T)$ the relationship is shown in Figure 2. 3.

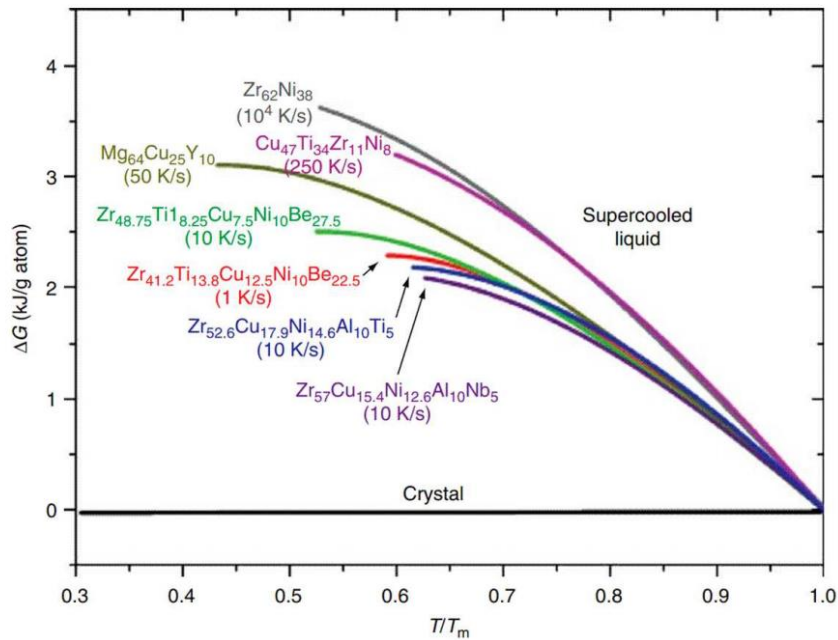


Figure 2.3: The Angell plot of Gibbs free energy variation between the liquid and crystalline state for different glass-forming materials [53].

There are some parameters derived from the thermodynamic aspects which are applied to evaluate the GFA of the BMGs. The supercooled liquid region ΔT_x is obtained by $T_x - T_g$, where T_x is the crystallisation temperature of the MGs during the heating process. In a general view, the higher the T_g , the lower T_i for most of the MGs. Another parameter $\gamma = T_x / (T_g + T_i)$ was suggested by Lu and Liu [56], [57] which is widely applied to assess the GFA of the MGs.

2.2.3 Kinetics of Metallic Glass Formation

For the kinetics aspects, understanding the viscosity or diffusion behaviour of the supercooled liquid is very important [52], [58]. A variety of methods were developed to evaluate the viscosity [59][60]. In general, the viscosity behaviour is characterised by the liquid fragility. The liquid fragility indicates the structural evolution during the rapid cooling process, hence the fragility has a strong relationship with the GFAs. Figure 2.4 illustrates the fragility plot produced by Angell [52]. The materials are classified as kinetically ‘strong’ and ‘fragile’ liquid. The viscosity of strong glass-forming liquids exhibits an Arrhenius relation with the temperature. The fragile liquids show a non-Arrhenius behaviour and are usually described by the modified Vogel-Fulcher-Tamman (VFT) relationship [61] as shown in Equation 2.4

$$\eta(T) = \eta_0 \exp\left(\frac{D^* T_0}{T - T_0}\right) \quad (2.4)$$

where D^* is the fragility parameter which identifies the thermal property of liquid, T_0 is the VFT temperature, at which the barriers with respect to flow would go to infinity, and η_0 is a constant inversely proportional to the molar volume of the liquid.

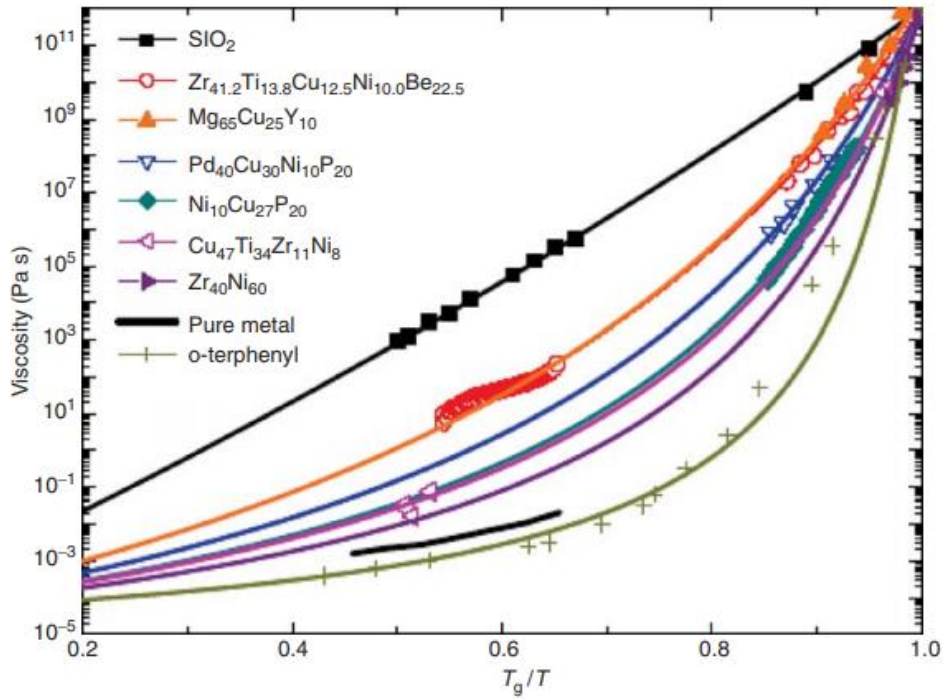


Figure 2.4: The Angell plot of different types of metallic-glass-forming liquids [53]. The materials are classified as kinetically ‘strong’ and ‘fragile’ liquid.

2.2.4 Alloying Element Effect to the Glass Forming Ability

The GFA of BMGs is complex and is strongly related to the joint effects of kinetics, thermodynamics and structures. Various researches have studied the influence factors of the GFAs and possible solutions to enhance the GFA. The alloying element of the BMGs is one of the important factors which strongly influence the GFA of the BMGs [62], [63]. ZrCu-

and Ti-based BMGs are among the most widely investigated BMGs. Several well studied alloy systems have been established such as Zr-Cu-Ni-Al, Zr-Cu-Al-Ag and Ti-Zr-Be-Al alloy systems. A variety of the research is based on these two alloy systems. The following discussion of the minor addition effect on the GFA of the alloy system will mainly focus on the ZrCu- and TiZr-based BMGs.

For the Zr-Cu-Ni-Al bulk metallic glass system, the composition of the $Zr_{55}Cu_{30}Al_{10}Ni_5$ has been widely investigated because it exhibits very high GFA. Inoue and Zhang reported in 1995 [64] that $Zr_{55}Cu_{30}Al_{10}Ni_5$ can be cast into the form of a cylindrical rod with diameter of 30 mm and length of 50 mm using the suction casting process and remain amorphous. The investigation of this composition became popular in recent times. The Zr element has a large atomic size compared to other elements, which will enhance the stability of the liquid phase. When the Zr content is higher than the eutectic composition, the mechanical properties will be enhanced for as-cast materials. This alloy system has extended eutectic and hypoeutectic compositions. Haruyama et al. [65] have investigated the free volume characterisation of the cold-rolled $Zr_{55}Cu_{30}Al_{10}Ni_5$ bulk metallic glass. They found volume dilatation of cold-rolled $Zr_{55}Cu_{30}Al_{10}Ni_5$ due to the free volume change during the cold-rolling process causing dilatation. The constituent elements Al and Ni have contributed to the enhanced GFA due to the atomic radius and heat of mixing differences.

The Zr-Cu-Al-Ag BMG system exhibited excellent GFA with suitable Ag elements. This alloy system shows a very wide supercooled liquid region, the range of ΔT_x varies between

70 to 110 K [66]. Jiang et al. reported that a series of alloy compositions of this alloy system can be cast with a diameter of at least 20 mm and the amorphous phase can be observed. Even for ingots of the alloy of 25 g the amorphous phase still occurs. Among these alloy compositions, $Zr_{46}(Cu_{4.5/5.5}-Ag_{1/5.5})_{46}Al_8$ should be highlighted [67]. From their investigations, the constituent elements Ag and Al were the elements that affect the GFA of the alloy. With increasing Al content, the decrement of the supercooled liquid region occurred. The effect of the Ag element was also investigated from kinetic and thermodynamic perspectives. They used the classical nucleation theory and calculated the steady-state crystal nucleation rate per unit volume I_{ss} . This parameter can produce the relationship between the kinetics and thermodynamics.

$$I_{ss} = \frac{A}{\eta(T)} \exp \frac{16\pi\sigma^3}{2k_B[\Delta G_{l-s}(T)]^2} \quad (2.5)$$

The viscosity is temperature-dependent and is expressed as $\eta(T)$, σ is the interfacial energy between the liquid and the crystal. From the equation it shows that in order to get good GFA, the driving force should be low and the viscosity should be high around melting temperature. According to the investigation, there exists the local atomic packing ratio and Gibbs free energy difference between the crystalline and amorphous phases. In order to get good GFA, the Gibbs free energy differences should be minimized and the local atomic packing ratio should be increased.

TiZr-based MG was first reported by Tanner et al. in 1977 [68]. Ti-Zr-Ni-Be system was reported by Johnson and Peker in 1994 [41]. From that time Ti-based BMGs developed

some systems with more complex and multi-component compositions. In the following years the development of the alloy systems tended to form Ti-Ni-Cu-Al [69] and Ti-Cu-Ni-Sn [70]. These alloys can be easily fabricated by copper die suction casting and injection casting. A recent investigation by Tang et al. found that the Ti-Zr-Ni-Be-Cu alloy system can be cast up to 50 mm in diameter, which indicated good GFA of the Ti-based BMGs [28]. During the development of Ti-based BMGs most of the alloy systems with very good GFA contain the element beryllium element. This element will significantly increase the glass forming ability of BMGs, enhance the plastic strain and make them easier to be fabricated in their supercooled liquid region. In recent years most of the alloy designs will start from the Ti-Zr-Be ternary alloy system combined with other elements with different requirements.

In 2012, Gong et al. developed a Ti-Zr-Be-Al system [71]. According to their investigation, the short-range order of the Al element will strongly increase the GFA of the alloy system. The Al element will suppress crystallisation formation. The liquid phase and atomic mobility are limited by this element. The formation of short-range order clusters during the melt will significantly enhance the GFA of the alloy system.

Guo et al. also reported ductile BMGs based on the Ti-Zr-Be system [72]. They added Cu and Ni into the system which resulted in very good GFA; the as-cast rod can be up to 14 mm in diameter. The yield strength is about 1680 MPa and the elastic strain limit is up to 5 %. They indicated that when designing good GFA alloy compositions, the following factors should be considered: they should form a wide supercooled liquid region, good

chemical interaction in the system, low liquidus temperature and the glass transition temperature should be reduced.

2.3 Introduction of Metallic Glass Composites

BMGs exhibit a lot of excellent properties such as high strength, high elastic limit, high hardness and good magnetic properties [6], [28], but along with the development of BMGs these materials exhibit some obvious drawbacks such as low fracture toughness, low ductility and failure under tensile loading. Due to the monolithic structure of BMGs, the unhindered shear bands after deformation will rapidly propagate. There are no other microstructure features to stop the propagation of single shear bands, which usually contributes to catastrophic failure. These drawbacks lead to many problems and limit the application of BMG materials. However, the main drawbacks for the BMGs are brittleness at room temperature and low fracture toughness. These problems limit further applications of BMGs. In order to overcome the BMGs' disadvantages, the concept of forming Bulk Metallic Glass Matrix Composites (BMGMCs) has been introduced and proven to be an effective way to improve the mechanical properties. BMGMCs are formed based on the glassy matrix and combine with the different reinforcement materials or second phase particles.

The combination of multiple particle phases, dendrites and glassy matrix contribute to the changes of the dislocation and microstructure features after deformation, which

significantly improves the mechanical properties of BMGMCs. In order to get the desired properties, the volume fraction of the second phases should be controlled. During the investigation of BMGMCs two directions of designing and making these alloys are developed in-situ and ex-situ methods. Eckert et al. have classified the general manufacture methods, which are shown in Figure 2. 5 [73].

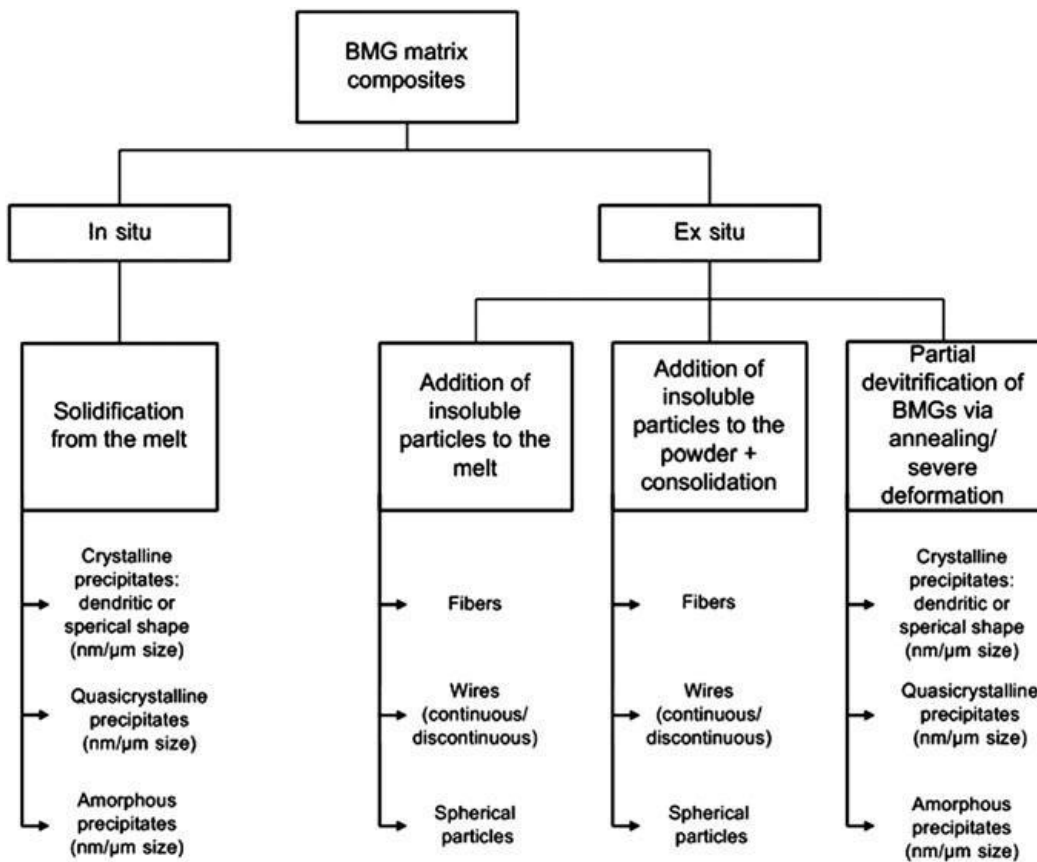


Figure 2.5: Classified BMGMCs manufacture processes [73].

The in-situ process is achieved by choosing the chemical compositions which will form the second phases in the glassy matrix during the solidification. The solidification will not produce the homogeneous phase, and the crystalline phases will be generated with the glassy matrix. The in-situ process is usually done by directly casting the materials into the mould

and the shape of the second phase is usually dendritic. If subsequent processing is applied to the as-cast alloys, the microstructure of the alloy can be controlled. The first toughened Zr-Ti-Nb-Cu-Ni-Be in situ BMGMCs were reported by Kim and Hays in 2000 [74]. The ductile dendritic phase was embedded into the BMG matrix, which strongly enhanced the plasticity under compression of the alloy. For ex-situ methods it can be separated to the following: (i) Combining the glassy phase and reinforcing the second phase particles in the general alloying process. (ii) Adding the reinforcements (crystalline second phase) directly into the glass forming process [73].

In 2007, the general developing strategy for designing BMGMCs was developed as follows: (i) The desired composite system should have a highly processable monolithic metallic glass matrix with sluggish crystallization. (ii) The composite system should have a stable crystal structure that cannot cause heterogeneous nucleation of the matrix so that the dendrites will form in the equilibrium systems. (iii) For the dendritic BMGMCs, the shear modulus of the dendrite needs to be lower than the glassy matrix, hence they would inhibit the propagation of shear bands and cracks in the glass matrix. (iv) The microstructure should have enough size and spacing for the glassy matrix and second phases [75].

The ductility is the main factor that influences the application of BMGs to structural applications. The BMGMCs are designed and developed to overcome this drawback. For the BMGMCs, the major factor that affects ductility is reinforcement material [76]. It is well known that the ductility of BMGMCs can be ascribed to the ductile dendritic crystalline

phase, which stabilises against the shear localisation and propagation of critical shear bands upon loading.

The reinforcement can be particles, fibres and dendrites. The microstructure will be changed when introducing the reinforcement into the BMGs and the mechanical properties should be enhanced. The strengthening effect is produced by the second phase particles in the BMGMCs. The yield strength of the composites can be obtained by using the rule of mixtures which is shown in Equation 2. 6

$$\sigma_c = V_r \times \sigma_r + (1 - V_r) \times \sigma_m \quad (2.6)$$

where σ_c is the yield strength of the composites and the volume fraction of the reinforcement is V_r , which can be particles, dendrites and fibres [77]. Yield strength of the reinforcement and matrix can be represented by σ_r and σ_m respectively. From the equation, the strength of the BMGMCs increases with the increasing volume fraction of the reinforcement. There are some factors of the reinforcement which will strongly affect the mechanical properties of the whole alloy system: The particle shape and size, volume fraction of the reinforcement and shear band initiation and propagation [78]–[80].

Most of ductile BMGMCs are formed based on the ZrCu- and Ti-based alloy systems. The Ti-based BMGMCs were first designed and reported by Hofmann et al. [81] which aimed to compare with the most famous Ti-6Al-4V commercial alloy. The alloy system Ti-Zr-V-Cu-Be was applied and the density for the alloy system is about 4.97 to 5.15 g/cm³.

They have introduced their design strategy for the Ti-based BMGMCs: (i) A suitable Ti-based BMG matrix alloy system should be decided first and should be highly-processable. (ii) The two-phase microstructure should be formed, which is usually bcc dendrites plus liquid. (iii) Dendritic phase with lower shear modulus is desirable. (iv) The deformation microstructure length scale in the glass phase should be homogenized and coarsened.

The very famous Ti-Zr-Be system was set for the matrix materials and both V and Cu were added into the system to form the dendritic phases. These types of BMGMCs have yield strength up to 1597 MPa. At the same time, they also developed the Ti-Zr-V-Cu-Al-Be alloy system [82]. The Al element will reduce the density and enhance the ductility of the alloy. They also exhibit very good mechanical properties and the comparison between these alloy systems and commercial Ti-6Al-4V is shown in Figure 2. 6. The Ti-Zr-V-Cu-Be system has very good properties by controlling the shear band movement which can be found from the stress-strain curve. The serrated feature on the curve proves the shear band movement was stable. Throughout their investigation of Ti-based BMGMCs, it is found that these alloys exhibit good tensile ductility and toughness. The mechanical properties are much better than the commercial Ti alloys.

The shape memory effect was also found in the Ti-based BMGMCs. Garagerella et al. reported the Ti-Cu-Ni shape memory BMGMCs [32]. The B2 and B19' Ti(Ni,Cu) ductile martensitic precipitates were found with the TiCu and Ti₂(Cu,Ni). The compressive strength and strain were significantly enhanced and it also showed good work-hardening behaviour

[32]. They also found multiple shear bands during the compression test, which was due to the stress concentrations around the precipitates, and the heterogeneous stress distribution was observed. The yield strength of the as-cast rod is up to 1172 MPa. This alloy system showed very good plasticity and contains no toxic elements. A large amount of alloy composition within this system can be cast over 10 mm diameter. The composition effect is the main factor affecting the properties of this alloy system. This is kind of the effect was also observed in the CuZr- based BMGMCs. A detailed study will be introduced in the following sections.

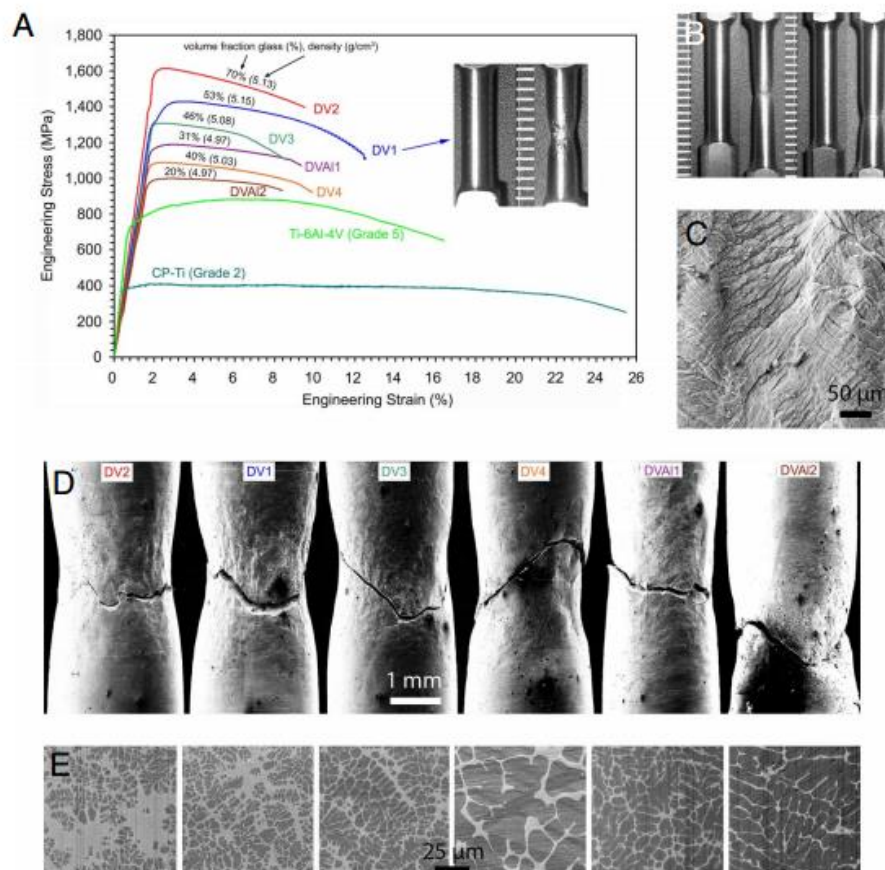


Figure 2.6: Tensile test of Ti-Zr-Be-V-Cu and Ti-Zr-Be-V-Cu-Be alloy system. (A) The room temperature tensile test strength-strain curve for 6 different compositions compared with commercially pure titanium and Ti-6Al-4V alloy. (B) The necking image of Ti-6Al-4V and commercially pure titanium. (C) Shear band morphology of one test sample. (D) Necking SEM images of test samples (E) The corresponding microstructure of necking images [82].

Another Ti-Zr-V-Cu-Be system has been reported by Qiao et al. [83]. The alloy was found with 43 % dendrites with 1–2 μm and the yield strength was about 1420 MPa. They found the shear band movement was hindered by the dendrites and dimples were found all over the fracture surface, which is the typical ductile fracture mechanism. The formation of BMGMCs has enhanced and improved the mechanical properties of BMGs.

The ZrCu-based BMGMCs were also fabricated via different fabrication process. Lu et al. [84] reported that the nanocrystalline structure was obtained by controlling the crystalline nucleation during the solidification process. In 1993, Johnson et al. [18] developed a quinary $\text{Zr}_{41.2}\text{Cu}_{12.5}\text{Ni}_{10}\text{Ti}_{13.8}\text{Be}_{22.5}$ metallic glass with a critical cooling rate of 1 K/s. This alloy became the first commercial BMG and is known as Vitreloy 1 (Vit 1). Johnson et al. then introduced Nb element to the Vit 1 alloy system and successfully obtained dendrite reinforced BMGMCs. The bcc $\beta\text{-Zr(Ti)}$ is observed from the SEM images.

2.4 Deformation Behaviour

The desire of making more real-life applications for BMGs materials has driven research towards the detailed study of the deformation of BMGs

The mechanical properties of the engineering materials are very important parameters for BMGs. BMGs only have amorphous microstructure, there are no grains or grain boundaries and mobile dislocation compares with the crystalline alloys. The mechanical properties of BMGs are enhanced by this microstructure. They exhibit high strength and high hardness, but there are also some drawbacks of BMGs, such as low plasticity and lack of work hardening behaviour. In order to improve these disadvantages, the deformation behaviour should be studied first.

2.4.1 Homogeneous and Inhomogeneous Deformation

There are two kinds of deformation mechanism for the BMGs: homogeneous and inhomogeneous plastic deformation. For the homogeneous deformation, the temperature and strain rate are high but for the inhomogeneous deformation the temperature is low and strain rate is high.

The term homogeneous deformation can be explained as, in the region of high temperature ($0.6T_g < T < T_g$) and high strain rate being applied to the BMGs, the plastic strain will distribute continuously in the viscous form BMGs and every element in the alloy system will contribute to the strain. For the inhomogeneous deformation, a low temperature

($T < 0.6T_g$), which is usually about half of the T_g , is applied on the BMGs. The shear bands will form the deformation and concentrate in these areas. Shear bands usually form on the planes which are close to 45° of the loading axis. These localised deformations are inhomogeneous deformations. Most investigations focus on the inhomogeneous deformation, especially the shear bands.

The inhomogeneous deformation will come along with the formation of shear bands and sudden fracture. Shear transformation zones (STZ) were reported by Argon et al. [38]. Along with an increase in stress, a localised distortion was created by the STZ and some thin and planar bands were formed. These bands are referred to as shear bands. Figure 2.7 shows the schematic of the STZ. When the deformation occurs, the small cluster of close-packed atoms will rearrange and accommodate a characteristic shear strain under the applied shear stress.

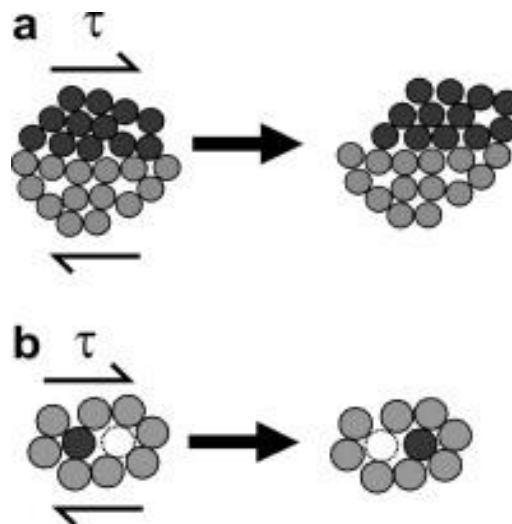


Figure 2.7: Schematic of the shear transformation zone [3].

The quantified process for the STZ was also reported and the activation free energy for the STZ is shown as Equation 2.7:

$$\Delta F_0 = \left[\frac{7-5\nu}{30(1-\nu)} + \frac{2(1+\nu)}{9(1-\nu)} \beta^2 + \frac{1}{2\gamma_0} \cdot \frac{\tau_0}{\mu(T)} \right] \cdot \mu(T) \cdot \gamma_0^2 \cdot \Omega_0 \quad (2.7)$$

where ν is Poisson's ratio, τ_0 is the thermal shear stress at which the STZ transforms, β is the ratio of the dilatation to the shear strain (of order ~ 1), γ_0 is the characteristic strain of an STZ. Ω_0 is generally believed to encompass between a few and perhaps ~ 100 atoms. The STZ is a very important element for the plastic deformation in metallic glasses. Two assumptions were made to explain the inhomogeneous deformation caused by the shear bands. One is the formation of the free volume, which will decrease the viscosity in the shear bands during the deformation. Another is that adiabatic heating will decrease the viscosity in the shear bands.

Homogeneous deformation in the metallic glass occurs with high temperature and high strain rate. STZ theories can be used to explain the deformation process. The homogeneous deformation can be defined by a large amount of atomic-scale independent events forming a statistical superposition. The size and energy scale will be unique. The deformation behaviour of $Zr_{55}Cu_{30}Al_{10}Ni_5$ bulk metallic glass was reported by Zhang et al. [85]. They applied the compression test to $Zr_{55}Cu_{30}Al_{10}Ni_5$ samples in the supercooled liquid region and found that the deformation behaviour in the supercooled liquid region was strongly influenced by the temperature and strain rate. The viscosity of the materials will change from the Newtonian flow regime to the non-Newtonian flow regime when the strain rate

increases. They established the metallic glass strain rate, viscosity and temperature relationship. They found that the viscosity and temperature relationship around the glass transition temperature can be expressed by the Arrhenius function:

$$\eta N = B \exp\left(\frac{H}{RT}\right) \quad (2.8)$$

where η is the viscosity H is the activation energy in the viscosity region and B is the structural parameter. They also applied the stretched exponential function to demonstrate that the bulk metallic glass deformation behaviour and function can be expressed by Equation 2.9:

$$\frac{\eta}{\eta N} = 1 - \exp\left[-\frac{D}{(\eta N \dot{\epsilon})^\beta}\right]. \quad (2.9)$$

The free volume theory is one of the most famous. The traditional free-volume theory states that the viscosity of the liquid is strongly related to its own volume. Turnbull and Cohen established a widely applicable theory based on the traditional free-volume theory [27]. They suggested that the liquid atoms are in a condensed state and some atoms' movements are trapped by the neighbouring atoms. There is little space for the atoms to move: the atom can only move when there is a large space formed next to it, allowing it to move further.

2.4.2 Shear Band Nucleation and Propagation

Shear bands are major research topics for the deformation mechanism of BMGs. The STZ must be examined precisely when investigating the mechanical properties of the bulk

metallic glass. When plastic flow occurs, stress is applied to the STZ and the shear band are formed on the localised area during the process.

Qu et al. reported the composition $Zr_{53}Cu_{18.7}Al_{16.3}Ni_{12}$ bulk metallic glass with very high plasticity. They found that when the applied load is in the longitudinal direction, atomic strain saturation occurs, and the structure moves to the closest packing when the yield of the atoms is in the transverse plane. The connection between the atomic flow movement and shear was investigated. When the atomic flow reaches a homogeneous level and coexists with the large scale shear band, this will enhance the formation of the shear transformation zone and promote the multiplication of shear bands. Shear band formation and propagation will strongly influence the mechanical and deformation behaviours. Good mechanical properties can be found for this alloy system. $Zr_{55}Cu_{30}Al_{10}Ni_5$ reported as the bulk metallic glass with very good GFA and $Zr_{60}Cu_{20}Al_{10}Ni_{10}$ has high resistance to embrittlement. Figure 2. 8 shows that mechanical properties are strongly influenced by the composition of the materials. Greer et al. summarised the shear bands mechanism in the BMGs and BMGMCs. The shear band nucleation and propagation will control the yielding and plasticity of most BMGs and BMGMCs [86], [87].

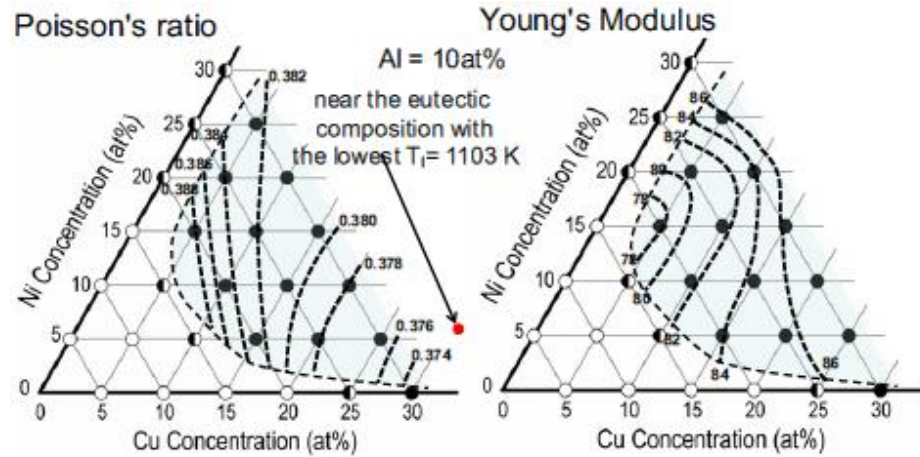


Figure 2.8: Effect of the composition of the Zr-Cu-Ni-Al system to Poisson's ratio and Young's modulus [85].

Greer et al. [4] figured out the major features of shear bands: they usually form along the maximum shear stress planes; they exhibit low flow stress when the cohesion is maintained and cracks may develop; they will contribute to local distortion of the materials; when the flow stress decreases this will lead to local heating; and they are very thin, about 20 nm. Three scenarios were established for the formation of shear bands. For the first one, the amount of homogeneous and active STZs exceed the percolation limit. The percolation limit is the point where STZs interact with each other and align in a two-dimensional plane. The percolated STZs will mainly form on the plane with the maximum shear stress. The deformation band will then form and lead to shear strain formation and the shear bands will subsequently develop. This theory demonstrates that the shear band is the inherent structural change within the amorphous microstructure. The second scenario indicates that the shear bands will form when the local stress is much bigger than the global average value. The

shear bands are very easy to form even in small sizes. The third scenario describes that the shear band nucleation consists of two continuous stages: the structural rejuvenation which will create a viable band for the shearing—this stage can be finished in microseconds and the shear-off and sliding of the original rejuvenation planes. Large plastic strain will be applied and local heating will form and lead to the formation of shear bands. The shear band nucleation will initiate from the large stress concentration in the glassy matrix.

Wang et al. [88] reported that the alloy composition $Zr_{46}Cu_{31.6}Ag_{8.4}Al_8$ exhibited good plastic behaviour such as compressive plastic strains. A slight change in the composition of the alloy will cause a huge difference in plasticity. They also found that during compression tests, the likelihood of formation of shear bands increased with increasing number of atoms which take part in the yielding. This is because increasing the Zr content of the alloy will affect the plasticity of the materials. When the content of Zr increases, both the formation of the Zr-Zr bond volume and the bond length will increase, and more shear bands can be formed during the movement of the atoms. The composition change will strongly influence the final structure of the materials. This gives very similar results compared with the Zr-Cu-Ni-Al bulk metallic glass system.

Due to the unique structure of BMGs and BMGMCs, the yield stresses are different in tension and compression. A suitable yield criterion should be developed to investigate the yield behaviour of these alloy systems. Donovan et al. [89] reported that the yielding process will follow the Mohr-Coulomb criterion. According to this theory, yielding behaviour

depends on the applied shear stress and the stress normal to the shear displacement. Due to the unique structure of BMGs and BMGMCs the flow strength-to-modulus ratio is not negligible. The Mohr-Coulomb criterion can be expressed as:

$$\tau_y = \tau_0 + \alpha\sigma_n \quad (2.10)$$

where τ_y is the effective shear yield stress, τ_0 is a constant, α represents the system specific coefficient, which controls the strength of the normal stress effect, and σ_n is the shear displacement. Atomic level analysis for the pressure-dependent yielding was investigated by Schuh and Lund [40]. This theory is based on the STZs concept and proved that the Mohr-Coulomb criterion is suitable for the BMGs.

2.5 Methods for Plasticity and Work Hardening Improvement

During the development of BMGs, various concepts have been introduced to improve their mechanical properties. The main problems for BMGs are a lack of plasticity and no work-hardening behaviour. The following sections will demonstrate the methods which will provide the solutions to overcome these drawbacks.

2.5.1 Phase separation

The phase separation process of BMGs can be explained by a homogeneous glassy phase with a specific composition separating into two glassy phases with different compositions [90]. The phase separation is mainly caused by the spinodal decomposition or nucleation and growth. Phase separation is more likely to happen in the BMGs alloy systems that

contain at least one atom pair with large positive enthalpy. The first phase separation phenomenon in La-Zr-Al-Cu-Ni alloy system was reported by Turnbull [91]. This was the first reported phase-separated BMG with no nanocrystalline structures. In order to obtain a two-phase BMG, two alloy systems with good GFA were selected (La-Al-Cu-Ni and Zr-Al-Cu-Ni). Both Zr and La have negative heats of mixing with the other three elements, but Zr and La have a positive heat of mixing. Two amorphous phases with different compositions were observed from the La-Zr-Al-Cu-Ni alloy system. Inoue indicated that there are two different kinds of phase separation situations [92]. One is nano-scaled fine crystalline structure dispersed into the glassy matrix of the as-solidified samples, which is usually due to the low GFA of the BMG systems. Another is when two completely amorphous phases form during the solidification process or reheating of the original homogeneous amorphous alloy. Phase separation will occur between two phases which have a thermodynamically stable miscibility gap. The binary alloy systems with zero or positive heat of mixing have more chance to form the phase separation alloys. However, compared with the traditional theory of the formation of BMGs, the phase separation behaviour formation is a contradictory process. Negative heats of mixing of the alloy systems are more desirable for BMGs, but a positive heat of mixing is an important factor for the phase separation process. The interesting fact is that along with the development of BMGs, a variety of phase separated BMGs have been discovered such as Pd-Ni-P [93], Al-Ni-Y-Co-Pb [94], Cu-Zr-Ti [95], Cu-Zr-Al [96] and Zr-Cu-Ni-Al [97]. Most of the phase separation evidence was obtained by

small-angle x-ray diffraction (SAXS), TEM and DSC. At least two elements with positive heat of mixing will form phase-separated BMGc.

The studies of BMG phase separation have introduced another way to form 'composite like' BMGs which exhibit a unique microstructure and lead to the enhanced mechanical properties. The wide supercooled liquid range will enable the study of the decomposition behaviour of BMGs. There are two common types of microstructures for the amorphous phase separation: the droplet-type structure by the nucleation and growth mechanism; and the interconnected-type structure by spinodal decomposition. The free energy will increase in the metastable region due to the infinitesimal composition fluctuation. The nucleation of the new phase must lower its free energy to enable the following process. Figure 2. 9 indicates that the $Y_{28}Ti_{28}Al_{24}Co_{20}$ exhibits a spinodal decomposed interconnected-type microstructures with dark and bright contrasts. The Ti-riched and Y-riched phase are observed.

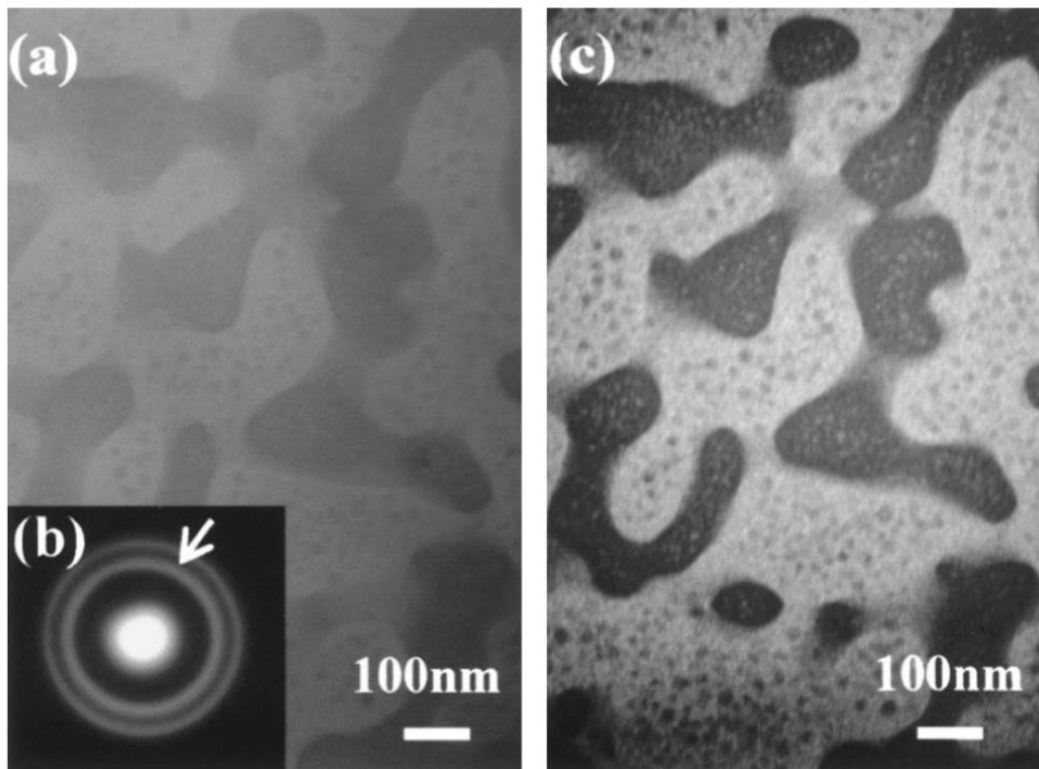


Figure 2.9: (a) BF- TEM micrograph showing a typical microstructure formed by phase separation in as-melt spun alloy, (b) Corresponding SAED pattern showing double halo rings, and (c) DF- TEM micrograph obtained using inner diffuse halo ring marked in (b).

Chen et al. recently reported a $\text{Cu}_{47.2}\text{Zr}_{46.5}\text{Al}_{5.5}\text{Nb}_{0.8}$ BMG which shows phase-separation structure. The phase separation structure leads to the large room temperature plasticity of 16%. The phase separation was examined by the EDS and EELs which are proved to be an effective method to check the phase separation structure [98].

2.5.2 Increase in Poisson's ratio

Poisson's ratio or shear modulus to bulk modulus ratio reflects the complexity level between the shear band nucleation of and volume fraction. They have strong relationship

between the chemical bond and structure [99]. Lewandowski et al. [100] indicated that BMGs shows enhanced ductility and plasticity when the Poisson's ratio is larger than 0.31–0.32. In year 2011, Demetriou et al. designed a $\text{Pd}_{79}\text{Ag}_{3.5}\text{P}_6\text{Si}_{9.5}\text{Ge}_2$ BMG which exhibits excellent ductility and fracture toughness which is very similar to the low carbon steel [101]. Na et al. investigated the relationship among the Poisson's ratio, fragility index and plasticity of the BMGs. They found that the fragility value can be expressed with Poisson's ratio. A larger Poisson's ratio will contribute to the high fragility value. For the BMGs with high m values, the liquid phase viscosity is reduced and further reduce the propagation of the shear bands, finally lead to the ductile deformation behaviour. The Zr-TM-Al (TM=CO, Ni, Cu) alloys have been studied by Xu and Ma. The $\text{Zr}_{61}\text{Ti}_2\text{Cu}_{25}\text{Al}_{12}$ alloy has a Poisson's ratio = 0.367, and it showed a very high fracture toughness. Their researches have indicated that high ductility BMGs are usually obtained from the rich main element alloy composition system, such as high Zr alloy system [102], [103].

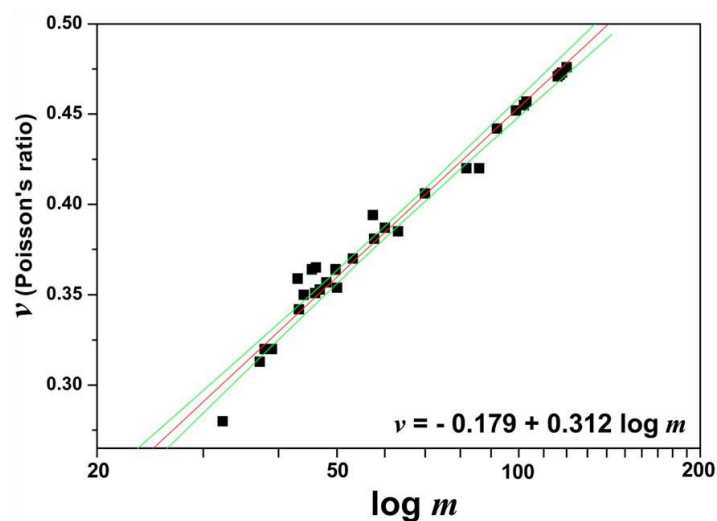


Figure 2.10: The Correlation between the Poisson's ratio and the fragility index for Cu-based BMGs [104].

2.5.3 Phase Transformation Induced Plasticity

The concept of transformation-induced plasticity (TRIP) has been widely investigated and applied to steels and ceramics for many years. This technique has significantly increased materials' plasticity and work hardening ability at high strength [105]. In order to get good work hardening, plasticity and uniform ductility, this effect has been introduced to make BMGMCs. The formation of this effect involves very complex thermodynamic and kinetic processes. The ideal process is to form a metastable austenite phase into the amorphous matrix. When the back-stress effect is applied to the alloy, the transformation phase combined with the amorphous matrix will produce a highly improved plasticity and strength [106]. However, the requirements for successful achievement of this effect are very high: the BMG matrix should have a good GFAs; the metastable phase must be formed and must not decompose to the other brittle phases during the cooling; the fabrication process and alloy compositions must not influence the martensitic transformation of this austenite phase during the deformation. The studies of TRIP effect in BMGMCs have mainly focussed on the CuZr-based BMGs. CuZr BMGs have very good GFAs and will form a cubic B2-CuZr phase with specific composition ranges. Moreover, the B2-CuZr phase undergoes a stress-induced martensitic transformation to B19'-CuZr phase. The B2-CuZr phase has the

potential to be the metastable phase of the TRIP process. The crystal structure transformation process is shown in Fig 2. 11 (a) and (b).

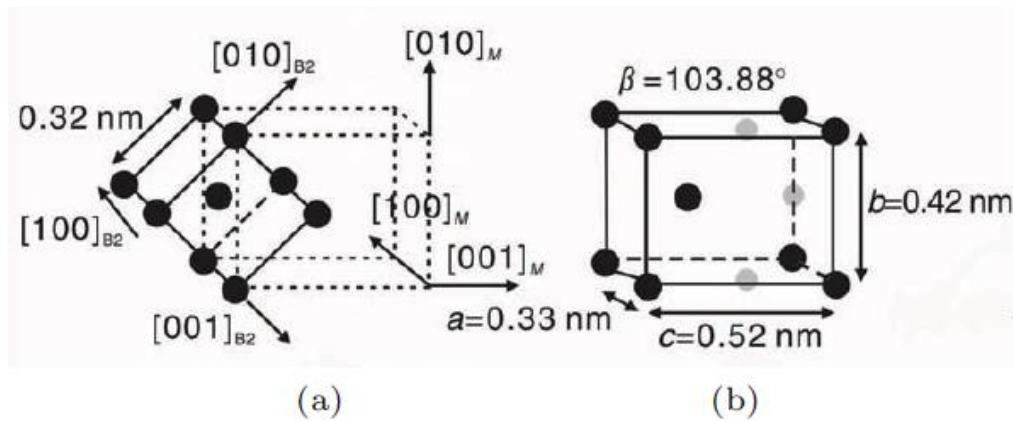


Figure 2.11: The transformation process of (a) The Crystal structure of B2-CuZr to (b) B19'-CuZr martensitic structure [107].

Pauly et al. [107] reported the martensitic transformation (B2 to B19') in the Cu-Zr-Ti and Cu-Zr-Al systems. The yield strength of the alloy can be up to 1246 MPa and the fracture strain is 14.9 %. The Cu-Zr-Ti system also shows good work hardening ability. In their study they have indicated that the Ti element will destabilise the B2 CuZr phase at a relatively low temperature and will lead to the formation of Zr_2Cu and Zr_7Cu_{10} phases. However, the Al element has no significant influence on the B2 phase formation [107]. This group has done further investigation for the microstructure nature of Cu-Zr-Al BMGMCs as shown in Figure 2.12. They indicated that different melting conditions will strongly affect the volume fraction of the B2 phase and the content of the B2 phase is the key factor in changing the mechanical properties. The plasticity is much better for samples with a volume fraction of the crystalline phase between 5–30 vol. %, compared with samples with a volume fraction

over 50 vol. %. They have tested the mechanical properties of the B2 CuZr phase in $\text{Cu}_{47.5}\text{Zr}_{47.5}\text{Al}_5$ for the first time. They also found that the glass solidification and crystalline phase growth processes will occur at the same time. They have figured out a way to improve the ductility of the BMGMCs without sacrificing strength [108], [109]. In 2010, Pauly et al. applied a tensile test to the CuZr-based BMGs and found nano-sized precipitate and clear twinning in the microstructure. They suggested that the temperature rise could cause nanocrystallisation in shear bands of deformed samples. They have clearly demonstrated the CuZr-based BMGs' deformation process as shown in Figure 2.13. When loading is applied to the alloy, local stress concentration will occur. The B2 phase will precipitate after a period and reduce the stress concentrations. The STZs will also form and develop, but the propagation of the shear bands can be hindered by the B2 nanocrystals. The twinning of B2 crystals forms and further absorbs the stresses from the matrix. The whole process significantly delays the fracture of the alloy and increases the ductility [31].

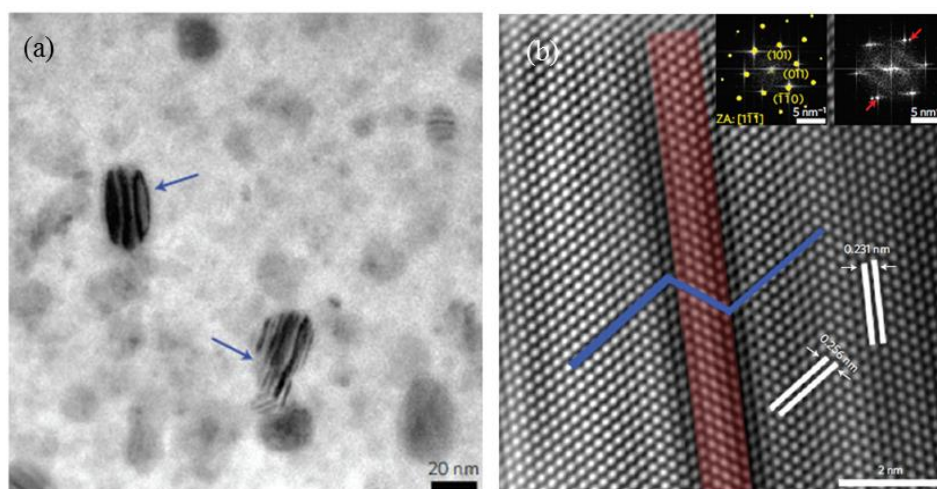


Figure 2.12: (a) The TEM images of deformed $\text{Cu}_{47.5}\text{Zr}_{47.5}\text{Al}_5$ alloy with typical twins contrast. (b) HRTEM images of the lattice planes, the twins and B2 CuZr phase were examined. The inset shows the FFT of the twins and B2 phase.

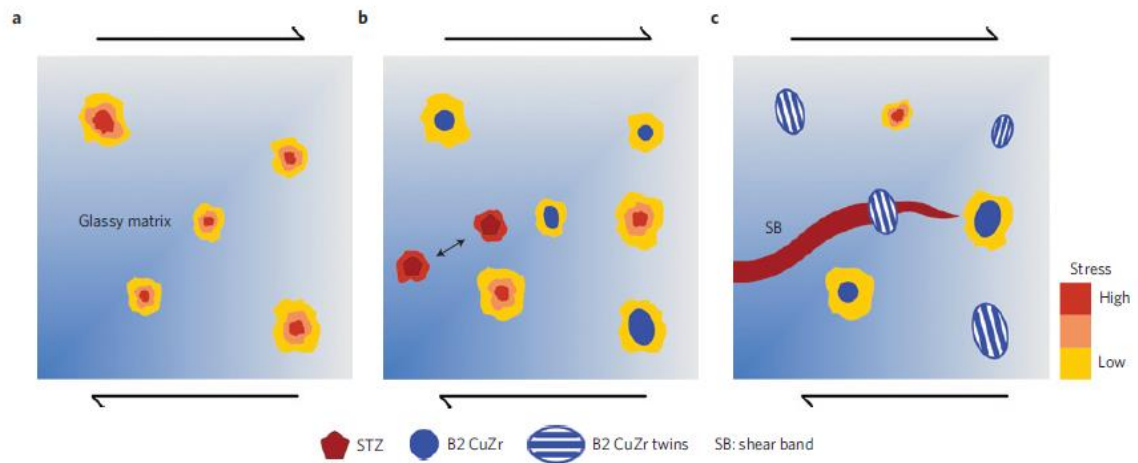


Figure 2.13: The deformation process in the CuZr based alloy systems. (a) The glassy matrix is shown in blue and the local stress concentrations shown in red to yellow will generate at the beginning of loading. (b) A variety of nanocrystal morphologies are formed due to stress. The STZs start to develop in this region at the same time and are blocked by the nanocrystals. (C) The STZs will band together to form a nascent shear band which will absorb the stress and hinder the fracture propagation.

In 2010, Wu et al. [84] performed tensile tests to the $\text{Zr}_{48}\text{Cu}_{47.5}\text{Al}_4\text{Co}_{0.5}$ alloy system and an obvious work-hardening process has been observed. They have investigated the B2 CuZr phase morphology change during different strain conditions. At the beginning of the plastic deformation process, the B2 phases are round and stress concentrations are formed around these phases. The phases will then extend along the loading direction during the work-

hardening stage, followed by the formation of small shear bands. For the near fracture stage, the cracks will approach these phases and result in a stress decrease. They suggested that most of the fracture caused by cracks were due to the crystalline phase and glass matrix interface separation. The microstructures and tensile test processes are shown in Figure 2.14

(a)–(c).

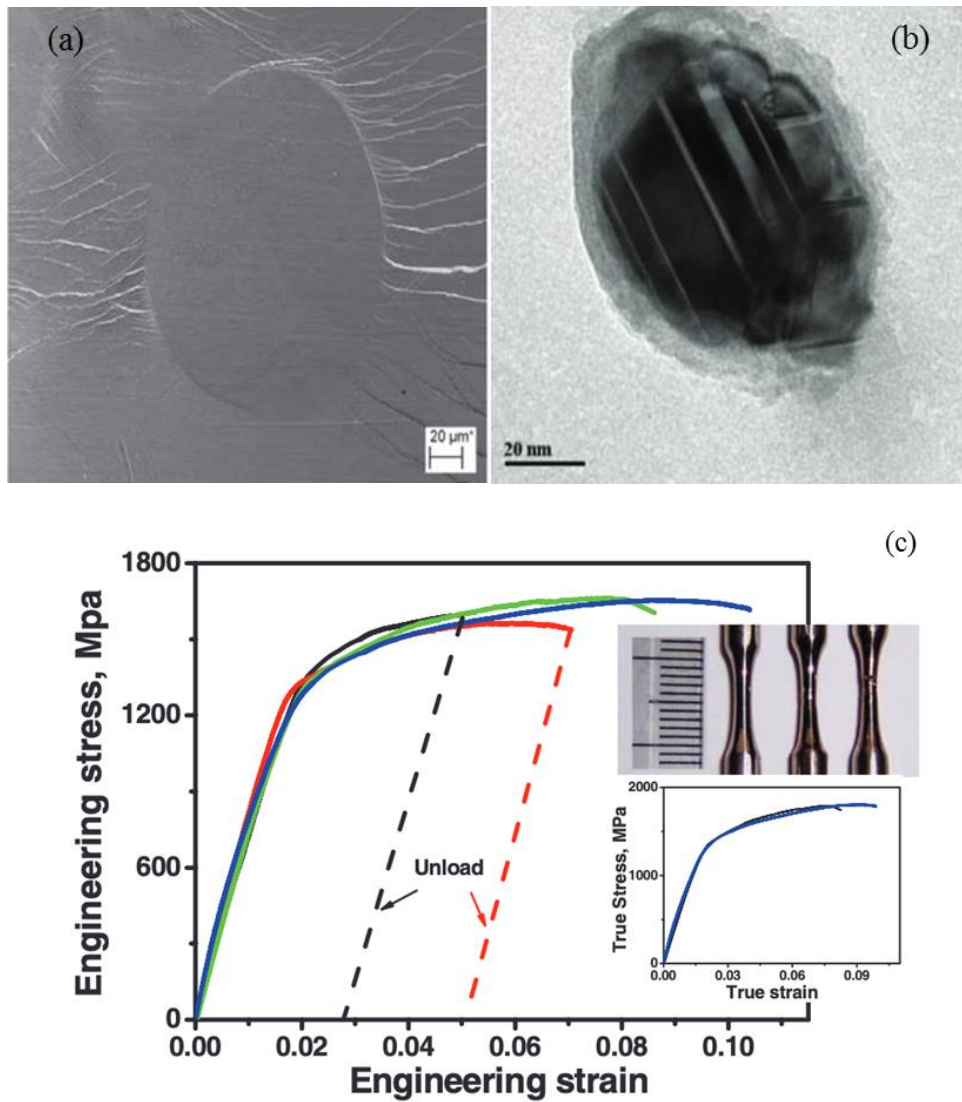


Figure 2.14: (a) The SEM image of tensile test sample, (b) Martensite phase after the TRIP process, (c) Tensile engineering stress-strain curve for different stress conditions, inset shows the true stress-strain curve [106].

Hofmann compared tensile properties of TRIP reinforced BMGMC $Zr_{48}Cu_{47.5}Al_4Co_{0.5}$ with body centre cubic (bcc) dendrite reinforced $Zr_{39.6}Ti_{33.9}Nb_{7.6}Cu_{0.5}Be_{12.5}$. The results and microstructure are shown in Fig 2. 15. The TRIP reinforced material exhibited very good tensile plasticity and work-hardening behaviour, even when the crystalline volume fraction was smaller than the bcc reinforced BMGMC [22].

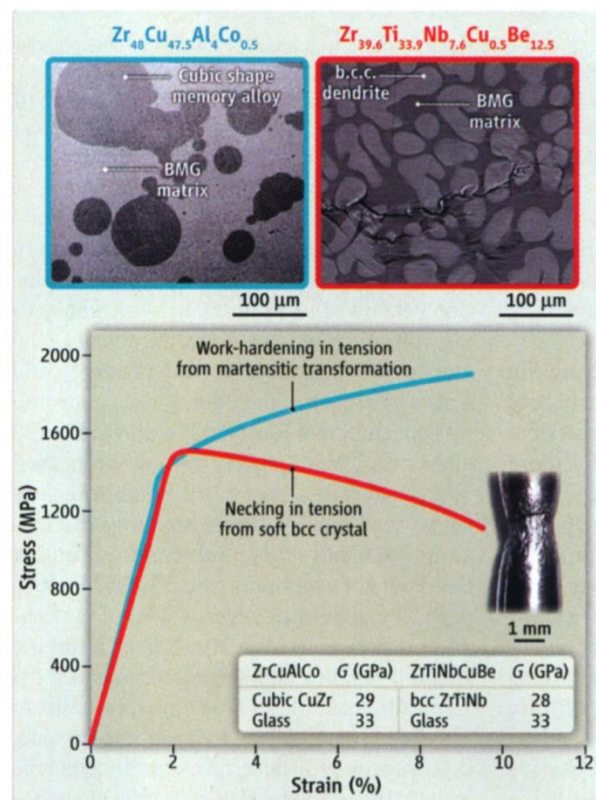


Figure 2.15: The tensile test curves and SEM images of TRIP reinforced BMGMCs and bcc dendrite reinforced BMGMCs [22].

Detailed studies of alloy composition and cooling rate effects on the microstructures of CuZr- based TRIP alloys have also been performed by Wu et al. [33] in 2011. Alloy compositions of $(\text{Zr}_{0.5}\text{Cu}_{0.5})\text{Al}_x$ ($x = 1, 2, \dots, 10$ at. %) with as-cast diameters up to 10 mm have been investigated. They found that with different cooling rates (casting sizes) of the samples, the phase formation process can be very different. They summarised the as-cast sample microstructure changing process for this alloy system: the fully amorphous phase forms first when the casting diameter is low and the B2 phase combined with the amorphous phase structure will form when the casting diameter is increased. The Al_2Zr , B2 and amorphous phases will form together with large casting diameters. They indicated that the casting size is a key factor affecting the microstructure. The B2 phase could be homogeneously distributed in the glassy matrix, with a spherical shape, when the diameter was 3 mm. However, the shape of the B2 phase became patch-like and randomly distributed in the glassy matrix when the diameter was 4 mm. They also demonstrated that the composition inhomogeneity is caused by the temperature gradient during the rapid cooling process. Larger casting sizes provided more thermal diffusion space and the composition inhomogeneity became large. The microstructure features with different Al content and cooling rates were also plotted by the group as shown in Figure 2. 16.

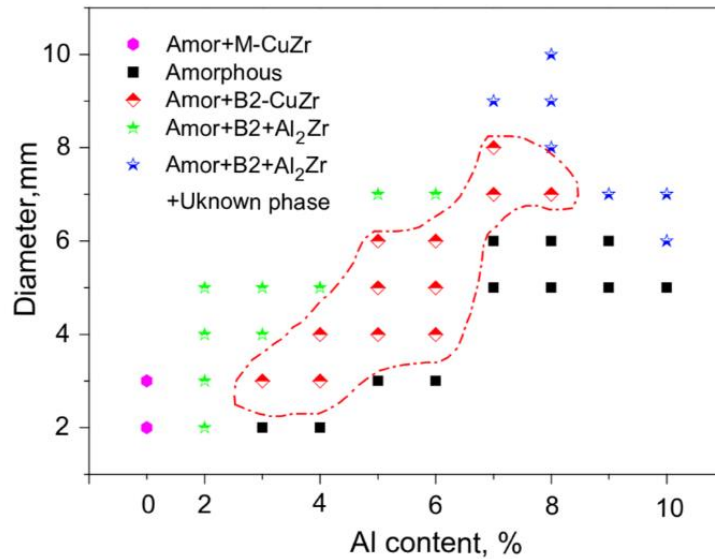


Figure 2.16: The microstructure changes with different Al content and diameters of $(Zr_{0.5}Cu_{0.5})Al_x$ ($x = 1, 2, \dots, 10$ at. %) [110].

They have indicated that tensile ductility was found for the single B2-CuZr phase type samples, and samples with intermetallic Al_2Zr phases exhibited brittle properties. The blocking effect was observed for the tensile samples: the shear band propagation was obstructed by the crystalline B2-CuZr phase, and secondary shear bands were generated around the B2-CuZr phase. The rapid crack process was significantly delayed by this effect. Further investigation by the same group has indicated that the volume fraction, size and distribution of the metastable B2-CuZr phase have strong relationships with the mechanical properties. They reported that the BMGMCs exhibit the best mechanical properties when the sample contains the B2-CuZr phase and amorphous matrix structure only. The yield stress decreases with an increase in B2-CuZr phase volume fraction, which generally obeys the rule of mixtures (ROM). In contrast, the fracture strength shows a near-constant value.

This will not change with the volume fraction of the B2-CuZr phase. The B2-CuZr phase has relatively low yield stress but the glassy matrix has very high yield stress, and according to the ROM, the yield stress will vary with the volume fraction of B2-CuZr. The deformation-induced martensite phase has a similar fracture strength to the glassy matrix, so the fracture strength has no big differences between samples. Despite the cooling rate effect for the TRIP BMGMCs, researchers found that there are still some other factors to influence the phase structure and morphology of the samples. Kou et al. [111] have suggested that the casting mould shape can change the morphology and plasticity of the TRIP reinforced BMGMCs. Pauly et al. found that by applying different melting currents before the casting process, the volume fraction and distribution of the B2-CuZr phase exhibited very obvious differences which lead to the mechanical properties variations. Okulov et al. [112] have applied the Joule Heat-treatment process to $\text{Cu}_{47.5}\text{Zr}_{47.5}\text{Al}_5$ BMGMCs ribbons. The microstructure can be controlled through this rapid heating method and this was the first time the single B2-CuZr phase combined with glassy matrix could be fabricated other than using the casting process.

The mechanical properties of the TRIP reinforced BMGMCs is strongly dependent on the martensitic transformation. The martensitic transformation ability of the metastable phase plays a key role in the plasticity and work-hardening ability. Wu et al. have systematically investigated the effect of alloying elements on the stacking fault energy of the B2-CuZr phase. The Cu element was substituted by minor addition of alloying elements

and they found that the $\{011\} \langle 100 \rangle$ slip system has the lowest stacking fault energy, so the phase transformation is more likely to happen in this system. The alloying elements can significantly change the electronic density of B2-CuZr during the phase transformation. The alloying elements which reduced the electronic density charge redistribution can further reduce the stacking fault energy of the CuZr phases, and vice versa. They have indicated that with the same volume fraction of the B2-CuZr phase, but different stacking fault energy, BMGMCs can exhibit different mechanical properties. The BMGMCs with lower stacking fault energy has lower yield strength but better plasticity. The BMGMCs with higher stacking fault energy exhibit in a contrary way. The reduction in stacking fault energy of the metastable phase will contribute to the formation of twin nuclei and further development of the twin structure. The TRIP effect formation should become easier under this situation and further reduce the stress concentration in the amorphous matrix.

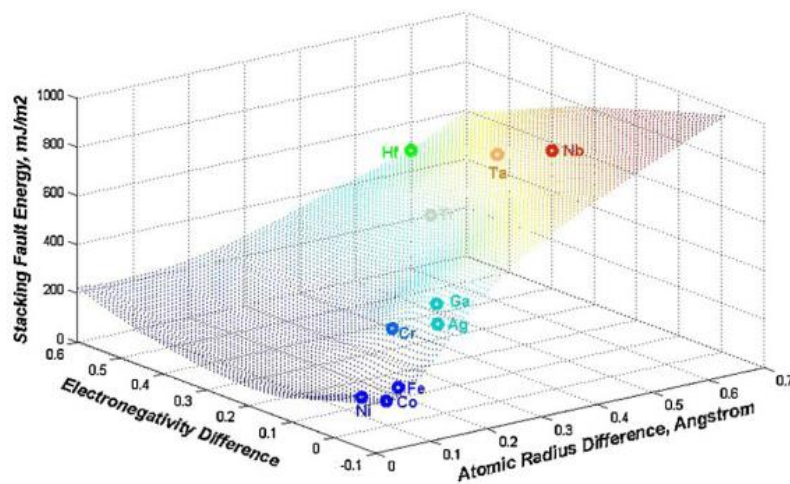


Figure 2.17: The B2-CuZr phase stacking fault energy dependence of the electronegativity and atomic radius difference with different alloying elements [84].

Along with the development of TRIP reinforced BMGMCs, the desire to make relatively large samples with good plasticity and work-hardening ability became very strong. Making large size TRIP reinforced BMGMCs poses some challenges: the GFA of the amorphous phase should be high; the cooling rate will rapidly decrease when the sample size becomes large. The low cooling rate will contribute to the formation of the brittle phase, lower the volume fraction of the amorphous matrix, enlarge the metastable phases and cause random distribution of metastable phases. An effective way to manipulate the nucleation and crystal growth is desired. Song et al. recently announced an attempt to solve these problems. They introduced the idea of heterogeneous nucleation to control the microstructures of the BMGMCs. Figure 2. 18 shows the heterogeneous nucleation process for the TRIP reinforced BMGMCs.

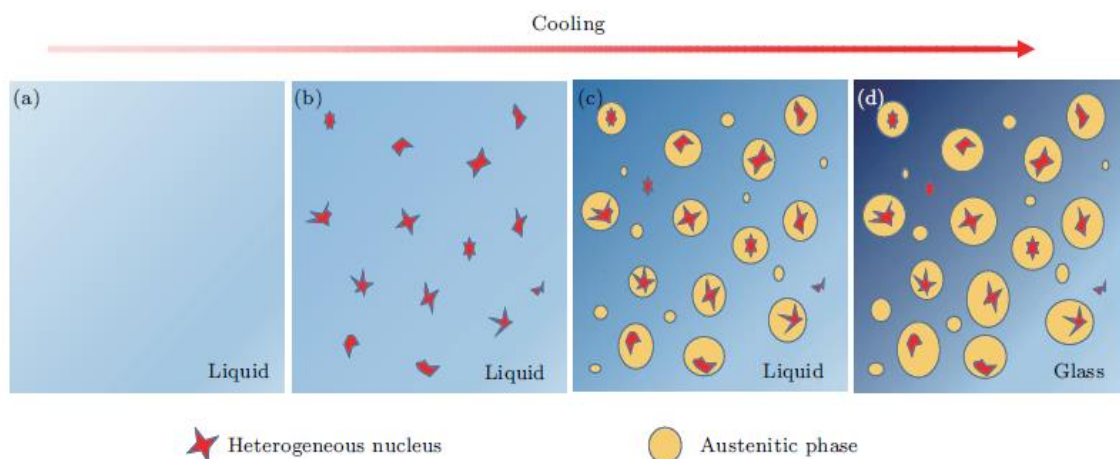


Figure 2.18: The schematic of the heterogeneous nucleation process for developing large-sized BMGMCs. (a) The suitable alloying elements have increased the GFA of the matrix. (b) The alloying elements will form intermetallic with the main elements due to the decrease in

temperature. (c) The high melting point intermetallic will contribute to the formation of the homogeneous distributed metastable phase. (d) The remaining molten materials will form the amorphous matrix [113].

The $\text{Cu}_{47}\text{Zr}_{48}\text{Al}_4\text{Ag}_1$ alloy was selected as base alloy, and minor addition of Sn was added into the glassy matrix. Sn will form Zr_5Sn_3 with Zr due to the negative heat of mixing. The high melting point of about 1988 °C will make this intermetallic structure retain in the microstructure and become the heterogeneous nucleation nucleus. The B2-CuZr phase will precipitate homogeneously as a consequence. The crystalline nucleation and growth is a competitive process during the solidification: more heterogeneous nucleation means the grain growth driving force will become smaller, which will suppress the rapid growth of the B2-CuZr phase and form a homogeneous distributed fine structure. The Zr-Cu-Al-Nb alloy system was reported by Wu et al. which exhibited large tensile plastic deformation after the tensile test, and they indicated that the B2 phase can effectively improve the local stress concentration. The B2 phase can stabilise the tensile plastic deformation by boosting the interaction of shear bands

The detailed studies of the deformation mechanism of TRIP reinforced BMGMCs were conducted by the neutron diffraction technique. Wu et al. have reported that the crystalline structures with different orientations showed significant anisotropic properties. Most of martensitic transformation occurred on the (110) plane. They found that the atoms of the martensite phase were all located on the interface between the amorphous matrix and the

crystalline phase. To summarise, the TRIP effect can significantly improve the mechanical properties of BMGMCs. This kind of BMGMC has strong potential to be developed and investigated.

2.6 Summary of literature review

In this chapter, a brief history and the development of BMGs and BMGMCs have been introduced. The nature of BMG formation has been investigated through kinetic, thermodynamic and structural aspects. BMGMCs were then introduced and deformation behaviours and mechanisms were investigated. The last section introduced several methods to improve the plasticity and work-hardening behaviour of BMGs.

Chapter 3

Experimental Methods

3.1 Materials Preparation

3.1.1 Alloy Preparation

The constituent elements of different alloy systems were made in batches of 2–5 g. All the constituent elements were in sheet format with purities $\geq 99.99\%$. All the elements were carefully ground using abrasive paper to remove oxides or dirt from the surfaces. The elements were then cleaned using isopropanol and cut into small pieces. The elements were weighed on a Precisa XB 120A electronic mass balance device with an accuracy of 0.1 mg. Elements were finally cleaned in isopropanol for 5 minutes using an ultrasonic cleaning machine before the arc melting process.

3.1.2 Arc Melting

Arc melting process was performed using the MAM1 Edmund Buhler arc melter. The arc melter consists of three parts: a vacuum chamber with copper hearth, a water-cooling system and a power supply. The melting chamber setup is shown in Figure 3. 1 (a) and (b). Due to the high-level melting requirements of BMGs and BMGMCs, the chamber was cleaned using isopropanol, and the copper hearth was cleaned using 4000 grit grinding paper and isopropanol. The constituent elements were placed on the water-cooled copper hearth and a commercial purity titanium ‘getter’ was also placed at the centre of the hearth. The

chamber was sealed and pumped down to a pressure below 0.1 Torr, then backfilled with 0.3 bar of argon and pumped down to 0.1 Torr again. This process was repeated three times in order to reduce the oxygen in the chamber. The chamber was then evacuated to a pressure below 5.0×10^{-5} Torr. Once the vacuum was below this value, 0.7 bar of argon was introduced into the chamber to create an ideal atmosphere for the following melting process.

The ‘getter’ was melted first to consume the remaining oxygen in the chamber and then the constituent elements were melted to form a single master alloy. The master alloy was flipped over and re-melted at least four times to ensure chemical homogeneity of the alloy system. The ‘getter’ was melted prior to each melt of the master alloy. The weight loss of all the alloy ingots after melting was less than 0.1 wt. %. The alloy ingot was removed from the chamber and cleaned using isopropanol before the casting process.

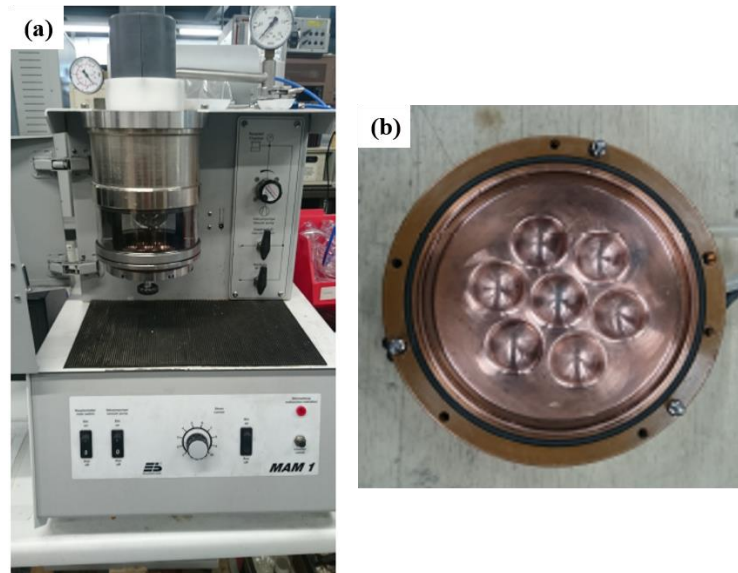


Figure 3.1: (a) MAM1 arc melter configurations for melting. (b) Melting mould.

3.1.3 Copper Mould Suction Casting

A rapid solidification process with the high cooling rate was applied to form BMGs and BMGMCs. A suction casting method was used for this research and the setup is shown in Figure 3. 2 (a) and (b). The master alloys were cast using copper moulds with diameters of 2 mm to 6 mm. The inner surfaces of the copper casting mould were cleaned by a 6 μm diamond paste to remove the dirt, and the outer surfaces were cleaned by using an abrasive paper. This aims to enhance the cooling rates during the casting.

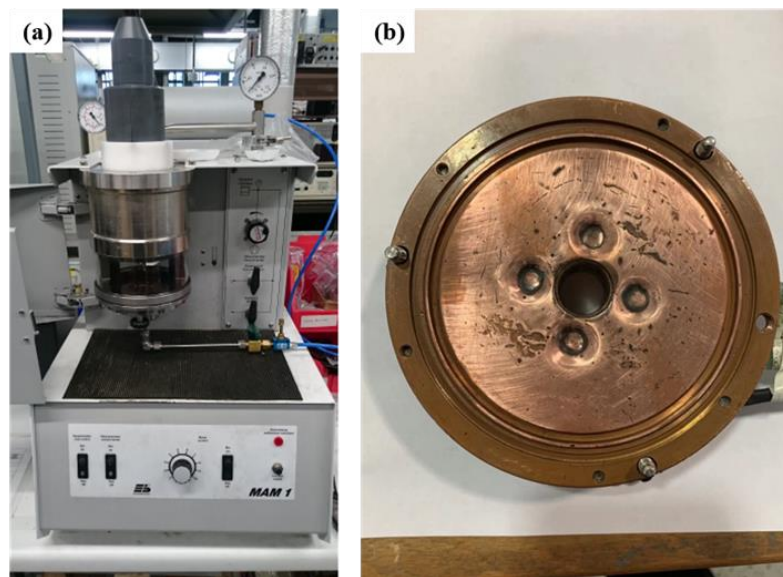


Figure 3.2: (a) MAM1 arc melter configurations for casting. (b) Casting mould.

At the beginning of the casting process, different casting pressures were set with corresponding casting diameters. The rest of the evacuation processes were the same as the melting process described in Section 3.1.2. Once the chamber pressure was below 5.0×10^{-5} Torr, the casting process was performed by melting the titanium ‘getter’ first and then the

master alloy. When the master alloy was fully melted, the pressure valve was released, the molten alloy entered the casting mould and finally solidified in the mould with the desired diameters.

3.2 Characterisation

3.2.1 X-Ray Diffraction (XRD)

An X-Ray Diffraction technique (XRD) was applied to examine amorphous features and crystalline phases. The XRD patterns indicate the Bragg peaks of different kinds of crystalline phases and the amorphous trace can also be detected.

The as-casted rods were cut into thin disks with thicknesses around 1 mm. All the thin disks were polished by abrasive papers to produce flat surfaces. All the disks were cleaned in the ultrasound cleaning machine before the XRD test to avoid impurities. Disks were attached to the sample holder and the number of disks must be enough to cover an area of 1 cm².

A Siemens D5000 X-Ray Diffractometer with a monochromatic radiation source Cu Ka ($\lambda = 0.15418$) was used. The scanning regime was set as follows: step size of 0.05°, step speed of 0.5°/min and diffraction angle (2θ) from 20° to 90°.

3.2.2 Thermal Analysis

Thermal properties of the as-cast rods were examined using Differential Scanning Calorimetry (DSC) and Differential Thermal Analysis (DTA). The GFA of BMGs and BMGMCs can be found through this technique. The crystallization temperature T_x and glass transition temperature T_g can be obtained from the DSC trace. The supercooled liquid region ΔT_x can be calculated ($T_x - T_g$), which indicates the glass forming ability of the BMGs and BMGMCs.

Perkin Elmer Diamond DSC and Perkin Elmer Diamond DTA were used to test these thermal properties. A baseline was set by two empty aluminium pans before each test with the same conditions and then subtracted for the subsequent test. The actual test for each sample with 8–10 mg was placed into one aluminium pan and the other empty pan was used for reference. The heating rates varied between 5–20 K/min up to 800 K with argon flow.

The melting temperature, T_m , and liquid temperature, T_l , were also examined using Perkin Elmer DTA-7. The heating rate was 20 K/min and the sample weight for a single test was 20 mg.

3.2.3 Compression Test

A compression test was applied to examine the mechanical properties of BMGs and BMGMCs. Samples were tested by a ZWICK Z050TH machine at room temperature. The test sample rods were prepared with an aspect ratio (length: width) of 2:1. Five rods were

cut from original as-cast rods in order to ensure reproducibility and statistical properties of the specimens. Both the top and bottom ends of each rod were carefully machine-polished before the test. In order to avoid orthogonal deviation, the parallelism of both ends was precisely controlled and the planarity was also checked by a calliper.

In each test, sample was placed between two compression platens. Sample was set on a foil. Graphite lubricant was applied to the surface between the sample and platen to reduce friction. The strain rate of the compression test was set as $2 \times 10^{-4} \text{ s}^{-1}$ at room temperature. The engineering stress and strain curves were converted to the true stress and strain curves by following equations:

$$\sigma_{TC} = \sigma_{EC}(1 + \varepsilon_{EC}) \quad (3.1)$$

$$\varepsilon_{TC} = \ln(1 + \varepsilon_{EC}) \quad (3.2)$$

where σ_{EC} and ε_{EC} are the engineering stress and strain respectively. σ_{TC} and ε_{TC} are the true stress and strain respectively.

3.2.4 Tensile Test

Tensile test specimens were machined and polished into dumbbell-shaped rods from as-cast rods. The test specimen is shown in Figure 3. 3. The sample gauge dimensions were 1.5 mm \times 8 mm.



Figure 3.3: Tensile test specimen.

Tensile tests were conducted using the ZWICK Z050TH machine with 20 kN load cell and a strain rate of $1 \times 10^{-4} \text{ s}^{-1}$ at room temperature. Five samples were tested for each composition to ensure the reproducibility and statistical properties of the specimens. The tensile sample properties such as 0.2 % proof stress ($R_{p0.2}$), ultimate tensile stress (UTS) and total strain to failure (ϵ_{tot}) were determined. The engineering stress and strain curves were converted to the true stress and strain curves by the following equation:

$$\sigma_{TT} = \sigma_{ET}(1 + \epsilon_{ET}) \quad (3.3)$$

$$\epsilon_{TT} = \ln(1 + \epsilon_{ET}) \quad (3.4)$$

where σ_{ET} and ϵ_{ET} are the engineering stress and strain respectively. σ_{TT} and ϵ_{TT} are the true stress and strain respectively.

3.2.5 Scanning Electron Microscopy

Scanning Electron Microscopy (SEM) was applied to test amorphous features and second phases of the BMGs and BMGMCs. The fracture surfaces after compression and tensile tests were also examined by this technique. FEI Inspect F detector was used with an

accelerating voltage of 15–20 kV, a beam current of 45 μA and a spot size of 5. Both backscatter and secondary electron detectors were used. The energy dispersive spectrometer (EDS) was also applied to analyse the alloy compositions. The SEM samples were mounted using cold resin to avoid crystallisation. The sample was ground with silicon carbide grinding and polishing paper from P120 to P4000. The fine polish was also applied using oil-based diamond suspension from 3 μm to 1 μm . The fractured sample after compression and tensile tests were also examined by this technique.

3.2.6 Transmission Electron Microscopy and High-resolution Transmission Electron Microscopy

The microstructures of BMGs and BMGMCs were examined and studied using transmission electron microscopy (TEM). The TEM specimens were cut from the as-cast rods and deformed samples. The specimens were ground to thin foil specimens with a thickness between 20–30 μm . An ion milling process was conducted on the specimens by Gatan Precision Ion Polishing PIPSII with a beam energy of 2.5 keV and milling angle between 8° – 10° . Liquid nitrogen was added during the ion milling process to prevent unwanted crystallisation. The FEI Tecnai F20 TEM was used for examining amorphous features, crystalline phases and obtaining selected area diffraction (SAED) patterns with an accelerating voltage of 200 kV. The nano-scale features were further inspected using high-resolution TEM (HRTEM). JEOL-2010F and JEOL JEM F200 were used with an

accelerating voltage of 200 kV. All the TEM images were post-processed by a Gatan Digital Micrograph software.

Chapter 4

Investigation of the Effect of Ag Element to the Zr-Cu-Al Bulk Metallic Glass Composites

4.1 Introduction

BMGs have attracted great attention owing to their unique structure and properties. They exhibit high strength, high hardness, large elastic strain limit and good corrosion resistance [1]–[3], [43]. However, the room-temperature brittleness, lack of plasticity and strain-softening behaviour of the monolithic BMGs have strongly limited their applications in the structural and engineering aspects [114]–[116]. To overcome these drawbacks, many approaches have been applied to the BMGs, such as introducing second phase particles into the BMG matrix to form BMGMCs [117]–[120]. Recently, a new concept of introducing TRIP effect to reinforce the BMGMCs has been studied. This effect is achieved by forming a metastable phase into the amorphous matrix; when an external load is applied to the alloy, the phase transformation combined with the amorphous matrix will produce improved plasticity and work hardening behaviour [84], [105], [110], [121]. This idea came from previous research in steels which strongly enhanced the toughness and work-hardening properties. The TRIP effect has been introduced to the ZrCu-based and Ti-based BMGMCs. For the ZrCu-based BMGMCs, the TRIP effect is due to the transformation from the metastable B2-CuZr phase to the martensitic B19' phase during the deformation which has significantly improved the mechanical properties of the alloys.

According to recent research [107], [119], [122], [123], the TRIP reinforced ZrCu-based BMGMCs exhibit enhanced mechanical properties when forming the amorphous phase combined with a single B2-CuZr phase structure. However, most of the single B2-CuZr phase TRIP reinforced Zr-Cu-Al or Zr-Cu-Al-based BMGMC systems exhibit sample size around 2–3 mm for the rod samples. As stated in the recent research, the as-cast sample with microstructure which consists of an amorphous phase and single B2-CuZr phase usually exhibit better plasticity under tension [121]. However, increasing the sample size (reduced cooling rate) will significantly influence the microstructure formation. The brittle phases such as $\text{Cu}_{10}\text{Zr}_7$ and CuZr_2 will precipitate due to the low cooling rate, the volume fraction and morphology of B2-CuZr phase exhibit significant variation with different sample size. Thus, obtaining a single B2-CuZr phase structure with the increasing sample size is desirable for the current researches. In order to increase the sample size, the GFA of the alloy system should be enhanced first and the Ag element has been proved to strongly enhance the GFA of the BMGs according to research, which can form rod sample up to 25 mm in diameter [67][124].

The aim of this chapter is to find a method which will increase the sample size of the traditional Zr-Cu-Al BMGMCs. The alloy design process is explained as: the Zr-Cu-Al alloy system has been selected as the base alloy due to the extensive studies in the recent years. They have exhibited enhanced mechanical properties and the TRIP effect has been successfully obtained for this alloy system. As stated in the previous research, the Al content

will strongly influence the GFA and phase formation of Zr-Cu-Al alloy systems. Moreover, the aim of this chapter is investigating the effect of Ag element on the alloy system, hence the Al content has been fixed. The minor addition of alloying element Ag was introduced to the Zr-Cu-Al alloys. The $Zr_{50}Cu_{45-x}Al_5Ag_x$ ($x = 0, 0.5, 1, \text{ and } 2 \text{ at.}\%$) are prepared, the GFAs, microstructures and mechanical properties of this alloy system are studied.

4.2 Experimental Work

The constituent elements of alloys $Zr_{50}Cu_{45-x}Al_5Ag_x$ ($x=0, 0.5, 1, \text{ and } 2 \text{ at.}\%$) alloys with purity $> 99.9 \%$ were prepared under an argon atmosphere using arc melting. The alloy ingots were melted four times to ensure compositional homogeneity. The weight losses for the alloys after the melting were less than $0.1 \text{ wt.}\%$. The ingots were then fabricated into rod shapes with 3–6 mm diameters using copper mould suction casting. The amorphous features and crystalline phases were examined using the Siemens D5000 XRD with the monochromatic radiation source Cu Ka, and the diffraction angle (2θ) was set between 30° and 80° . The GFAs and thermal properties were examined using the Perkin Elmer Diamond DSC with a heating rate of 20 K min^{-1} . Room temperature compression tests were carried out by a Zwick machine with a maximum load of 50 kN at an engineering strain rate of $2 \times 10^{-4} \text{ s}^{-1}$. The microstructure nature of the as-cast samples and fracture samples were investigated by the FEI Inspect F SEM and FEI Tecnai TEM. The specimens for the TEM were ground and polished to 20 micrometres before the ion milling process was applied.

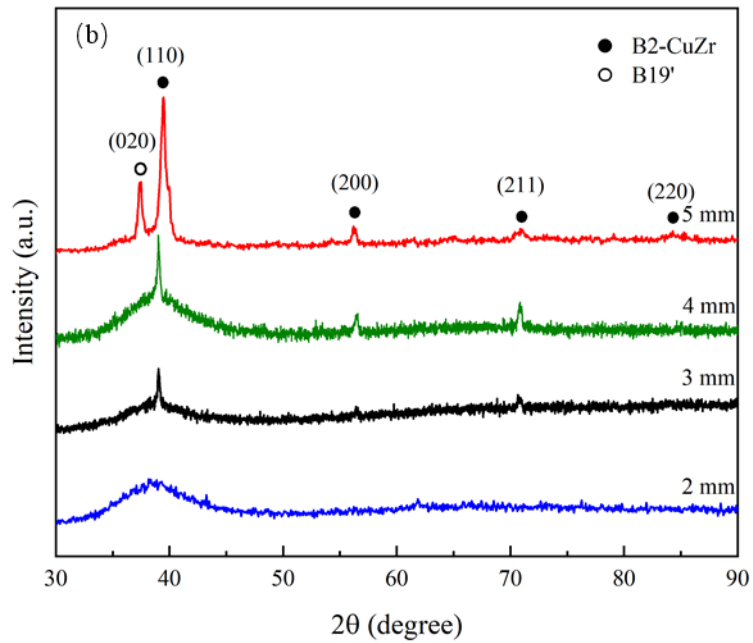
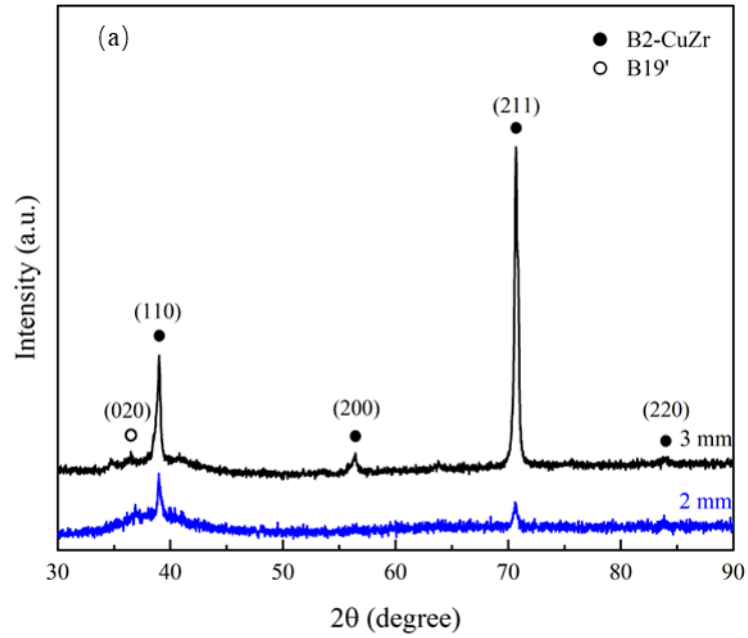
The Gatan PIPS Ion Milling device was used under the liquid nitrogen cooling condition in order to prevent unpredicted crystallisation induced by the heating from the machine [125].

4.3 Results and Discussions

4.3.1 Microstructure features of as-cast samples

Figure 4. 1 (a)–(d) shows the XRD patterns of as-cast $Zr_{50}Cu_{45-x}Al_5Ag_x$ ($x = 0, 0.5, 1,$ and 2 at. %) alloy. The $Zr_{50}Cu_{45}Al_5$ base alloy exhibits a composite structure which consists of an amorphous phase and single B2-CuZr phase with 2 mm sample size. When the casting diameter is 3 mm, the Al_2Zr phase is also observed from the XRD curve. For the $Zr_{50}Cu_{44.5}Al_5Ag_{0.5}$, it exhibits a fully amorphous structure up to 2 mm. The 3 mm sample shows a single B2-CuZr phase structure. From 4 mm and onwards, the $Cu_{10}Zr_7$ phase and B19' martensite phase is observed. For the $Zr_{50}Cu_{44}Al_5Ag_1$ specimen, it exhibits a fully amorphous structure up to 2 mm. This alloy composition exhibits a single B2-CuZr phase structure from 3 mm to 5 mm. The B19' martensitic phase and $Cu_{10}Zr_7$ brittle phases are obtained in 6 mm sample. For the $Zr_{50}Cu_{43}Al_5Ag_2$ sample, it exhibits a fully amorphous feature up to 3 mm. The microstructure becomes a single B2-phase structure when the casting diameter is 4 mm diameter. The $Cu_{10}Zr_7$ phase is observed when the casting diameter reaches 5 mm. The XRD results indicate that the Ag content has significantly enhanced the GFA of the Zr-Cu-Al base alloy, the fully amorphous structure can be obtained up to 4 mm.

which enables the alloys to form the same microstructures even with the reduced cooling rate (larger sample size).



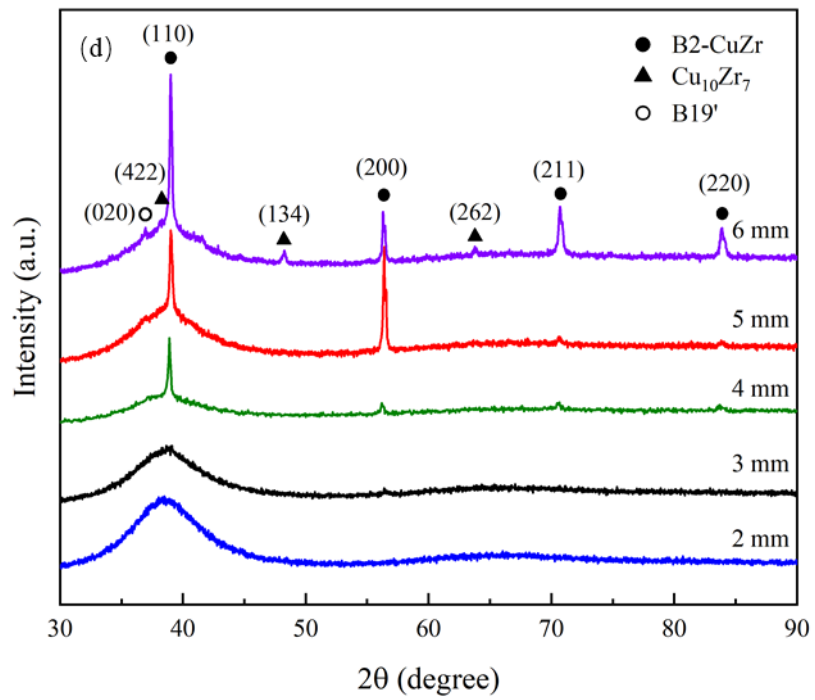
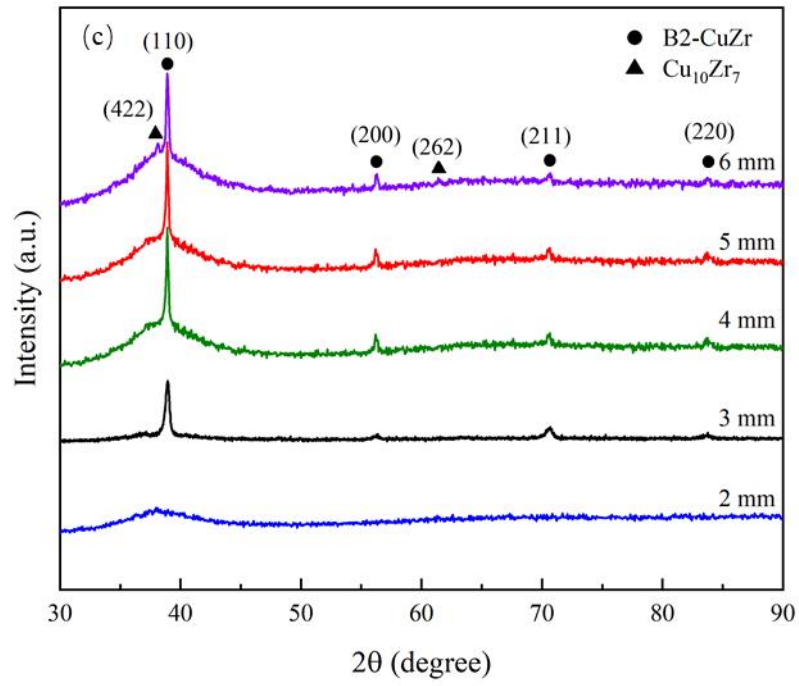


Figure 4.1: XRD patterns of the as-cast $Zr_{50}Cu_{45-x}Al_5Ag_x$ ($x = 0, 0.5, 1, \text{ and } 2$ at. %) alloys with different cooling rate (sample size): (a) $x = 0$, (b) $x = 0.5$ (c) $x = 1$, (d) $x = 2$. The Ag content has significantly enhanced the GFA of the Zr-Cu-Al base alloy.

Figure 4. 2 shows phases present in this $Zr_{50}Cu_{45-x}Al_5Ag_x$ ($x = 0, 0.5, 1, \text{ and } 2$ at. %) alloy system has strong dependence on the Ag content and sample size (cooling rate). The minor addition of Ag element has enhanced the GFA of the base alloy and leads to the formation of fully amorphous structure up to 3 mm. It is also found that with the suitable alloy composition and cooling rate, the single B2-CuZr phase can be retained during the cooling process without the formation of B19' martensitic phase, $Cu_{10}Zr_7$ and $CuZr_2$. The Ag element has enlarged the sample size range which can form single B2-CuZr phase, compared with the base alloy. The phase formation of the alloys exhibits big differences with the sample size (cooling rate), even with the same Ag content. Increasing sample size will contribute to the decrease of cooling rate, the microstructure changes from fully amorphous structure to amorphous combined with single B2-CuZr phase structure and finally becomes a structure which consists of amorphous structure, B2-CuZr phase and other brittle phases. The formation of single B2-CuZr phase structure can only be retained with specific alloy compositions and cooling rate.

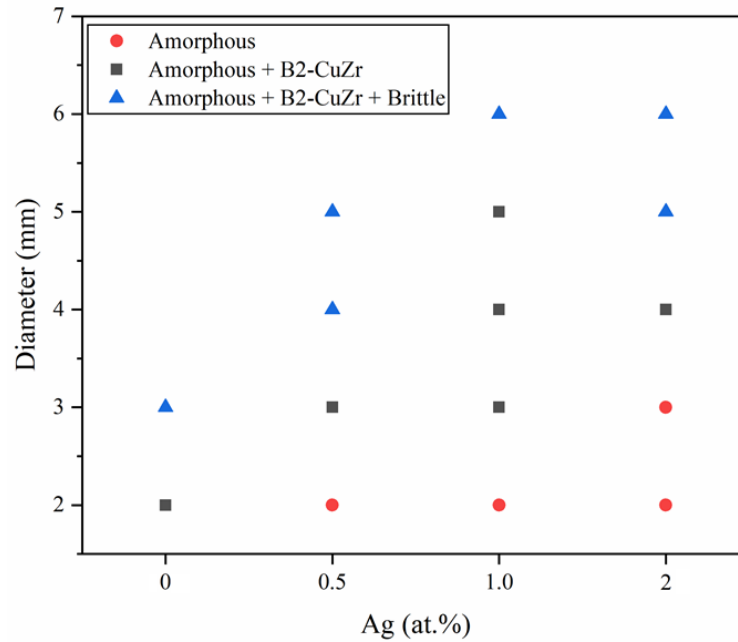


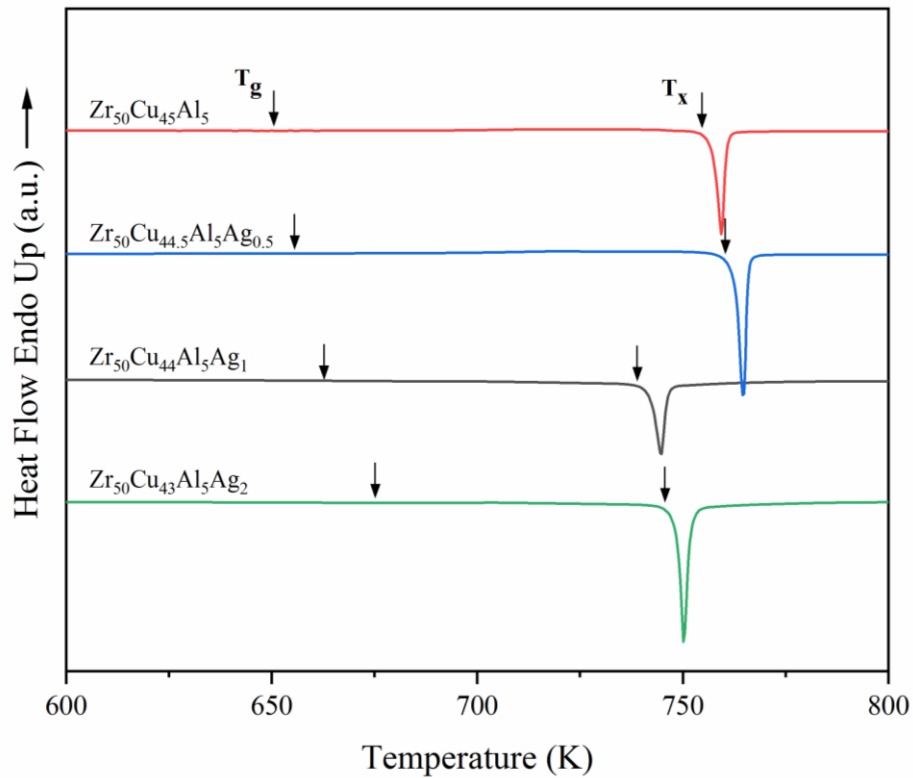
Figure 4.2: Microstructure variations with Ag content and sample size (cooling rate) of $Zr_{50}Cu_{45-x}Al_5Ag_x$ ($x = 0, 0.5, 1, \text{ and } 2 \text{ at. } \%$) alloy system.

xAl_5Ag_x ($x = 0, 0.5, 1, \text{ and } 2 \text{ at. } \%$) alloy system.

4.3.2 Thermal properties of as-cast samples

The effect of Ag on the GFA and thermal properties of as-cast samples are further examined by DSC. Figure 4. 3 shows the DSC curves of the $Zr_{50}Cu_{45-x}Al_5Ag_x$ ($x = 0, 0.5, 1, \text{ and } 2 \text{ at. } \%$) alloy system. The glass transition temperature (T_g), crystallisation temperature (T_x) and supercooled liquid region (ΔT_x) can be obtained from the DSC results. When the material passes T_g , the baseline will move towards the endothermic direction and form a step. As shown in the Figure 4.4, A is the point which starts to deviate from the base line and D is point where deviation ends. The baseline is extended from both point A and D. Point C is the half vertical distance between the two lines. Making tangent from point C and intersect with the baseline is point B which is T_g . The results indicate that the T_g value of the

base alloy increased from 649 K to 676 K which further proves the Ag element has enhanced amorphous phase stability. As discussed in the previous XRD results, the size of the fully amorphous sample increases with the Ag contents. According to the Inoue's empirical rule the larger the ΔT_x the better GFA of the alloys. However, the current alloy series, $Zr_{50}Cu_{44.5}Al_5Ag_{0.5}$ sample exhibits the largest ΔT_x values. The variations of these thermal properties may due to competition between the B2-CuZr phase and amorphous matrix during cooling process.



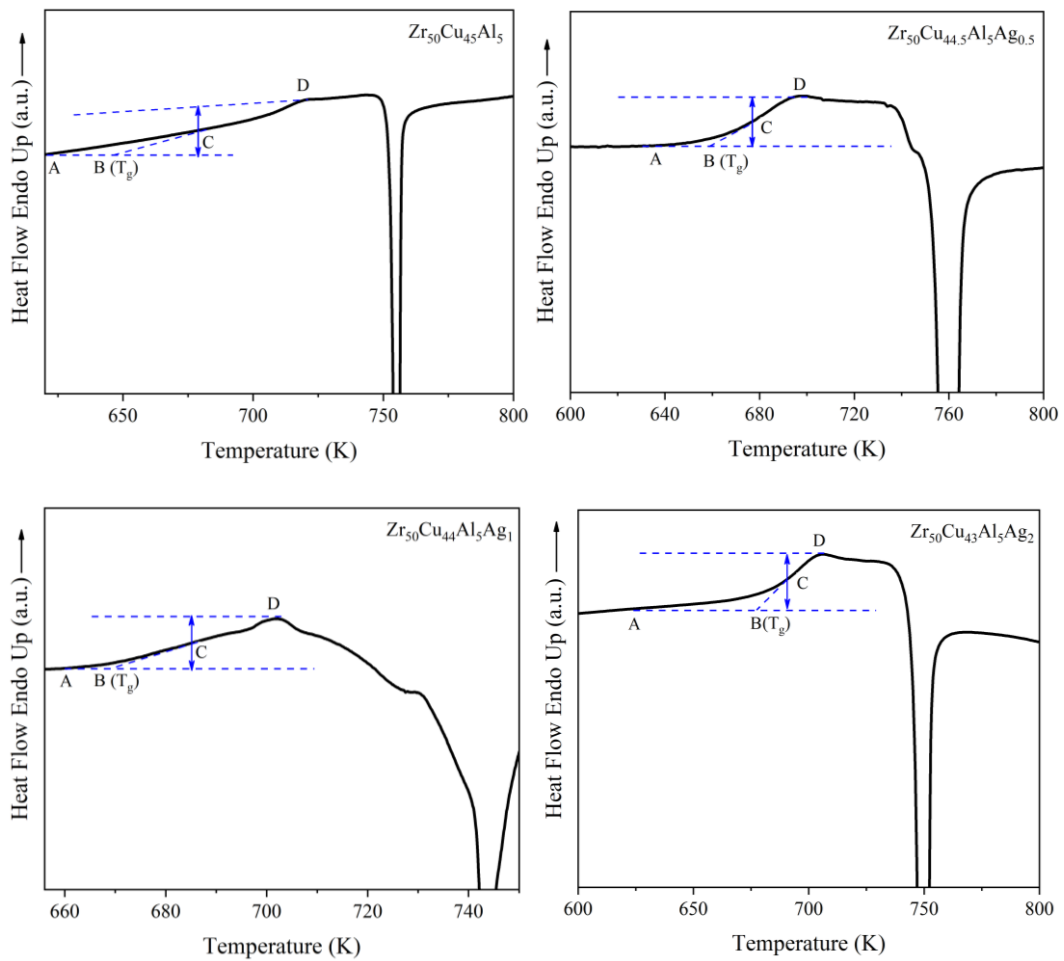
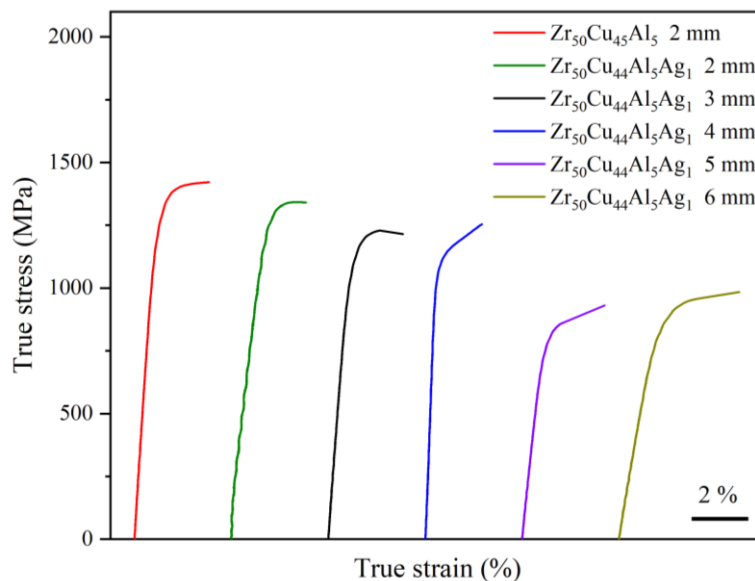


Figure 4.3: DSC curves of the as-cast 3 mm $Zr_{50}Cu_{45-x}Al_5Ag_x$ ($x = 0, 0.5, 1, \text{ and } 2$ at. %) alloy system. The determination of T_g is shown below the DSC curves.

4.3.3 Mechanical properties

In order to examine the mechanical properties of the current alloy system, the $Zr_{50}Cu_{44}Al_5Ag_1$ alloy series is selected and tested by the compression tests, due to the wider range of single B2-CuZr phase structure. The compression test stress-strain curves of all the $Zr_{50}Cu_{44}Al_5Ag_1$ specimens and the 2 mm $Zr_{50}Cu_{45}Al_5$ base alloy specimen are shown in the Figure 4. 4. The compression test results exhibit very big differences among the specimens.

The alloys exhibit a yield strength range between 763 MPa to 1325 MPa, and the plasticity range from 0.3 % to 2.4 %. The base alloy exhibits a yield strength of 1325 MPa and a plastic strain of 1.8 %. The 2 mm $Zr_{50}Cu_{45}Al_5Ag_1$ specimen exhibits a typical BMG compression curve which exhibit a fracture strength of 1650 MPa and 0.3 % plasticity. The 3 mm specimen shows a yield strength of 1368 MPa with a plastic strain of 1.3 %. Furthermore, the 4 mm specimen exhibits a yield strength of 1221 MPa and the best plasticity of 2.3 % among all the specimens. The fracture strength is 1700 MPa, and the stress increase with the plastic strain behaviour is observed in this specimen. The increased plasticity of this alloy is mainly due to the work-hardening behaviour caused by the phase transformation during the deformation. The 5 mm specimen exhibits a yield strength of 838 MPa with a plastic strain of 2.1 %. The 6 mm specimen exhibits a yield strength with 943 MPa and a plasticity of 1.9 %.



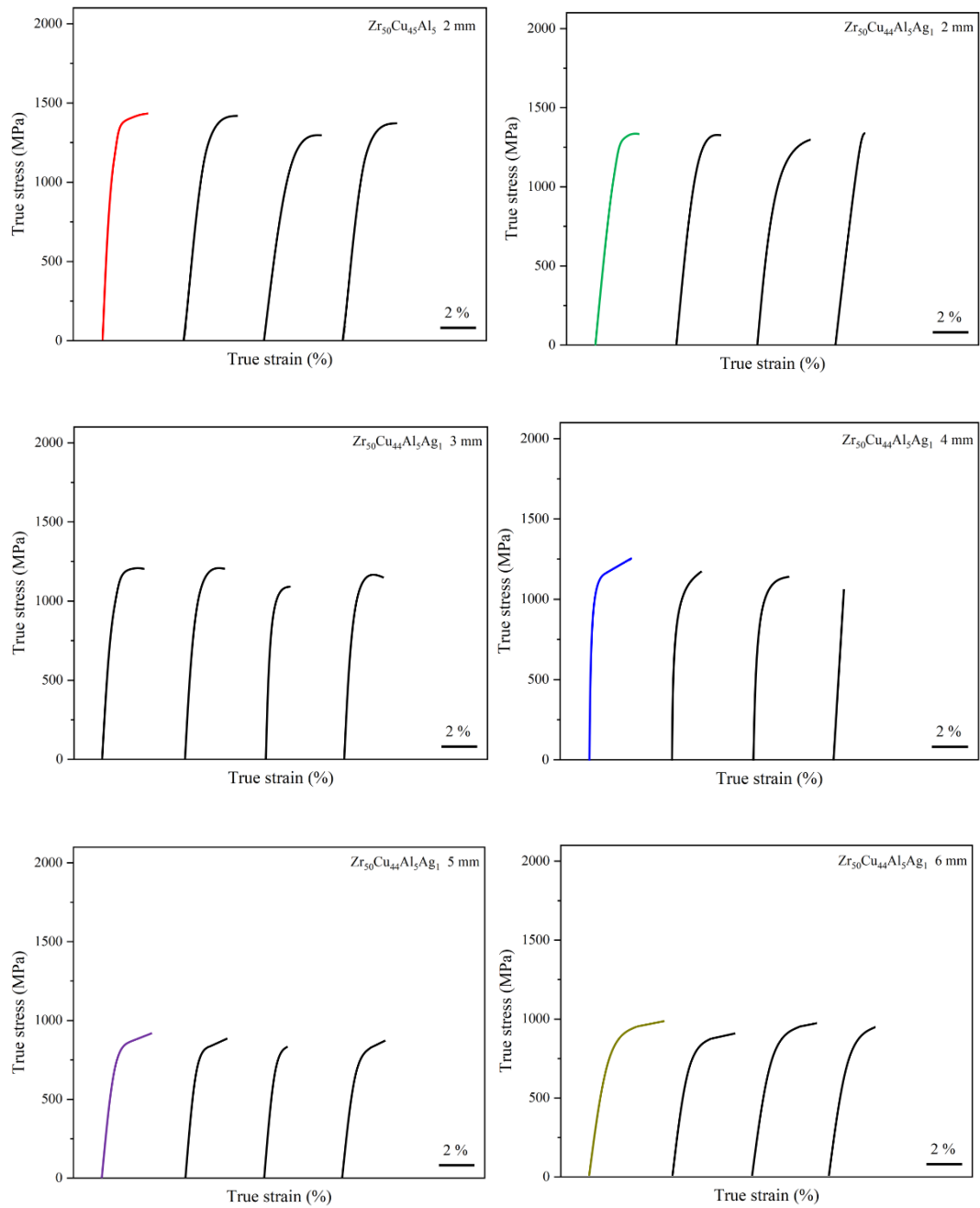


Figure 4.4: Room-temperature compression test curves of as-cast 2 mm $Zr_{50}Cu_{45}Al_5$ base alloy and 2–6 mm $Zr_{50}Cu_{44}Al_5Ag_1$ alloys. The repeat results are shown separately.

According to the XRD results, the 2 mm $Zr_{50}Cu_{44}Al_5Ag_1$ sample has a fully amorphous feature, and the compression result shows a typical amorphous alloy compression curve. The 6 mm $Zr_{50}Cu_{44}Al_5Ag_1$ has a structure which consists of amorphous phase, B2-CuZr phase and other brittle phases, the compression curve exhibits very similar behaviour as fully crystalline materials. The compression test results satisfy the microstructure of these two alloys. However, the 3–5 mm samples have the same microstructures but they show big differences upon compression tests. All the alloys have not exhibited significant mechanical properties improvements compared with the base alloy.

As a result, the microstructure of as-cast 3–5 mm $Zr_{50}Cu_{44}Al_5Ag_1$ samples are examined by the SEM. Figure 4.5 (a)–(c) shows the morphology of the 3–5 mm samples respectively. When the sample size is 3 mm, the spherical B2-CuZr particles precipitate on the amorphous matrix with size 65–200 μm and volume fraction is 11 %. The grey part shows the glass matrix and the dark parts are the B2 phases. For the 4 mm sample, the volume fraction further increases to 37 % and the size of the B2-CuZr phase has been increased up to 500 μm . When the sample size reaches 5 mm, the volume fraction reaches 83%. The spherical shaped phase is no longer be observed, instead of patch-like shapes. This phenomenon is due to the ‘Soret effect’ of the BMGs [110]. The large temperature gradient is formed during the rapid cooling process of BMGs results in composition inhomogeneity. Increasing the casting size will lead to the decrease of cooling rate and there will be more room for the

thermal diffusion process. The large compositional inhomogeneity will occur due to the above reason.

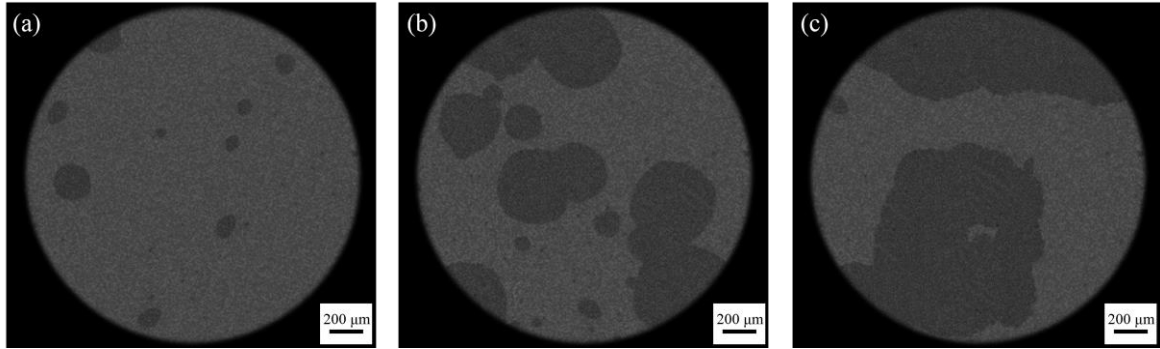


Figure 4. 5: SEM images of the as-cast (a) 3 mm (b) 4 mm (c) 5 mm $Zr_{50}Cu_{44}Al_5Ag_1$ BMGMCs.

By comparing the SEM results with the compression results, the volume fraction of the B2-CuZr phase and morphology of the sample microstructure has great influence for the current alloy system. A more homogenised distribution of the B2-CuZr phase will contribute the better mechanical performance. The patch-like pattern indicates the formation of large amount of B2-CuZr phase, and trigger a random distribution of the B2-CuZr phase. The volume fraction of the B2-CuZr phase is also a key parameter for the enhanced mechanical property. For the current alloy system, the mechanical variation among the samples may mainly due to the above reason, the microstructure of the alloy system exhibits big differences with the increase of sample size. The current alloy system has not exhibited significantly enhanced properties compared with the base alloy. However, the main output of the current chapter is by introducing the Ag element into the base alloy, the GFA of the

base alloy have been significantly enhanced and the single B2-CuZr phase can be obtained with sample size up to 5 mm.

4.4 Conclusion

The Zr-Cu-Al-Ag₁ alloy exhibits a relatively large range of forming single B2-CuZr phase microstructure. The mechanical properties exhibit large variations due to the volume fraction of the B2-CuZr phase and the formation of other brittle phases such as Zr₁₀Cu₇ during the casting process

The results of this chapter have produced a general view of the Ag content influence of the base Zr-Cu-Al alloy system. However, the single B2-CuZr phase can be obtained from the current alloy system, the large grain size and variation of volume fraction still have strong effect to the alloy system. The single B2-CuZr phase combined with amorphous phase structure can only be obtained with a suitable composition range and cooling rate. It should satisfy both thermodynamics and kinetics equilibrium. For the current study the Ag₁ alloy exhibit a exhibited a wider range of an amorphous and B2-phase structure and enhanced glass forming ability compared with the base alloy, and it was chosen as the base alloy for the following studies.

Chapter 5

Formation of Zr-Cu-Al-Ag-Ti Bulk Metallic Glass Composites with Enhanced Work-Hardening Ability and Plasticity

5.1 Introduction

BMGs exhibit high strength, large elastic limit, high yield strength and high hardness due to the long-range disordered and short-range ordered structural characteristics, which makes them attract significant attention [3], [43]. However, this unique structure also leads to room temperature brittleness and lack of plasticity, which has strongly limited their applications in engineering materials [19], [126]. In order to conquer these problems, the formation of BMGMCs has been introduced and proven to be an effective way to improve the mechanical properties of BMGs [4], [19], [23], [126]. During the development of BMGMCs, a variety of concepts has been investigated, such as in-situ formation of ductile crystalline phases in the glass matrix [81], [82], [127]–[129]. In contrast, the lack of work hardening behaviour is still a challenge for BMGMCs. As discussed in the Chapter 4, the TRIP effect has been found in the Zr-Cu-Al-Ag BMGMCs. However, the sample size and microstructure instability strongly affect this TRIP reinforced Zr-Cu-Al-Ag BMGMCs.

According to the literature and the last chapter's results, the specimens which consist of the amorphous phase and B2-CuZr phase microstructure exhibit better mechanical

properties [33]. As a result, the $Zr_{50}Cu_{44}Al_5Ag_1$ alloy system was selected as the base alloy because it formed an amorphous and B2-CuZr phase structure up to 5 mm. In order to further increase the sample size and enlarge the single B2-CuZr structure range, Ti was introduced to the base alloy by partially replacing Zr. The reasons for selecting Ti as an additional element are: (i) Ti addition will affect the thermal stability of B2-CuZr phase according to the recent research [31][130]; (ii) Ti has zero heat of mixing with Zr and large negative heat of mixing with Cu, Al and Ag (as shown in Table 5. 1) [131], it will enhance the GFAs by stabilising the liquid phase according to the empirical rules and further raise the chance to obtain medium/large-sized samples that contain amorphous phase and B2-CuZr phase microstructures; (iii) Ti and Zr have similar chemical properties as they are in the same group in the periodic table; (iv) Ti and Zr tend to form a homogeneous solid solution [132]. As a result, Ti is added to the alloy system.

In summary, the aim of this chapter is to design a new series of ZrCu-based TRIP reinforced BMGMCs based on the last chapter's results with improved mechanical properties and increased sample size. In the following sections, the $Zr_{50-x}Cu_{44}Al_5Ag_1Ti_x$ ($x = 0.5, 1, 2, 3, 4$ and 5 in at.%) alloy systems are designed and the effect of Ti addition on the alloy systems are investigated. A wide range of B2-CuZr phase structure is obtained throughout adjusting Ti content. The alloys are named as $Ti_{0.5}$, Ti_1 , Ti_2 , Ti_3 , Ti_4 and Ti_5 for convenience.

5.2 Experimental Work

The constituent elements of $Zr_{50-x}Cu_{44}Al_5Ag_1Ti_x$ ($x = 0.5, 1, 2, 3, 4$ and 5 in at. %) alloys with purity $> 99.9\%$ were prepared under an argon atmosphere using arc melting. The alloy ingots were melted four times to ensure compositional homogeneity. The weight losses for the alloys after the melting were less than $0.1\text{ wt. }%$. The ingots were then fabricated into rod shapes with $3\text{--}6\text{ mm}$ diameters using copper mould suction casting.

The amorphous features and crystalline phases before and after the mechanical tests were examined using the Siemens D5000 XRD with the monochromatic radiation source Cu K α , and the diffraction angle (2θ) was set between 30° and 80° . The GFAs and thermal properties were examined using the Perkin Elmer Diamond DSC and DTA with a heating rate of 20 K/min^{-1} . Room temperature compression tests were carried out using a Zwick machine with a maximum load of 50 kN at an engineering strain rate of $2 \times 10^{-4}\text{ s}^{-1}$. The tensile tests were conducted using the same machine with an engineering strain rate of $2 \times 10^{-4}\text{ s}^{-1}$ at room temperature. A camera was applied to calibrate and measure the strain during the tests. The microstructure nature of the as-cast samples and fracture samples were investigated by using the FEI Inspect F SEM and FEI Tecnai TEM. More detailed crystalline structures were further examined in the JEOL 2010 HRTEM. The specimens for the TEM were ground and polished to 20 micrometres before the ion milling process.

Table 5. 1: Heat of mixing (kJ/mol) for the binary systems of the Zr, Cu, Al, Ag and Ti elements

[131].

| ΔH^{mix} | Zr | Cu | Al | Ag | Ti |
|------------------|----|-----|-----|-----|-----|
| Zr | 0 | -23 | -44 | -20 | 0 |
| Cu | | 0 | -1 | +2 | -9 |
| Al | | | 0 | -4 | -30 |
| Ag | | | | 0 | -2 |
| Ti | | | | | 0 |

5.3 Results and Discussion

5.3.1 Microstructures of as-cast samples

The microstructures of as-cast rods were first examined using XRD. Figure 5.1 shows the XRD patterns of as-cast 3 mm $Zr_{50-x}Cu_{44}Al_5Ag_1Ti_x$ ($x=0.5, 1, 2, 3, 4$ and 5 at. %) alloys. All the alloys have a broad hump at $2\theta = 38^\circ-39^\circ$, which proves the formation of amorphous structure. The Ti_1-Ti_5 alloys exhibit a fully amorphous structure without any clear sharp peaks. The $Ti_{0.5}$ sample presents a small sharp peak on the amorphous hump which is B2-CuZr phase. The results indicate the addition of the Ti element will enhance the GFA of the Zr-Cu-Al-Ag base alloy and increase the fully amorphous phase structure sample critical diameter to 3 mm. Considering the aim of this chapter, to fabricate samples which consist of single B2-CuZr phase and amorphous phase microstructure with increased sample size,

all the alloys are then cast into 6 mm sample size. The XRD patterns of 6 mm samples are shown in Figure 5. 2. For the $Ti_{0.5}$ specimen, both B2-CuZr phase and B19' martensite phase are observed. For the Ti_1 specimen, with an increase of sample size, the B2-CuZr phase is found and all the crystalline peaks are B2-CuZr phase peaks. Comparing with the results in Chapter 4, the size of sample which consists of amorphous plus B2-CuZr phase structure has been increased from 5 mm to 6 mm. For the rest of 6 mm samples, the B2-CuZr phase, B19' martensite phase and $Cu_{10}Zr_7$ phase can be found from the XRD patterns. Increasing the sample size will reduce cooling rate and further reduce the of GFA and contribute to the formation of brittle phases for these four compositions. The cooling rate cannot prevent partial decomposition of the B2-CuZr phase. The $CuZr_2$ phase exhibits more sluggish behaviour due to Zr diffusing slower than Cu, as a result, the $Cu_{10}Zr_7$ phase usually precipitates first [133]. The Ti_1 alloys show a wide range of casting size with amorphous plus B2-CuZr phase structure. The B2 phase is at the dominate position and confirms that some of the B2 phases are very stable during the casting process. The results indicate a suitable amount of Ti suppresses the diffusional transformation of this metastable B2-CuZr phase into a mixture of stable $Cu_{10}Zr_7$ and $CuZr_2$. However, a small amount of Ti such as 0.5 at. % cannot suppress the formation of these brittle phases with reduced cooling rate. Introducing more Ti will enhance the amorphous phase and destabilise B2-CuZr phase. The results prove that the amorphous plus B2-CuZr structure sample can only be obtained with suitable Ti contents and cooling rate.

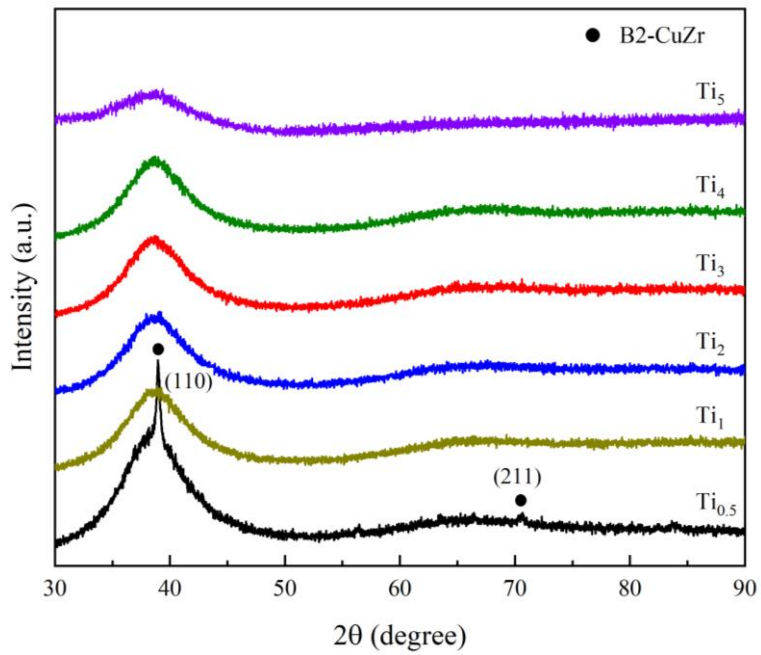


Figure 5.1: XRD patterns of as-cast 3 mm $Zr_{50-x}Cu_{44}Al_5Ag_1Ti_x$ ($x=0.5, 1, 2, 3, 4$ and 5 at %) alloys.

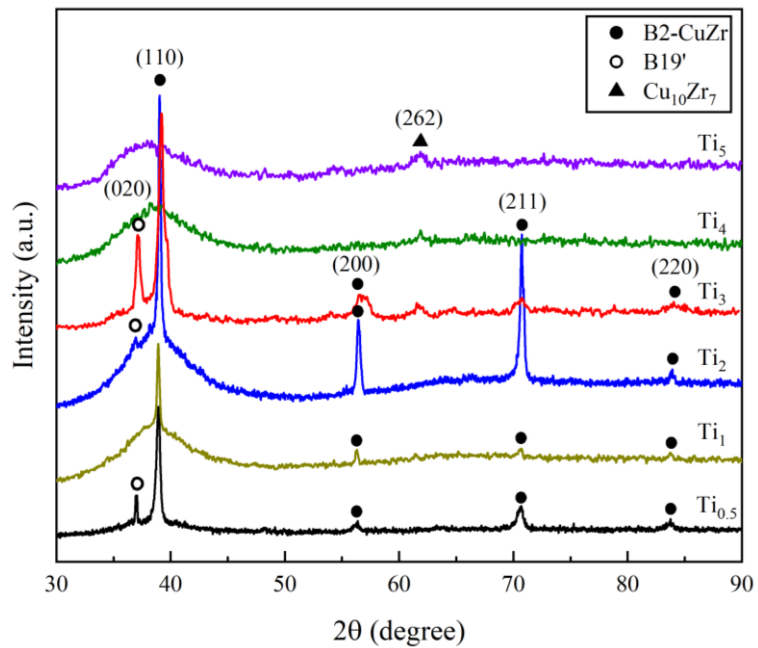


Figure 5.2: XRD patterns of as-cast 6 mm $Zr_{50-x}Cu_{44}Al_5Ag_1Ti_x$ ($x=0.5, 1, 2, 3, 4$ and 5 at %) alloys.

The Ti₁ sample exhibits the widest range of forming amorphous plus B2-CuZr structure, and the as-cast 3 mm sample was first examined using HRTEM as shown in Figures 5. 3 (a) and (b). Figure 5. 3 (a) depicts the general morphology of the sample which exhibits an amorphous phase. It is interesting to find that there are some lattices embedded in the glass matrix which are marked by a yellow circle, the inset shows the fast Fourier transformation (FFT) image of the selected region. Figure 5. 3 (b) shows the enlarged area of lattice structure. Large-sized crystalline features are not detected for this specimen.

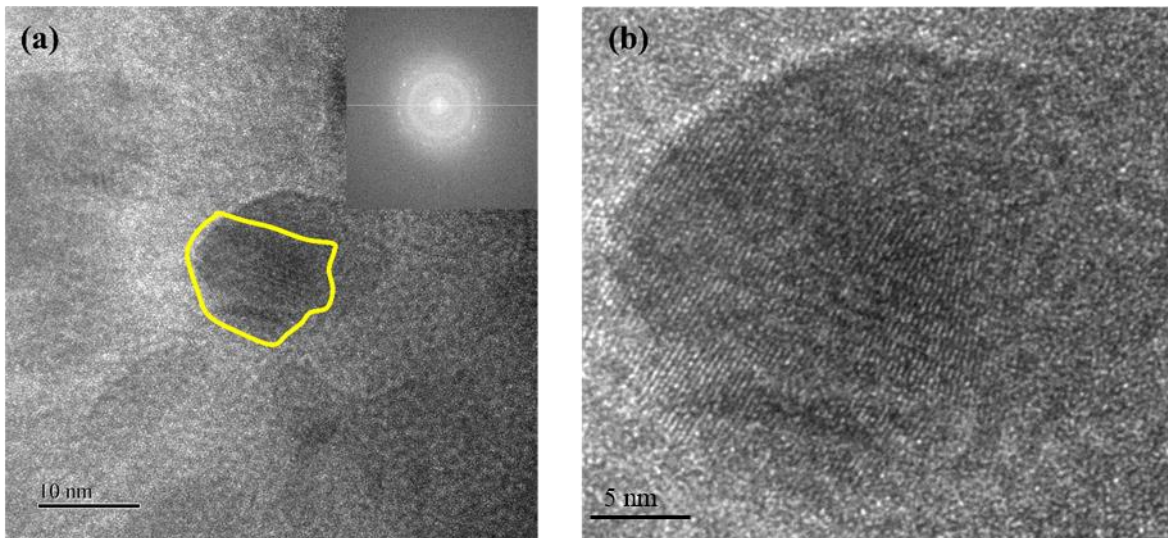


Figure 5.3: (a) The HRTEM images of the as-cast 3 mm Zr₄₉Cu₄₄Al₅Ag₁Ti₁ sample with lattice feature marked by yellow circles. (b) The enlarged area of the lattice structure and the corresponding SADP.

The microstructure features of as-cast 6 mm Ti₁ sample are also examined, as shown in Figure 5. 4 (a)–(d). Figure 5.4 (a) shows the BF-TEM image of the sample, the darker nano-sized B2-CuZr phase is clearly observed in the amorphous matrix which exhibits spherical

shapes with varying size between 15–40 nm. Figure 5. 4 (b) shows the HRTEM image of the interface between the ordered atomic structure and amorphous structure. Figure 5. 4 (c) presents the HRTEM image of the spherical crystalline phase. The measured d-spacing is 0.237 nm and it shows a similar result with the published B2-CuZr phase. The inset shows the corresponding SAED pattern, which further proves the formation B2-CuZr phase. Figures 5. 4 (d) shows the SEM image of the sample, the large-sized B2-CuZr phase particles can be clearly observed and are homogenous distributed in the amorphous matrix. The sizes are generally below 50 μm . The volume fraction of the B2-CuZr phase is 25 %. The formation of the B2-CuZr phase in the amorphous matrix can be also clearly observed. The B19' martensitic phase is not detected in this as-cast specimen which agrees with the XRD results. Increasing the sample size of this alloy system did not cause the dramatic microstructure variations. Introducing addition of Ti has strongly enhanced the GFA and the B2-CuZr particles are homogenous distributed in the 6 mm sample which contributes to the enhanced mechanical properties with a relatively large-sized sample.

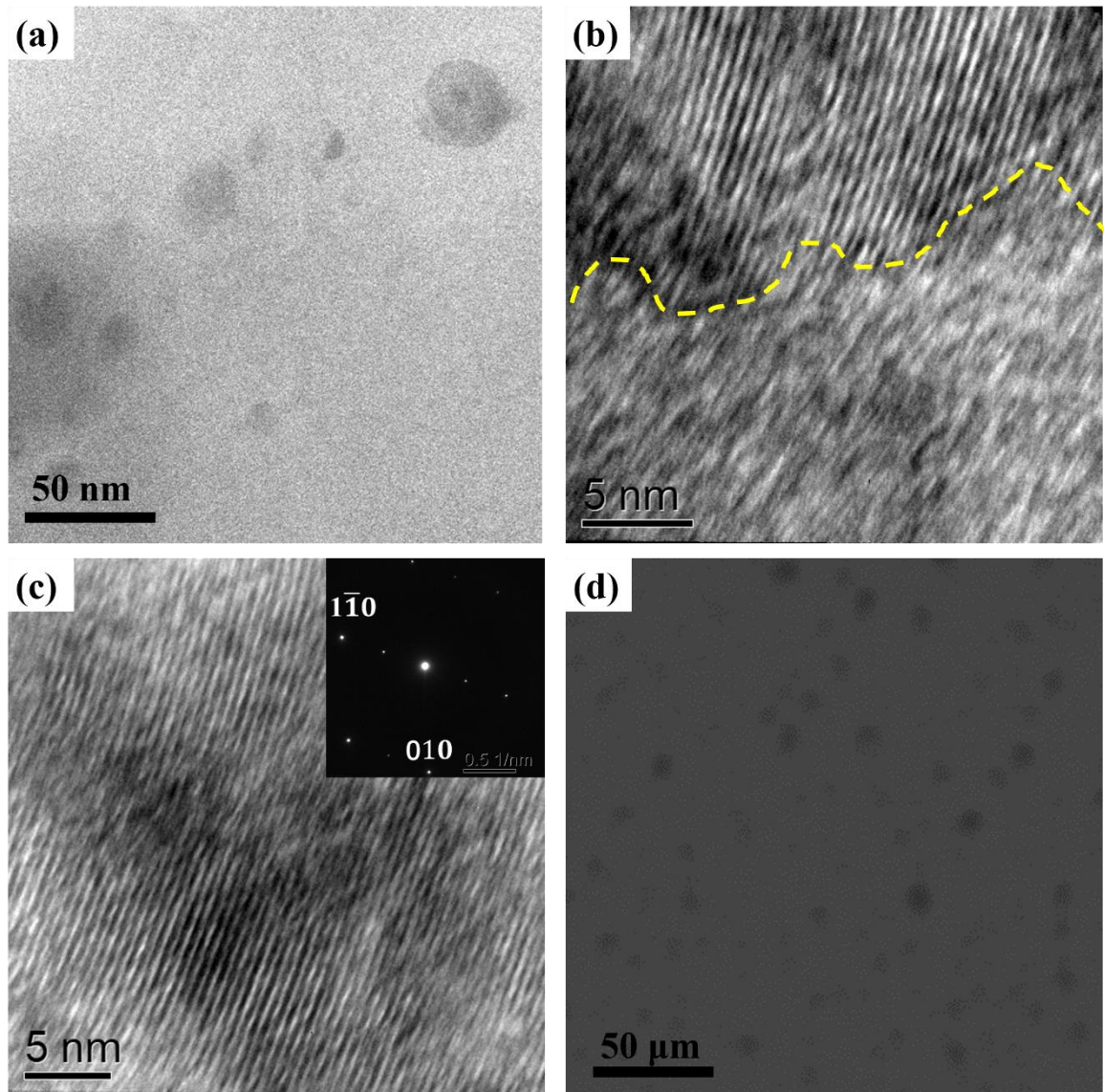


Figure 5.4: (a) The BF-TEM image of the B2-CuZr phase embedded on the amorphous matrix. (b)

HR-TEM micrograph of as-cast 6 mm Ti₁ alloy, shows the interface between the amorphous matrix and crystalline B2-CuZr phase. (c) The TEM image of the B2-CuZr phase. The inset shows the SAED pattern of B2-CuZr phase taken from zone-axis [0 1 0]. (d) SEM image of the B2-CuZr particles and the amorphous matrix.

5.3.2 Thermal properties of as-cast samples

The effect of Ti content on the thermal stability and thermodynamic properties of this alloy system were further investigated and examined using DSC and DTA. Figure 5.5 shows the DSC traces of 3 mm Ti_{0.5}, Ti₁, Ti₂, Ti₃, Ti₄ and Ti₅ obtained under continuous heating with a heating rate of 20 K/s. The T_g and T_x values are obtained from the curves and marked on the curves with arrows. The results from the DSC curves indicate that with an increase in temperature, all the samples experienced a glass transition into an undercooled liquid and then the crystallisation process occurred. The T_g value increases from 673 K to 680 K and the T_x values ranging between 738 K to 748 K, which indicates that by increasing the Ti content from 0.5 to 5, the thermal stability of the amorphous phase increased. The sharp crystallisation peak can be found for the Ti_{0.5} to Ti₃ alloys, while Ti₄ and Ti₅ exhibit two-step exothermic events with two exothermic peaks. The variation of T_g , T_x and ΔT_x with Ti content are summarised in Table 5.2. The calculated ΔT_x values show that the supercooled liquid region has a relatively large range and further enhances the GFAs.

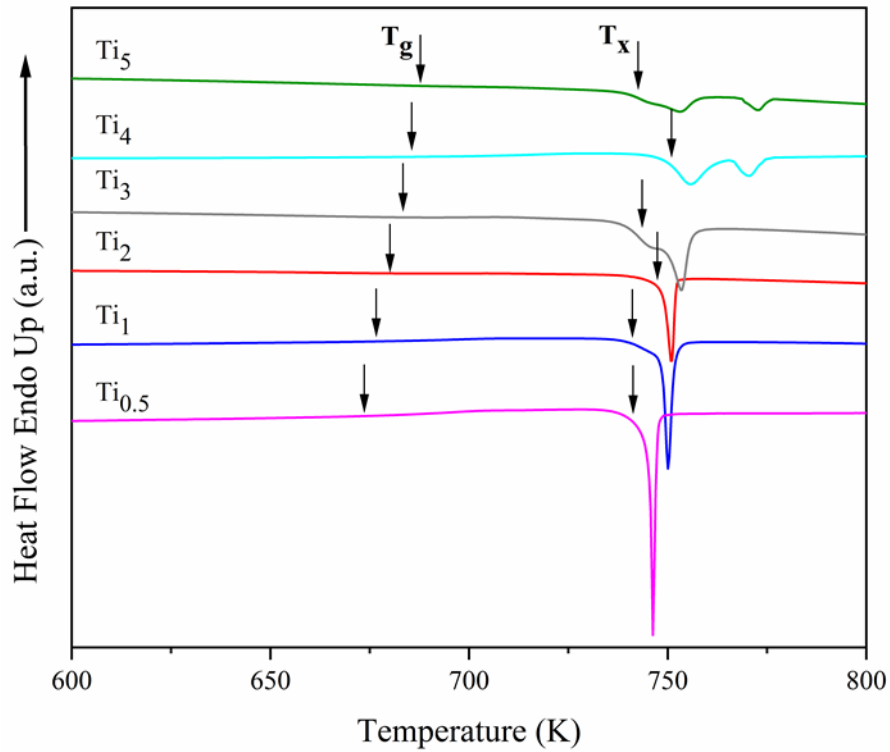


Figure 5.5: DSC trace of as-cast $Zr_{50-x}Cu_{44}Al_5Ag_1Ti_x$ ($x=0.5, 1, 2, 3, 4$ and 5 at %) specimens.

According to recent research, there will be a eutectoid phase transformation at high temperatures for the CuZr-based BMGMCs [130]. The low-temperature equilibrium phases such as $Cu_{10}Zr_7$ and $CuZr_2$ will transform into B2-CuZr phases during continuous heating. A new parameter K was defined, which equals T_f/T_L where T_f is the final temperature of the B2-CuZr phase transformation and T_L is the liquidus temperature. This parameter was suggested to predict the tendency of forming B2-CuZr phase in different CuZr-based BMGMC alloy systems. The reason for using these values is that the nucleation and growth rate of the CuZr intermetallic are governed by the precipitation driving force and this can be assessed by the Gibbs energy of the CuZr intermetallic. Equation 6.1 expresses the Gibbs energy of the CuZr intermetallic.

$${}^0G_m^{CuZr} = 0.5{}^0G_{Cu}^{fcc} + 0.5{}^0G_{Zr}^{hcp} + \Delta^0G_f^{CuZr} \quad (6.1)$$

where ${}^0G_{Cu}^{fcc}$ and ${}^0G_{Zr}^{hcp}$ represent the molar Gibbs free energy of *fcc* Cu and *hcp* Zr in the CuZr intermetallic respectively. The ΔG_f^{CuZr} can be expressed as $\Delta G_f^{CuZr} = a + bT$, where a and b are parameters to be evaluated based on some thermodynamic models. Therefore, the Gibbs free energy of the equiatomic CuZr intermetallic should be roughly evaluated by the phase transformation temperature T_f .

In order to check the thermal stability of B2-CuZr phase in this Zr-Cu-Al-Ag-Ti alloy system, DTA was applied for high-temperature measurements to obtain the eutectoid phase transformation parameters K , T_f and T_L . Figure 5.6 shows the DTA results of the Ti_{0.5} to Ti₅. All the alloys exhibit an obvious endothermic peak at a high temperature around 1000 K. This peak was formed after the glass transition and crystallisation event, and before the endothermic melting process. The T_f and T_L are indicated by arrows on the curves and the detailed T_f and T_L values and calculated K values are all shown in Table 5.2. As the content of Ti increases from 0.5 at. % to 5 at. %, the eutectoid transformation shifts to higher temperatures, and the T_f values gradually increase from 1027 K to 1053 K with increasing Ti content. In contrast, the T_L values decrease from 1198 K to 1153 K with increasing Ti content. The K values can be then obtained, which are between 0.869 and 0.913. Compared with the literature [162], these values indicate the alloys can be fabricated to relatively large sizes and the B2-CuZr phase formation become easier.

The above results have illustrated that with an increase in Ti content, T_f gradually increases. Therefore, the B2-CuZr phase thermal stability is reduced with increasing Ti content. The substitution of Zr by Ti has significantly increased the B2-CuZr phase transformation temperature, thus destabilising the B2-CuZr phase. The single B2-CuZr phase structure would be easier to retain for lower Ti contents. It is known that B2-CuZr phase will be stable at a high melting temperature above 988 K and should decompose eutectoid into the stable $\text{Cu}_{10}\text{Zr}_7$ and CuZr_2 at a lower temperature. As the Ti content increases, the B2-CuZr phase will become easier to decompose at lower temperatures, which is why the $\text{Cu}_{10}\text{Zr}_7$ was detected for the high Ti content samples. Due to the reduced thermal stability of B2-CuZr phase, the amorphous phase is prone to form during the casting process. The volume fraction of B2-CuZr phase would decrease with increasing Ti content and the amorphous phase will be enhanced, which corresponds well with the XRD results and also the ternary Cu-Zr-Ti BMGMCs [130].

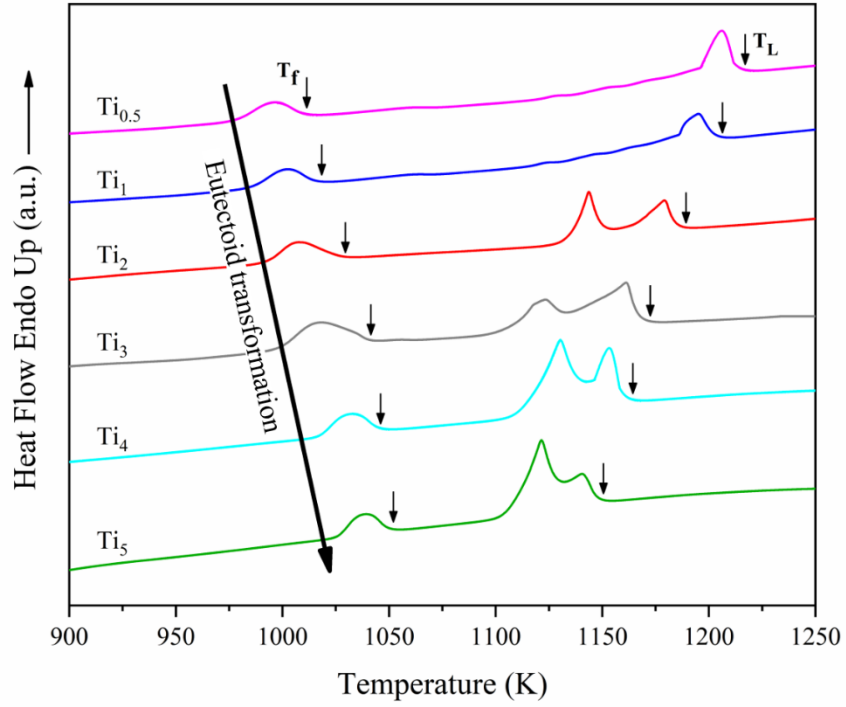


Figure 5.6: DTA trace of as-cast $Zr_{50-x}Cu_{44}Al_5Ag_1Ti_x$ ($x=1, 2, 3, 4$ and 5 at %) specimens.

Table 5. 2: Thermodynamic properties of $Zr_{50-x}Cu_{44}Al_5Ag_1Ti_x$ ($x=0.5, 1, 2, 3, 4$ and 5 at %) alloys as-cast rods obtained from DSC and DTA.

| x | T_g (K) | T_x (K) | ΔT_x (K) | T_f (K) | T_L (K) | T_{fg} (K) | K |
|-----|-----------|-----------|------------------|-----------|-----------|--------------|-------|
| 0.5 | 673 | 740 | 67 | 1027 | 1198 | 0.56 | 0.856 |
| 1 | 676 | 739 | 63 | 1030 | 1192 | 0.57 | 0.864 |
| 2 | 680 | 747 | 67 | 1033 | 1185 | 0.57 | 0.872 |
| 3 | 683 | 742 | 59 | 1038 | 1178 | 0.58 | 0.881 |
| 4 | 687 | 748 | 61 | 1043 | 1175 | 0.58 | 0.888 |
| 5 | 680 | 738 | 58 | 1053 | 1153 | 0.58 | 0.913 |

5.3.3 Mechanical Properties

As shown in Figure 5.7, the true compressive stress-strain curves of 6 mm Ti_{0.5}, Ti₁, Ti₂, Ti₃, Ti₄ and Ti₅ are obtained. These specimens exhibit different yielding behaviours and plasticity with the different microstructure natures.

The Ti_{0.5} exhibits a yield strength of 1490 MPa, high plastic strain of 12.3 % and fracture strength of 1720 MPa. Obvious plastic strain can be observed in this specimen even with the formation of some B19' martensitic phase. For the Ti₁ specimen, the yield strength is 1453 MPa and fracture strength is 1680 MPa with a plastic strain of 9.1 %. The increase in stress with strain phenomenon is caused by work-hardening behaviour which cause by the TRIP effect. For the Ti₂ and Ti₃ alloys, the yield strengths are 1692 MPa and 1130 MPa respectively, and the fracture strengths are 1723 MPa and 1233 MPa with plasticity 1.7 % and 1.3 % respectively. The low yield strength for the Ti₃ alloys is caused by the formation of brittle Cu₁₀Zr₇ crystalline phases. However, even though the B2-CuZr phase was obtained for these two specimens, the specimens still exhibit low yield strengths. The Ti₄ and Ti₅ exhibit typical BMG compression curve, they exhibit fracture strength of 1687 MPa and 1493 MPa respectively. They have very small plasticity which are all less than 1 %. The amorphous phase combined with small amount of brittle phases structure of these two alloys contributes to a high fracture strength but no obvious plasticity and work-hardening behaviour.

The compression tests results demonstrate that 6 mm Ti_1 specimens exhibit good mechanical properties due to the formation of single B2-CuZr phases. The specimens with brittle phases have shown relatively low yield strength and lack of plasticity even with the formation of the B2-CuZr phase. The work-hardening behaviour is believed to be caused by the TRIP effect. Detailed microstructure studies are given in the following sections.

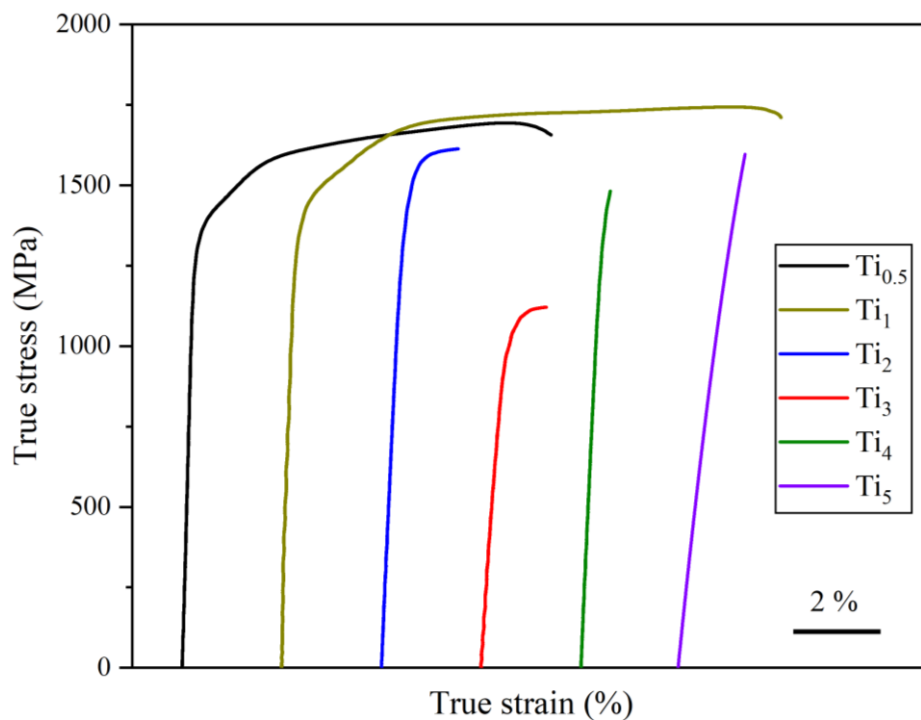


Figure 5.7: True stress-strain compression curve of the 6 mm $Zr_{50-x}Cu_{44}Al_5Ag_1Ti_x$ ($x=0.5, 1, 2, 3, 4$ and 5 at %) alloys.

The fracture surfaces of all the 6 mm samples were examined using SEM. The fracture surface of the $Ti_{0.5}$ and Ti_1 sample is shown in Figure 5.8 (a) and (b) respectively. Vein-like, fishbone-like patterns are observed, the different sized shear bands interact with each other. Meanwhile, small amounts of granulated structures were also observed. The granulated

structure is mainly caused by the formation of the crystalline phases of the samples. The fracture surface of the Ti₂ and Ti₃ samples are shown in Figure 5.8 (c) and (d) respectively. The amount of granulated structures is obvious increased and embedded with the vein-like pattern. This is due to the increase of crystalline phase volume fraction, the brittle phases and B2-CuZr phase are co-existing in these two samples which lead to the morphology of the samples. Figure 5.8 (e) and (f) are the fracture surfaces of the Ti₄ and Ti₅ samples respectively. The vein-like shear bands dominate the fracture surface, the shear bands sizes vary between 40-50 μm and no secondary shear bands were observed. This morphology contributes to a relatively high yield or fracture strength but lack of plasticity. The shear bands will propagate very quickly during the deformation and lead to the fracture of the sample. The fracture microstructures of the samples correspond well with the compression test results. The compression tests results have demonstrated that the formation of brittle crystalline phases will strongly affect the mechanical properties of this alloy system. The single B2-CuZr phase structure is more desired for the TRIP reinforced BMGMCs which is consistent with the previous chapter's results and the literature.

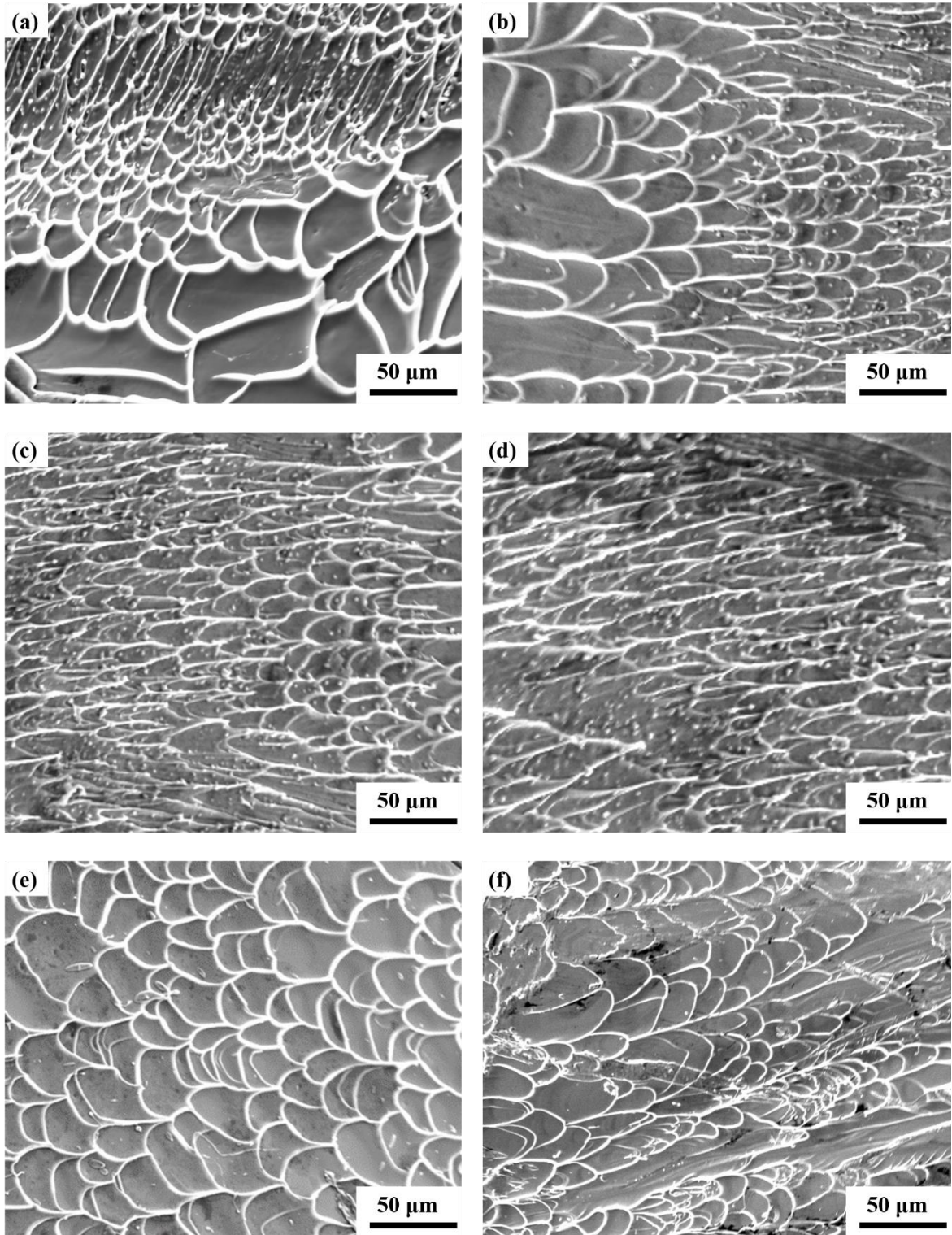


Figure 5.8: (a)-(f) SEM images of fracture surfaces for all the 6 mm specimens from $Ti_{0.5}$ to Ti_5 .

The longitudinal surfaces of the 6 mm $Ti_{0.5}$ and Ti_1 samples were also examined by SEM as shown in Figure 5.9 (a) and (b). Both samples exhibited high-density shear bands due to the large plasticity. The samples exhibit large number of primary shear bands which interact with the small secondary shear bands, shear bands were accumulated together and form a squama-like pattern which strongly enhanced the plasticity of the materials. The shear bands hindered further fracture propagation with multiple shear bands from different directions. These shear bands stacked together and increased the internal energy in the shear bands which led to the high plasticity during the compression

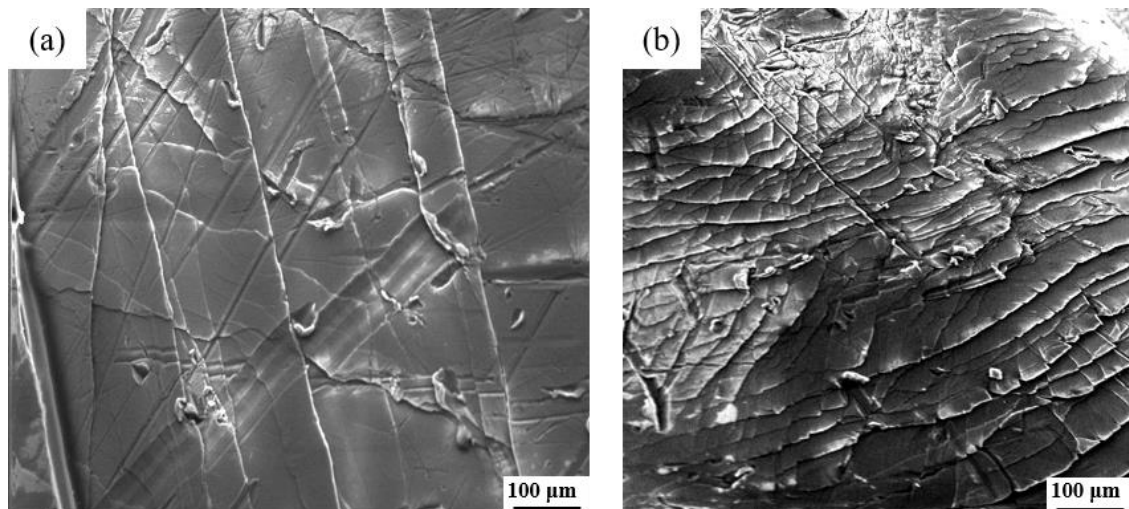


Figure 5.9: SEM images of the longitudinal surface of the deformed 6 mm (a) $Ti_{0.5}$ (b) Ti_1 specimens. Large shear bands aggregations are observed.

In order to further examine the reason for the enhanced mechanical properties of the specimens. The detailed microstructure features of deformed 6 mm Ti_1 sample was investigated by TEM and HRTEM. Figure 5.10 (a) shows a BF-TEM image and the corresponding SAED patterns, which indicates the formation B19' martensitic phase narjed

by yellow circle. The XRD results and TEM images of the as-cast 6 mm Ti₁ sample shown in the previous section indicate that no B19' formation in the as-cast alloy. These results have proved the transformation from the B2-CuZr phase structure to the B19' martensitic structure during the deformation. The B2-CuZr SAED pattern was also obtained from the image. This phenomenon has further verified the occurrence of the TRIP effect, which can be observed for this alloy and it has contributed to the enhanced mechanical properties. These results have proved the formation of martensitic phase after the deformation process which is also embedded in the glassy matrix. The B2-CuZr and B19' phases coexist after the deformation and not all the B2-CuZr phases have experienced the TRIP process. Figure 5.10 (b) shows the HRTEM image of the B19' phase in the (a). Figures 5.11 (a) and (b) show the nanocrystals after the deformation process, the image clearly indicates that the density of the nanocrystals has obviously increased compared with the as-cast sample, and some of them have grown to the size of 30-50 nm. The amorphous phase can still be observed and the nanocrystals are embedded in the amorphous matrix. The twinning-like features are also obtained from the image which are indicated by the yellow arrows. These features are indicative of twinning formation and will be further investigated in the future. As demonstrated before, the TRIP effect is usually accompanied by the formation of twinning. These microstructures will strongly enhance the work-hardening behaviour of the alloy.

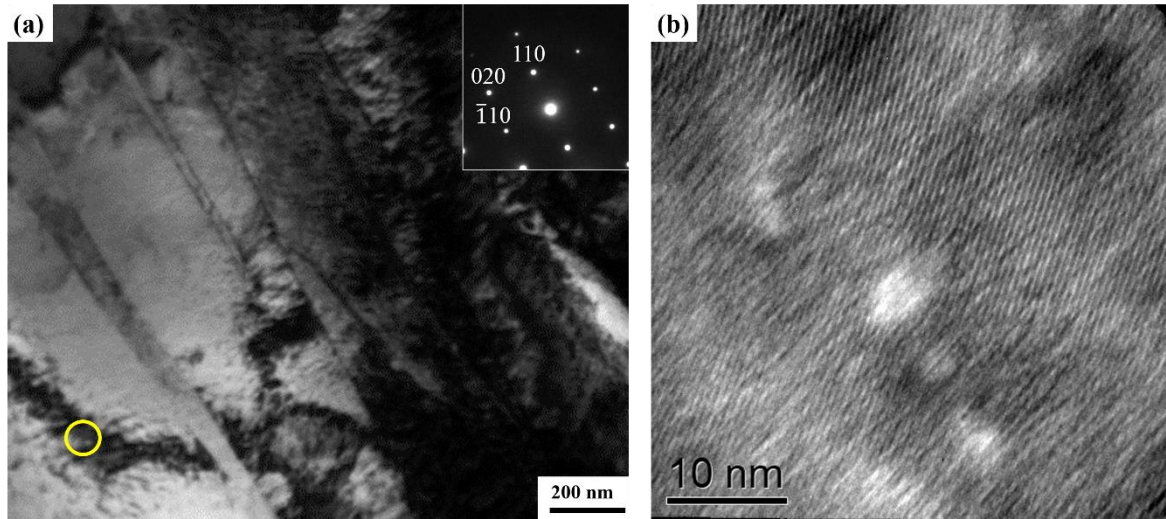


Figure 5.10: (a) Bright-field TEM images of the deformed 6 mm Ti₁ samples after the compression tests. (b) The HRTEM image of the B19' martensitic phase.

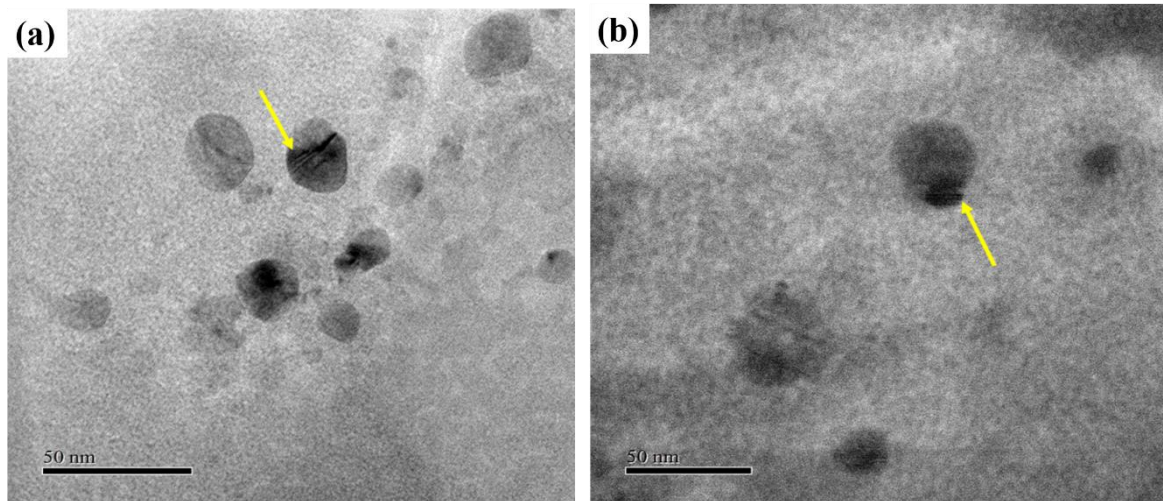


Figure 5.11: (a) and (b) The nano-sized B2-CuZr crystalline phase is an indicative of twinning feature.

The whole deformation process can be explained as follows: When the loading is applied to the alloy, local stress concentrations will occur. The B2 phase will precipitate after a period and reduce the stress concentrations. The shear transformation zones (STZs) will also

form and develop, but the propagation of the shear bands can be hindered by the B2 nanocrystals. The twinning of B2 crystals forms and further absorbs the stresses from the matrix. The whole process significantly delays the fracture of the alloy and increases the ductility of the alloy system. The combination of the B2 phase and glassy matrix lead to the heterogeneities of the microstructure. This structure will strongly affect the propagation of the shear bands so the shear band will move in a wave-like shape and no big shear bands can be formed. The local stress-strain difference will cause shear band movement to become more difficult. The shear bands gather together and lead to an increase in surface area and the energy between shear bands is reduced. By confirming the martensitic transformation in the current alloy systems and comparing with the previous studies of ZrCu-based BMGMCs, one of the common phenomena is the ‘blocking effect’ of the B2 phase. The shear band movement is hindered or delayed by the B2 crystals, which strongly enhances the plasticity of the materials. Some of the research also indicated that a combination of micro- and nano-sized B2 phases was obtained after compression and tensile tests. The martensitic transformation will prevent early necking under the tensile condition. The results for both 3 mm and 6 mm samples show good compressive plasticity and work-hardening behaviour. The 3 mm tensile properties are also improved.

According to previous research, the B2 phase has very similar elastic properties to a glassy matrix [122], [134] so there will be no local stress distribution between the glassy matrix and crystalline phase. It is also known that the hardness of the crystalline phase is

smaller than the amorphous matrix, so it is easier to deform under external force. The deformed amorphous matrix will experience a softening process due to the formation of shear bands. However, the metastable B2-CuZr phase transformation will lead to an increase in hardness through the phase transformation to the B19' martensitic phase. During the deformation process the shear band movement will also be stopped by the B2 crystals; the ductile crystals will strongly affect any further movement of the shear bands. In addition, some of the B2 phases will undergo a martensitic transformation during the deformation process, which will cause the work hardening behaviour and prevent large shear band movement.

The 3 mm and 6 mm samples were tested by the tensile tests. Due to the time limits and machining difficulties, only the Ti₁ samples were fabricated to the tensile test samples. The other samples will be examined in the future. The stress-strain curve after the tensile test is shown in Figure 5. 12. The yield strength of 3 mm sample is 1878 MPa and the fracture strength is 1901 MPa with the plastic strain of 1.8 %. The nanocrystals in the 3 mm sample have not contributed to significant plasticity during tensile. For the 6 mm sample the work-hardening behaviour was obtained, it shows a yield strength of 1321 MPa and fracture strength of 1563 MPa with a plastic strain of 2.3%.

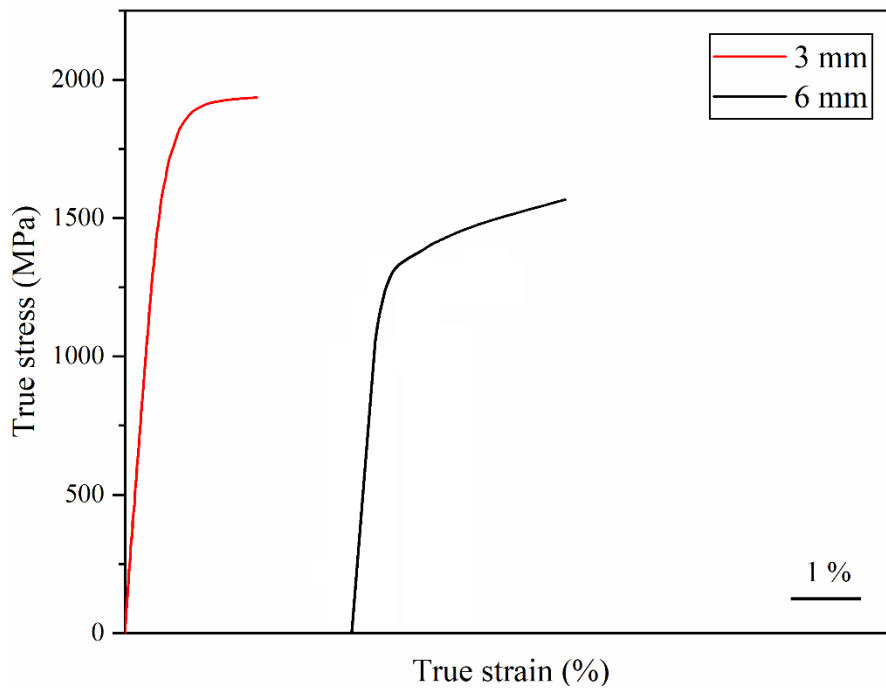


Figure 5.12: Tensile test stress-strain curve of the 3 mm and 6 mm Ti₁ sample.

The SEM images of fracture surfaces after the tensile test are shown in Figure 5. 13. Figure 5. 13 (a) shows many dimple structures combined with a small number of shear bands. The dimple structure is a ductile metallic alloys feature which proves that the formation of B2-CuZr phase has led to the enhanced mechanical properties. The fishbone-like patterns formed along with the dimple structures are shown in Figure 5.13 (b). Figure 5.13 (c) shows the B2-CuZr phase after the tensile test. The equiaxed crystalline structure has been stretched to an elliptical shape but these crystals have hindered the propagation of the large shear bands and the ‘block effect’ can be clearly observed. Figure 5. 13 (d) shows the edged of the fracture surface with granulated structures. The reason for the enhanced tensile results of the 6 mm Ti₁ sample is believed due to the TRIP effect. The B2 phase can stabilise the tensile plastic deformation by boosting the interaction of shear bands.

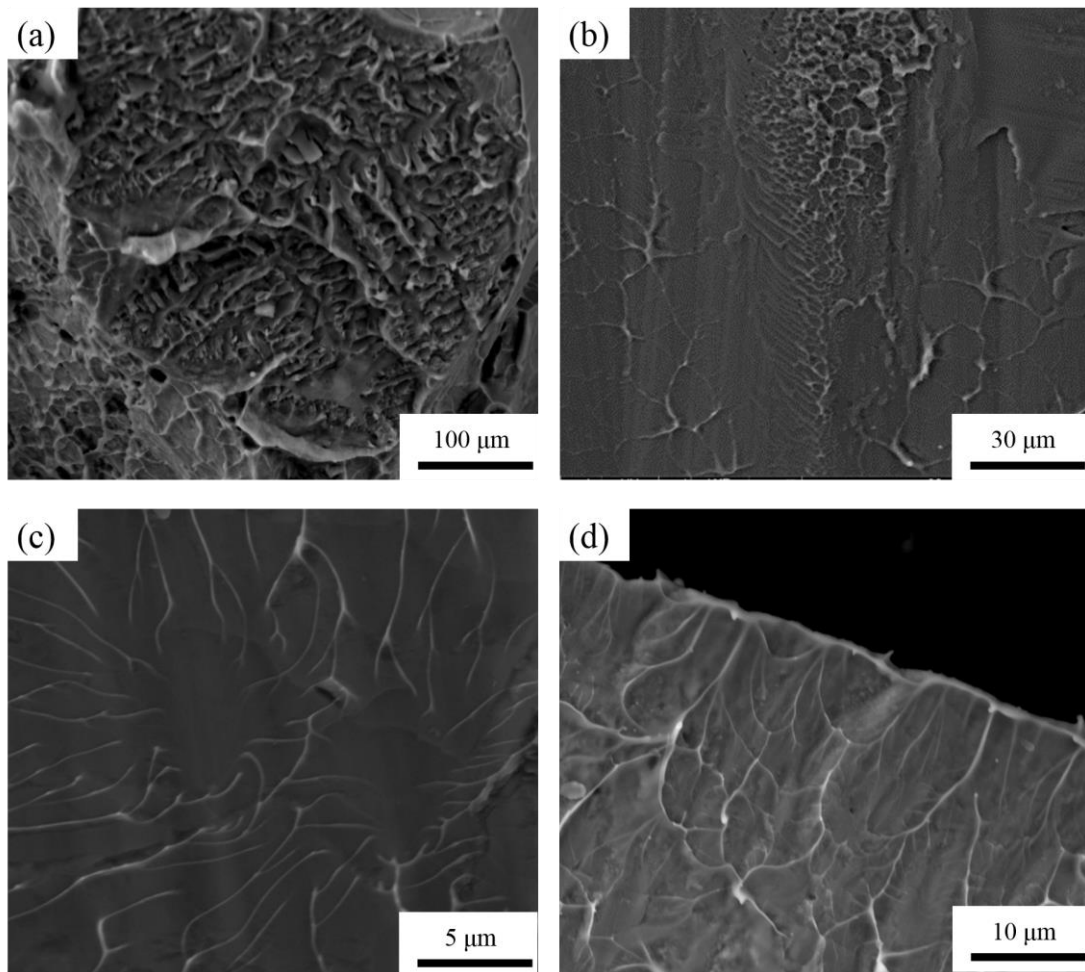


Figure 5.13: (a)–(b) SEM images of 6 mm Ti₁ sample fracture surface after the tensile tests. (c)–(d)

The ‘block effect’ due to the B2-CuZr phase is observed. The alloy presents ductile features after the tensile tests.

5.4 Conclusions

In this chapter, a new series of Zr-Cu-Al-Ag-Ti TRIP reinforced BMGMCs were designed and investigated based on the Zr-Cu-Al-Ag alloy system. The effects of Ti content on the GFAs and mechanical properties of the alloy systems have been studied. The addition of Ti content has enhanced the GFAs of the alloy system and samples with a microstructure which consists of the amorphous phase combined with the single B2-CuZr phase were obtained.

This type of BMGMC exhibits good GFA with an as-cast rod up to at least 6 mm in diameter. The martensitic transformation from the metastable B2-CuZr phase to monolithic B19' phase was observed after the compression tests. The deformation-induced martensitic transformation process leads to significantly improved compressive plasticity, with plastic strain of 9.1 %, and work hardening behaviour.

The $Zr_{49}Cu_{45}Al_4Ag_1Ti_1$ specimen can be cast to a rod sample up to at least 6 mm with a amorphous plus B2-CuZr phase structure. Improved GFAs and mechanical properties can be obtained for this sample. It has the potential to be fabricated to a larger size by modifying the compositions and has the potential to be applied to real-life applications.

Chapter 6

The Effect of minor Nb Addition on the Glass-Forming Ability and Mechanical Properties of Zr-Cu-Al-Nb Bulk Metallic Glasses

6.1 Introduction

BMGs exhibit unique properties such as high strength, high elastic strain limit and high hardness due to the absence of long-range ordered structure [2] [3][135] [136]. Defects such as dislocations and stacking faults cannot be generated in this structure. These characteristics contribute to the enhanced mechanical properties of BMGs [137]. However, room-temperature brittleness and lack of plasticity are still the main drawbacks of BMGs [126][138]. Developing BMG alloys with enhanced plasticity and good GFAs are desirable for researchers.

It is widely accepted that, for alloys with large atomic size, mismatched negative enthalpy of mixing among the constituent elements will enhance the GFA and improve the mechanical properties [43]. The atomic packing efficiency is enhanced due to these effects. However, recent researches have indicated that the minor addition of the elements that have positive heat of mixing with the constituent elements can also improve the GFAs and mechanical properties of BMGs [139]–[143]. From the literature, Zr-Cu-Al alloys with the addition of various Ag contents can be cast to sample sizes up to 25 mm in diameter [67].

The Fe element was introduced to the Zr-Cu-Al system and strongly enhanced the GFA of the system [144]. The effect of positive heat of mixing of elements has strongly attracted attention. In addition, as demonstrated in Chapter 4, minor Ag addition has significantly enhanced the GFA of the base Zr-Cu-Al alloy.

Among the various BMGs, ZrCu-based BMGs are considered to have potential in structural applications due to their good GFAs and mechanical properties [145]. Recently the Zr-Cu-Al-Nb alloy systems have been reported by some groups, exhibiting good work-hardening, improved GFAs and plasticity. Phase separation was observed in the Zr-Cu-Ni-Al-Nb and Zr-Cu-Al-Nb systems as reported by Chen et al [146][98]. The plasticity was strongly enhanced due to this BMG ‘composite-like’ effect. Another investigation by Wang et al. also indicated the occurrence of the phase separation phenomenon. Deformation-induced nano-crystallisations were also observed in this system [147]. However, the effect of minor addition of Nb on thermal stability, and mechanical properties of ZrCu-based BMGs are rarely studied. Therefore, understanding the GFAs, thermal stability and the mechanical properties of the BMGs are very important. The influence of the alloying element on the mechanical properties should also be studied. As a result, a series of $Zr_{50}Cu_{45-x}Al_5Nb_x$ ($x = 0.2, 0.4, 0.6, \text{ and } 0.8$ at. %) systems were developed and investigated based on the $Zr_{50}Cu_{45}Al_5$ alloy which was introduced in chapter 4. The investigation into the effect of Nb addition on the ZrCu-based BMGs is discussed in this chapter. The alloys are named as $Nb_{0.2}$, $Nb_{0.4}$, $Nb_{0.6}$ and $Nb_{0.8}$ for convenience.

6.2 Experimental Work

The constituent elements of $Zr_{50}Cu_{45-x}Al_5Nb_x$ ($x = 0.2, 0.4, 0.6$ and 0.8 at. %) alloys with purity > 99.9 % were prepared under an argon atmosphere using arc melting. The alloy ingots were melted four times to ensure compositional homogeneity. The weight loss for the alloys after melting were less than 0.1 wt. %. The ingots were then fabricated into rod shapes with $2-4$ mm diameters by using copper mould suction casting.

The microstructure nature of the as-cast samples was investigated using the Siemens D5000 XRD with the monochromatic radiation source Cu Ka, and the diffraction angle (2θ) was set between 20° and 80° . Thermal properties and annealing processes were examined and performed using the Perkin-Elmer diamond DSC and Perkin-Elmer DTA under an argon atmosphere with different heating rates. Room temperature compression and tensile tests were performed using a Zwick-Roell machine with initial strain rates of $2 \times 10^{-4} s^{-1}$ and $1 \times 10^{-4} s^{-1}$ respectively. A camera was applied to calibrate and measure the strain during the tensile tests. The compression test specimens were cut from the as-cast rods with an aspect ratio (length : width) of $2:1$, and both the top and bottom ends of the as-cast rods were carefully polished to ensure parallelism. Cross-section surfaces following the mechanical tests were examined using the FEI Inspect F SEM. Detailed microstructure information and amorphous features were examined using the FEI Tecnai TEM and JEOL 2010 HRTEM. The specimens for the TEM were ground and polished to $20 \mu m$ before the Ion milling process was applied.

6.3 Results and Discussions

6.3.1 Microstructure features of as-cast samples

Figure 6.1 displays the XRD patterns of as-cast $Zr_{50}Cu_{45-x}Al_5Nb_x$ ($x = 0.2, 0.4, 0.6$ and 0.8 at. %) rod specimens. As shown in Figure 6.1, the critical diameter of $Nb_{0.2}$ is 2 mm, whereas the $Nb_{0.4}$ and $Nb_{0.6}$ show the same critical diameter of 3 mm, $Nb_{0.8}$ exhibit the critical diameter of 4 mm. All the 2 mm specimens show a broad halo hump around $2\theta = 38^\circ$, which indicates the formation of the amorphous feature of the alloys. Clear crystalline peaks are obtained for the 3 mm $Nb_{0.2}$ sample and the 4 mm $Nb_{0.6}$ samples. The peaks are indexed as B2-CuZr and Al_2Zr . Comparing with the result in chapter 4, the critical diameter of $Zr_{50}Cu_{45}Al_5$ has been enhanced due to the minor addition of Nb contents.

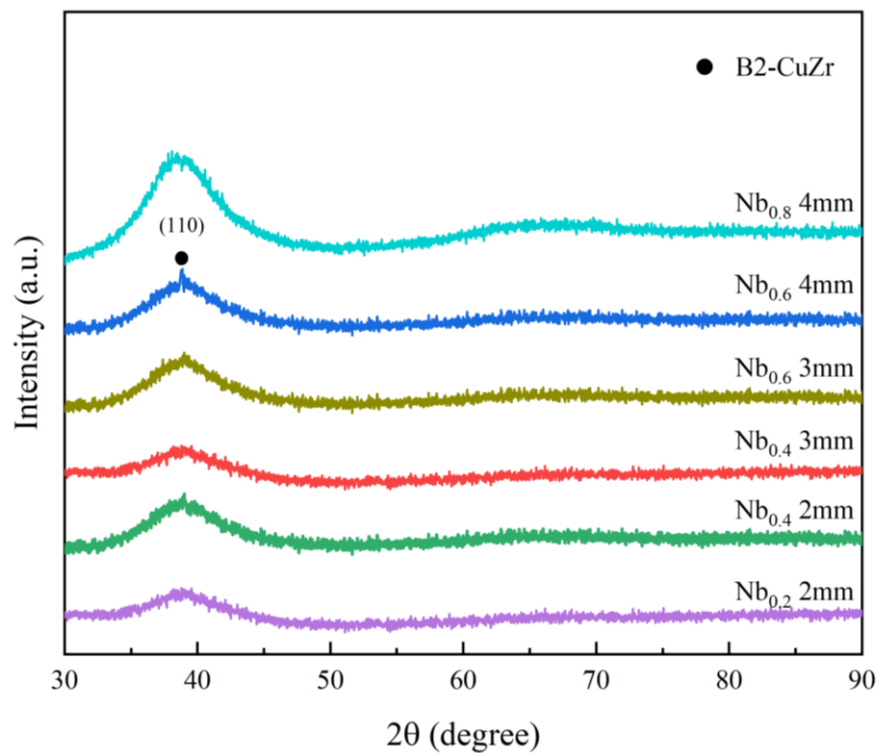
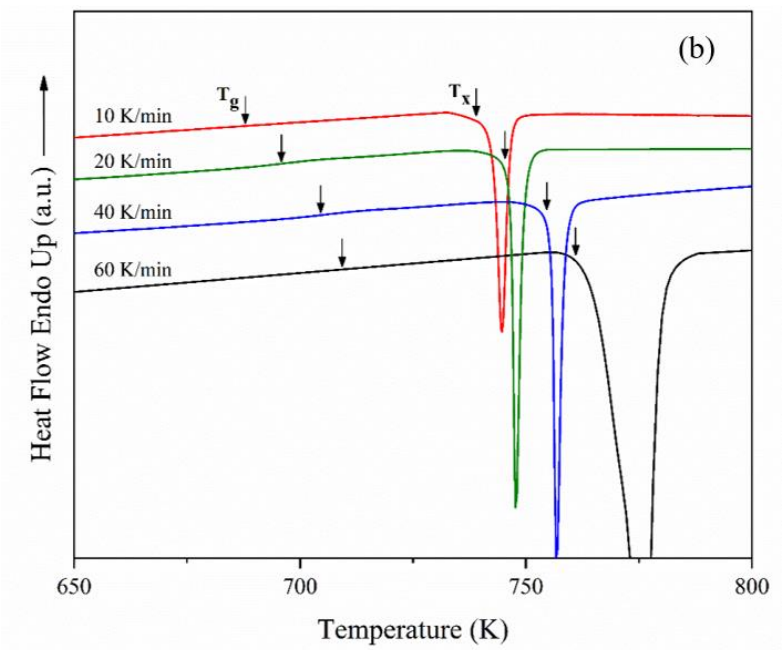
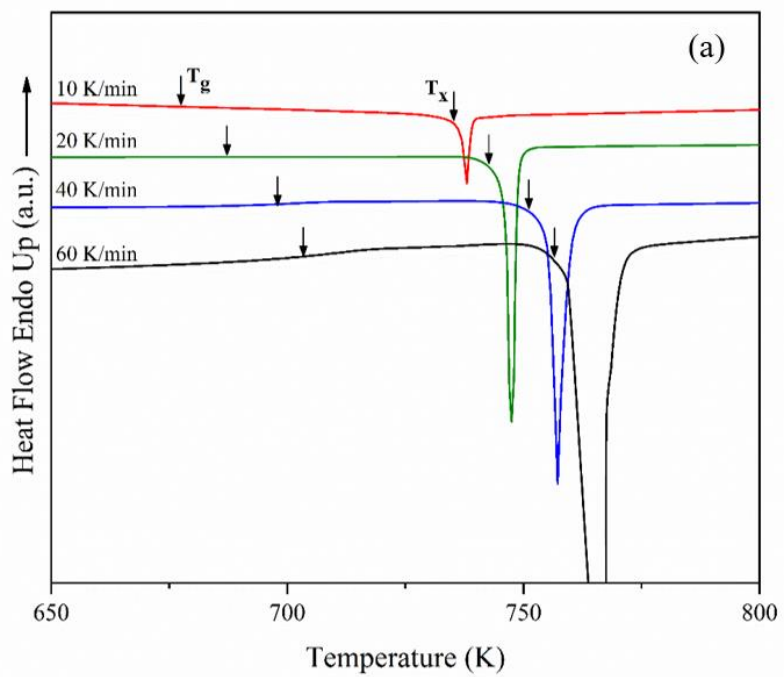


Figure 6. 1: XRD patterns of the as-cast $Zr_{50}Cu_{45-x}Al_5Nb_x$ ($x = 0.2, 0.4, 0.6$ and 0.8 at. %) alloys.

6.3.2 Glass forming ability and thermal stability of as-cast samples

Understanding the glass transition and crystallisation process is very important to determine the thermal stability of BMGs. In general, the glass transition and crystallisation kinetics are studied using thermal annealing techniques. The non-isothermal tests are performed using DSC. Figure 6.2 (a)-(d) shows the DSC curves of the as-cast 2 mm diameter $Zr_{50}Cu_{45-x}Al_5Nb_x$ ($x = 0.2, 0.4, 0.6$ and 0.8 at. %) alloys at different heating rates of 10, 20, 40 and 60 K/min respectively. The values of T_g , T_x and ΔT_x can be obtained from the DSC curves. Detailed DSC results are shown in Table 6.1-6.3. The DTA tests were also applied to all the 2 mm samples and the DTA curves are shown in Figure 6.3. The T_l values are also obtained from the curves. In addition, γ ($= T_x/(T_g+T_l)$) and T_{rg} ($=T_g/T_l$) are simple and reliable parameters which can also indicate the GFA of the alloys. All the parameters obtained from the DSC and DTA curves are summarised in Table 6. 1.



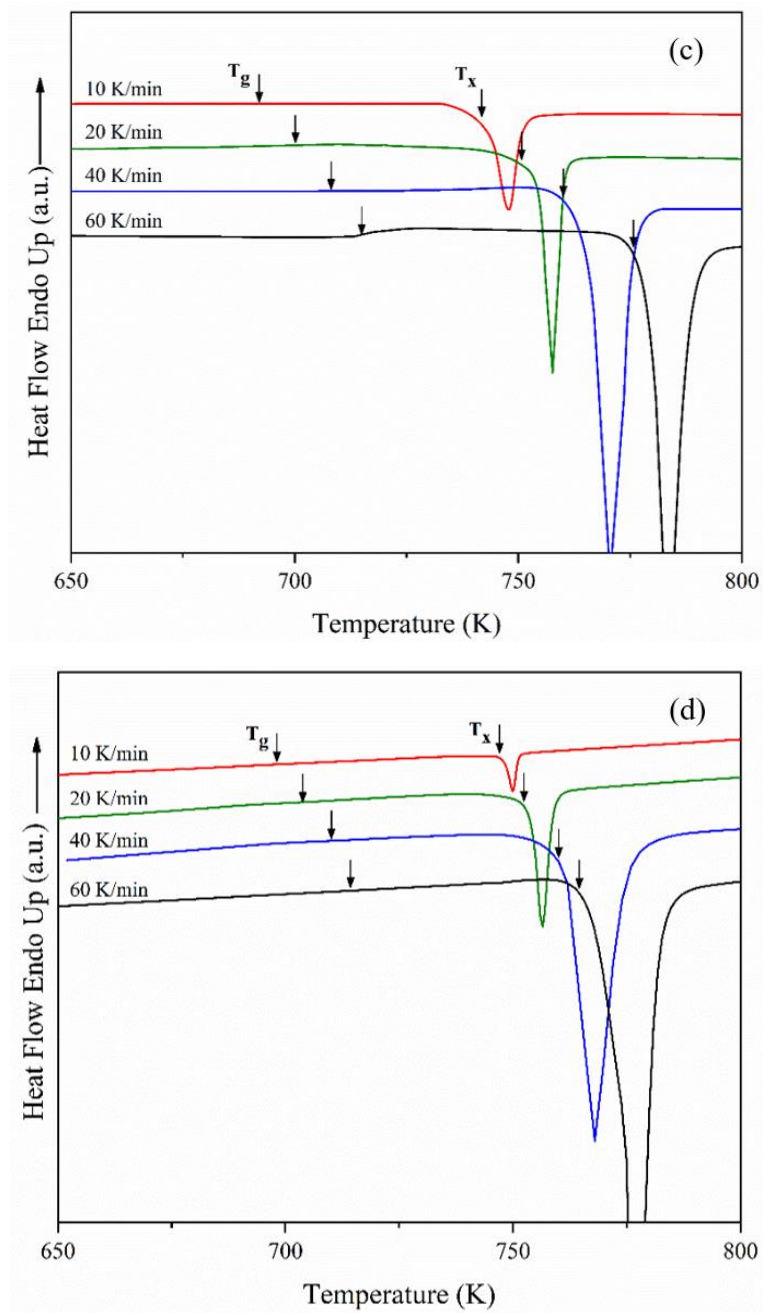


Figure 6. 2: DSC curves of the as-cast 2 mm $\text{Zr}_{50}\text{Cu}_{45-x}\text{Al}_5\text{Nb}_x$ ($x = 0.2, 0.4, 0.6$ and 0.8 at. %) BMG samples, (a) $\text{Nb}_{0.2}$, (b) $\text{Nb}_{0.4}$ (c) $\text{Nb}_{0.6}$ and (d) $\text{Nb}_{0.8}$ at heating rates of 10 K/min, 20 K/min, 40 K/min and 60 K/min respectively.

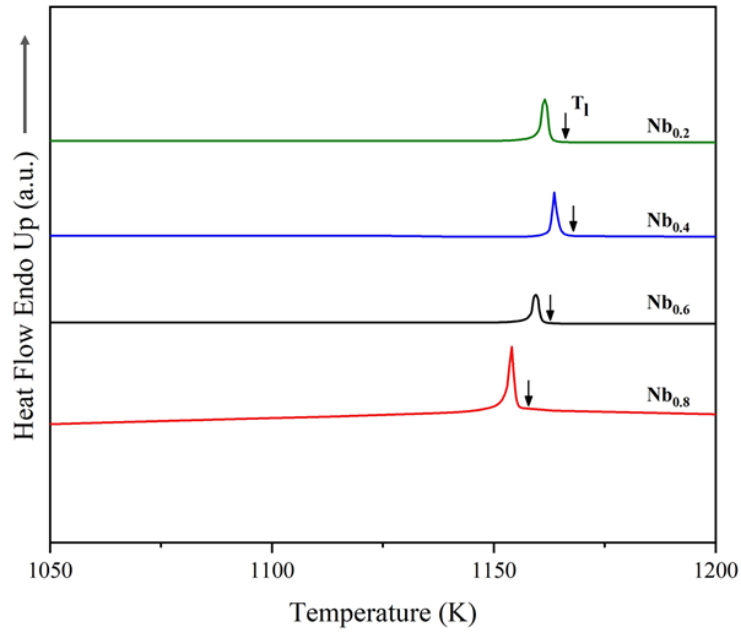


Figure 6. 3: DTA curves of the as-cast 2 mm $Zr_{50}Cu_{45-x}Al_5Nb_x$ ($x = 0.2, 0.4, 0.6$ and 0.8 at. %) BMG samples. The T_1 values are obtained from the curve.

All the alloys exhibit a clear endothermic event which corresponds to the glass transition process. The exothermic peaks are observed at higher temperatures, which indicate the crystallisation process of the alloys. According to the DSC traces, both glass transition and crystallisation events have shifted to a higher temperature with an increase in Nb content. According to Inoue's theory [2], the width of the supercooled liquid region is indicated by ΔT_x , which can be used to evaluate the stability of the amorphous phase and estimate the GFA of the alloys. The supercooled liquid regions ΔT_x at a 20 K/min heating rate of the four samples are 55 K, 49 K, 50 K and 48 K respectively. The $Nb_{0.2}$ specimen exhibits the largest ΔT_x value but the critical diameter of this alloy is the smallest among these four compositions. The T_{rg} values for the four alloy compositions are 0.590, 0.597, 0.601 and 0.609 respectively.

The γ values for the four alloy compositions are 0.401, 0.400, 0.403 and 0.404 respectively. As demonstrated in the literature, alloys which display good GFAs usually have T_{rg} higher than 0.5 or γ values higher than 0.35. All the four compositions exhibit higher T_{rg} and γ values, however the Nb_{0.2} alloy exhibited a lower GFA with critical diameter 2 mm even with the high ΔT_x , T_{rg} and γ values. According to the above results, the Nb_{0.8} exhibited the best GFA among these four compositions.

Table 6. 1: T_g , T_x , T_l , T_x , T_{rg} and γ values of the $Zr_{50}Cu_{45-x}Al_5Nb_x$ ($x = 0.2, 0.4, 0.6$ and 0.8 at. %)

BMG samples at a heating rate of 20 K/min

| | T_g /K | T_x /K | T_l /K | ΔT_x /K | T_{rg} | γ |
|-------------------------|----------|----------|----------|-----------------|----------|----------|
| Nb_{0.2} | 687 | 742 | 1165 | 55 | 0.590 | 0.401 |
| Nb_{0.4} | 697 | 746 | 1167 | 49 | 0.597 | 0.400 |
| Nb_{0.6} | 700 | 750 | 1163 | 50 | 0.601 | 0.403 |
| Nb_{0.8} | 705 | 753 | 1158 | 48 | 0.609 | 0.404 |

Table 6. 2: The T_g values of the as-cast 2 mm $Zr_{50}Cu_{45-x}Al_5Nb_x$ ($x = 0.2, 0.4, 0.6$ and 0.8 at. %)

BMG samples at heating rates of 10 K/min, 20 K/min, 40 K/min and 60 K/min.

| | 10 K/min | 20 K/min | 40 K/min | 60 K/min |
|-------------------------|----------|----------|----------|----------|
| Nb_{0.2} | 677 | 687 | 698 | 704 |
| Nb_{0.4} | 688 | 697 | 706 | 710 |
| Nb_{0.6} | 692 | 700 | 709 | 712 |
| Nb_{0.8} | 698 | 705 | 711 | 715 |

Table 6. 3: The T_x values of the as-cast 2 mm $Zr_{50}Cu_{45-x}Al_5Nb_x$ ($x = 0.2, 0.4, 0.6$ and 0.8 at. %)

BMG samples at heating rates of 10 K/min, 20 K/min, 40 K/min and 60 K/min.

| | 10 K/min | 20 K/min | 40 K/min | 60 K/min |
|-------------------------|----------|----------|----------|----------|
| Nb_{0.2} | 735 | 742 | 751 | 756 |
| Nb_{0.4} | 738 | 746 | 755 | 759 |
| Nb_{0.6} | 743 | 750 | 758 | 763 |
| Nb_{0.8} | 747 | 753 | 760 | 764 |

For the general BMG alloy systems, the transformation temperatures will become higher at faster heating rates [2]. The T_g and T_x values with different heating rates (β) were measured according to this concept. The activation energy for the glass transition (E_g) and crystallisation (E_x) of the BMG system are determined. There are two well-known methods which can be used to determine the activation energy for glass transition and crystallisation processes of the alloy systems, known as the Kissinger and the Ozawa methods [2]. The Kissinger model is a widely accepted model to assess reactions that are thermally activated in solid-state materials, and it can also be applied to study the crystallisation process[148]–[152]. As shown in Equation 6.1, E is the activation energy for reactions such as glass transition and crystallisation. T is the characteristic temperature, β is the heating rate, R is the gas constant and C is a constant. The E/R value is the slope of the line $\ln(T^2/\beta)$ vs $1000/T$, hence by plotting this line the value of E_g and E_x can be obtained.

$$\ln\left(\frac{T^2}{\beta}\right) = \frac{E}{RT} + c \quad (6.1)$$

The Kissinger plot of E_g and E_x of the four compositions are shown in Figure 6.4 (a) and (b), the activation energy can be then calculated for these four compositions. The E_g values for these Nb_{0.2} to Nb_{0.8} alloys are 256 kJ/mol, 309 kJ/mol, 337 kJ/mol, and 422 kJ/mol respectively. The E_x values for these four alloy compositions are 364 kJ/mol, 373 kJ/mol, 384 kJ/mol and 482 kJ/mol.

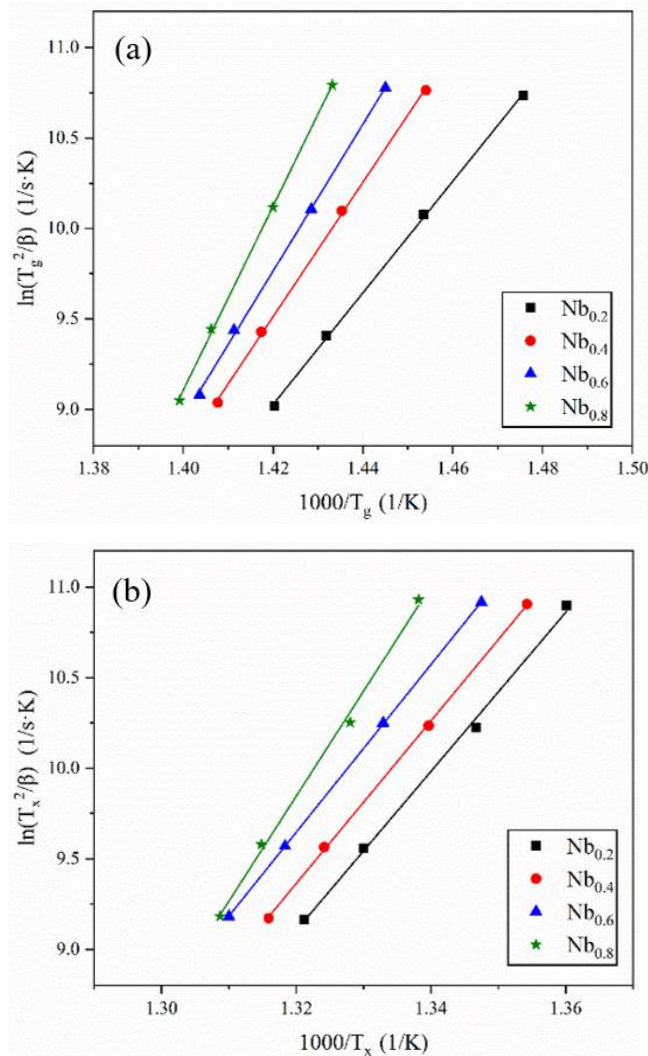
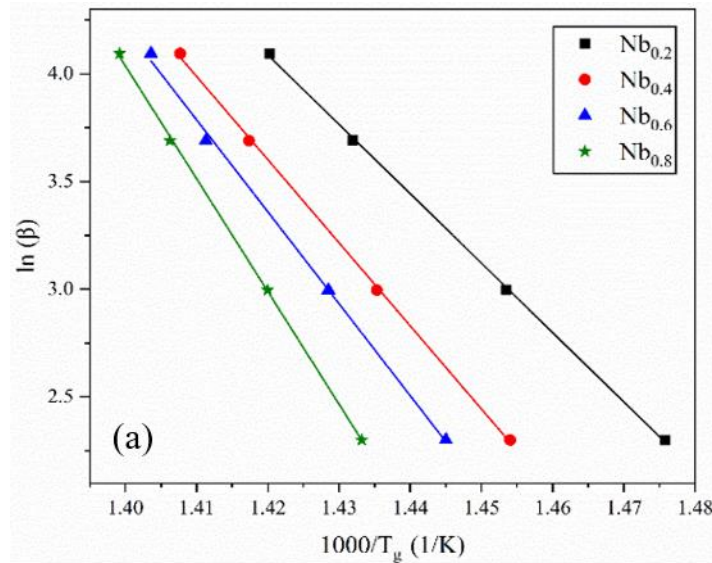


Figure 6. 4: The Kissinger plots of Zr₅₀Cu_{45-x}Al₅Nb_x (x = 0.2, 0.4, 0.6 and 0.8 at. %) BMG samples at temperature (a) T_g (b) T_x .

Another approach to determine the activation energy of the BMGs is using the Flynn-Wall-Ozawa plot [2]. The activation energy can be determined by plotting the $\ln(T/\beta)$ vs $1/T$, and the gradient is the activation energy. The E_g and E_x values are also calculated by using the Ozawa method as shown in Figure 6.5 (a) and (b).

$$\ln(\beta) = \frac{E_x}{RT_x} + c \quad (6.2)$$

The E_g values for the Nb_{0.2} to Nb_{0.8} alloys are 267 kJ/mol, 321 kJ/mol, 355 kJ/mol, and 435 kJ/mol respectively. The E_x values for these four alloy compositions are 377 kJ/mol, 386 kJ/mol, 397 kJ/mol and 495 kJ/mol respectively.



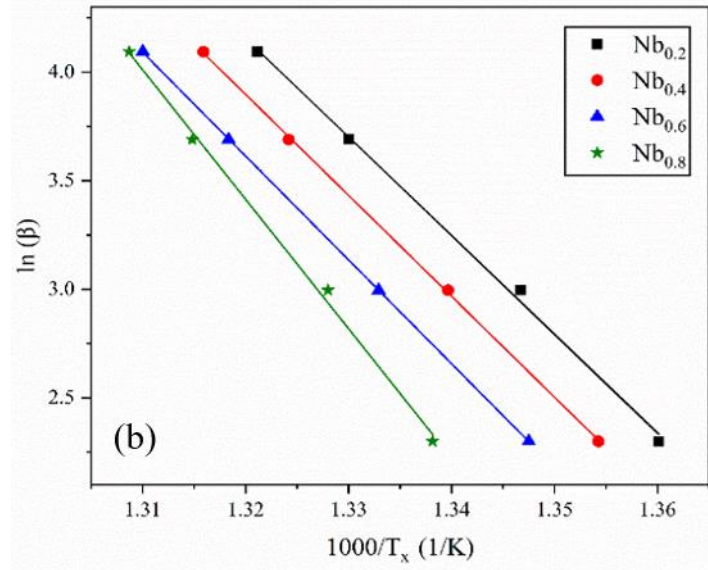


Figure 6. 5: The Ozawa plots of $Zr_{50}Cu_{45-x}Al_5Nb_x$ ($x = 0.2, 0.4, 0.6$ and 0.8 at. %) BMG samples at temperature (a) T_g (b) T_x .

According to the results above, the heating rate-dependent phenomenon is observed. This rate-dependent glass transition process is due to the BMG relaxation process in the glass transition region. The grain nucleation has a strong relationship with the thermal activities. Both the Kissinger method and Ozawa results exhibit similar tendencies for these four alloy compositions. The E_g and E_x values increase with increasing Nb contents. The E_g value of the $Nb_{0.2}$ alloy is much smaller than the other three alloys, the $Nb_{0.4}$ and $Nb_{0.6}$ alloys exhibit very similar E_g values and the $Nb_{0.8}$ alloy has the highest E_g value. The E_x values of $Nb_{0.2}$, $Nb_{0.4}$ and $Nb_{0.6}$ exhibit similar values, but the $Nb_{0.8}$ shows a large increase compared with the other samples. These results indicate that the glass transition process of $Nb_{0.8}$ must overcome a higher activation barrier compared with other three alloys, which further results in higher thermal stability and resistance to crystallisation than the other three samples.

Compared with some other Cu-Zr-Al-Nb alloy systems that exhibit crystallisation phase or phase separation, their E_x values are 238 kJ/mol and 260 kJ/mol [147]. The current alloy systems exhibit relatively higher activation energies which reflects the higher thermal stability of these alloy systems.

The activation energy represents the needs of atoms to overcome the obstructions with the surrounding atoms during the different transformation processes. It also indicates the interaction between the atoms [2]. A larger activation energy of the alloy system is due to a more obvious interaction effect between the atoms. For the ternary Zr-Cu-Al alloy systems, a large negative heat of mixing can be obtained. Strong interatomic bonding ability was also observed for this alloy system [153]. Introducing Nb content with a positive heat of mixing with Zr and Cu will increase the repulsion between atoms and make the movement of the atoms become difficult. It is difficult for the Nb content to form intermetallics with Zr and Cu, consequently it will prevent the formation of the heterogeneous nucleation and enhance the formation of the amorphous phase. The atomic radius of the alloying elements are Zr = 0.16 nm, Cu = 0.128 nm, Al = 0.143 nm and Nb = 0.148 nm [154]. The addition of Nb content will contribute to local chemical inhomogeneity and the local free volume distribution fluctuation [15]. It is known that the amorphous alloy formation involves competition between the liquid phase and the corresponding crystalline phases. With a suitable cooling rate or fabrication process, the liquid phase can be stabilised during cooling which further suppress the formation of the crystalline phases. The dense-packed atomic

structure is the dominated structure of amorphous metals. The liquid phase will become more stable with a denser packing density and slower diffusion of the constituent elements [155]. According to Cao et al [156], elements with small positive heat of mixing with Cu, such as Nb = 3 kJ/mol, will retard the nucleation and growth of the crystalline phases due to the rearrangement of the positive heat of mixing upon cooling. In addition, the atomic size mismatch between the Nb and Cu will generate a higher random packing density which further stabilises the liquid phase. Thus, the Nb_{0.4}-Nb_{0.8} alloys exhibit better GFA properties. By adding suitable amounts of the Nb element, the GFAs of the alloy systems will be significantly enhanced. These results also demonstrate why some of the Zr-Cu-Al-Nb alloys exhibit composite structure such as B2-CuZr phase combined with the amorphous matrix or phase separation process. The reason is that the crystalline phase of this alloy system is mainly dominated by the long-range ordered Zr and Cu crystalline packing. It is known that the Cu element has a repulsive nature with the positive heat of mixing elements. When the Nb addition in the alloy system is not enough to support the formation of local heterogeneous structure, the long-range diffusion of the Zr and Cu will dominate the process during cooling and the formation of the crystalline CuZr phases will become easier. In addition, when the Nb addition in the alloy system has exceeded a suitable range, it will also lead to phase separation during cooling [157].

6.3.2 Mechanical properties

The four 2 mm as-cast samples were subjected to the compression test and the true compressive stress-strain curves are shown in Figure 6.6. The Nb_{0.2} exhibits an elastic strain of approximately 0 with a fracture strength of 1703 MPa. The yield strength of Nb_{0.4} is 1756 MPa and the plastic flow is 1.3 %, the Nb_{0.6} alloy shows a yield strength of 1820 MPa and the plastic flow is 1.6 %, and the Nb_{0.8} alloy exhibits a yield strength of 1790 MPa and a plastic flow of 7.1 %, which is the highest plasticity among the four compositions. None of them exhibited work-hardening behaviour during the compression tests, mainly due to the fully amorphous feature of the alloys compared with the Cu-Zr-Al-Nb BMGMCs.

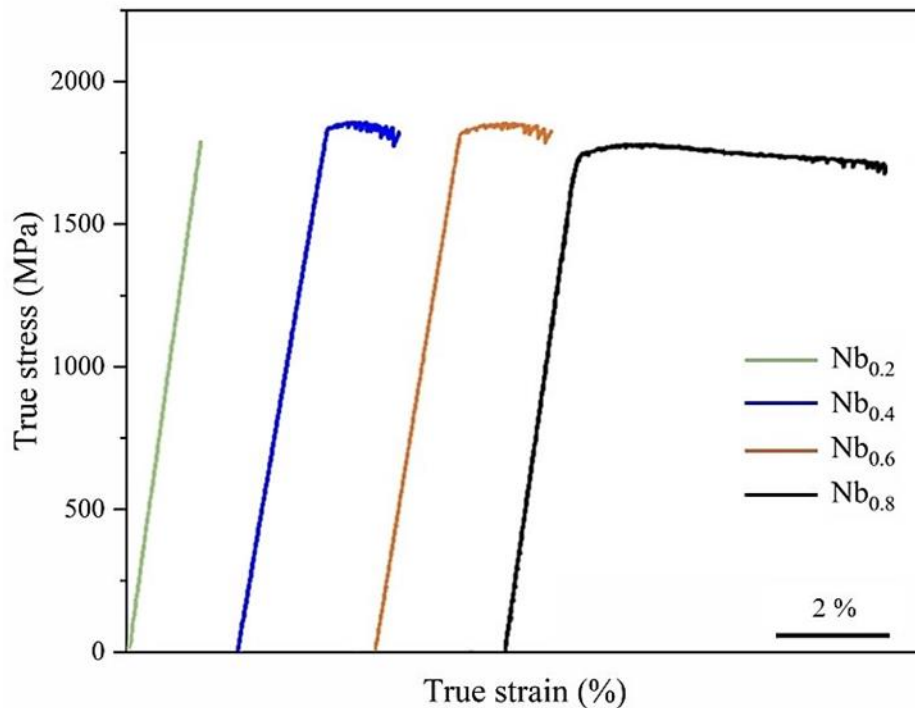


Figure 6. 6: The compressive stress-strain curves of Zr₅₀Cu_{45-x}Al₅Nb_x (x = 0.2, 0.4, 0.6 and 0.8

at. %) BMGs.

The Nb_{0.8} sample exhibited obvious plasticity compared with the other three samples. In order to examine the evolution of the microstructure during the compression test, and the reason for the enhanced plasticity of the Nb_{0.8} sample, SEM was performed for the samples. The fracture surfaces after the compression tests are shown in Figure 6.7 (a)-(f). Different shaped shear bands were obtained with a variation in Nb contents. Figure 6.7 (a) shows the fracture surface of the Nb_{0.2} sample; the very large-sized (50-100 μm) vein pattern shear bands dominate the structure. This vein pattern is the typical morphology of the BMGs after the compression tests. No secondary shear bands can be observed from the images, which lead to the rapid propagation of the large shear bands and finally contribute to cracks in the samples. Figure 6.7 (b) and (c) show the fracture surface of the Nb_{0.4} and Nb_{0.6} samples. The primary and secondary shear bands can be observed for these two alloys, and some of the river-like patterns are also observed. The different shaped and sized shear bands lead to an increase in plasticity [19]. The vein-like and river-like patterns are formed with some smooth fracture surface. These morphologies are also the typical characteristics of the amorphous alloys. Figure 6.7 (d) to (f) show the fracture surface of the Nb_{0.8} alloy; the shear band density has significantly increased. As shown in Figure 6.7 (d), typical ductile features can be observed and most of the fracture surface exhibits vein patterns with different sizes. The flocculent structure was also obtained from Figure 6.7 (f); the transformation of elastic strain into the heat energy and release the during fracture process will contribute to this unique morphology.

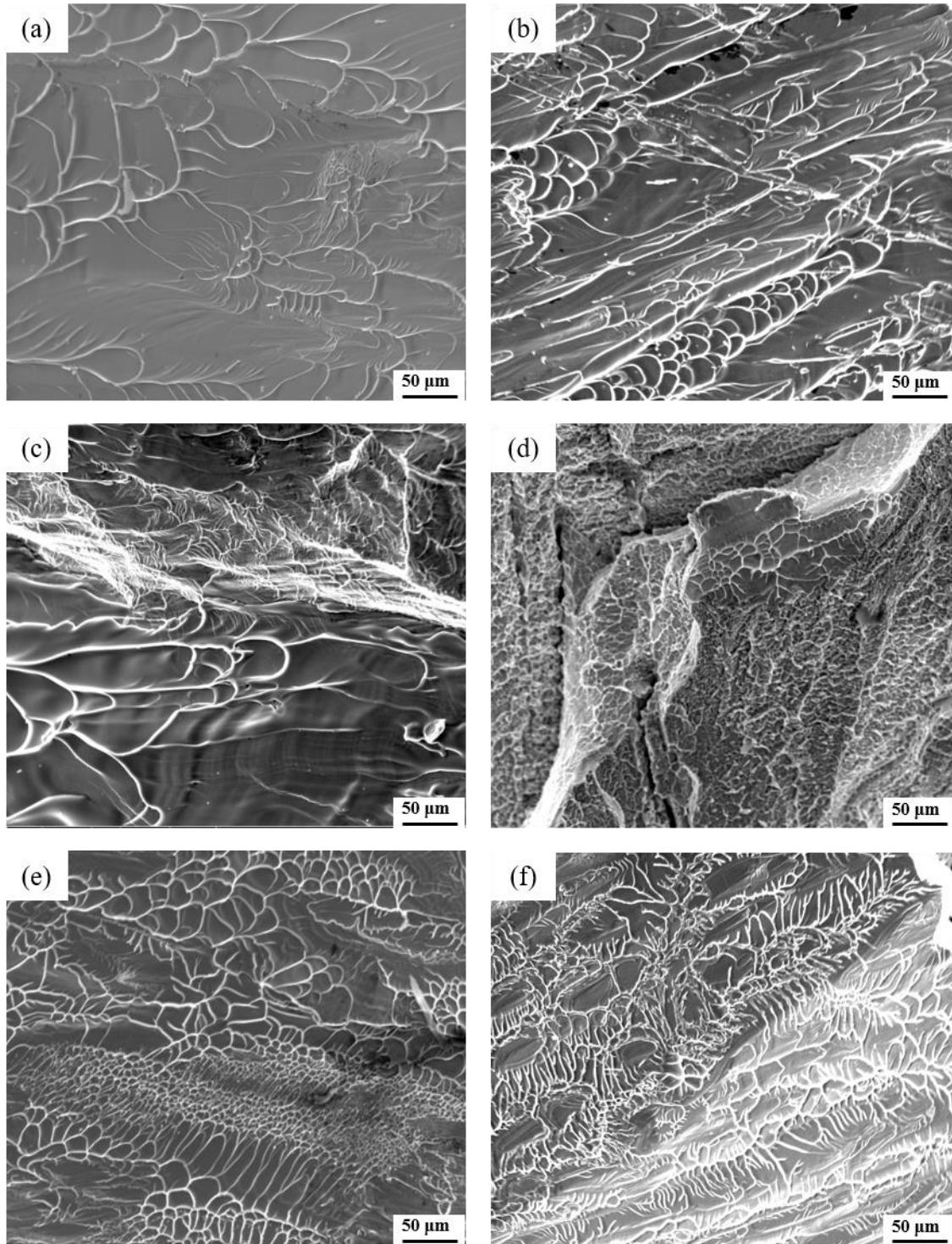


Figure 6.7: SEM images of the fracture surfaces of the (a) $Zr_{50}Cu_{44.8}Al_5Nb_{0.2}$, (b) $Zr_{50}Cu_{44.6}Al_5Nb_{0.4}$, (c) $Zr_{50}Cu_{44.4}Al_5Nb_{0.6}$, (d)-(f) $Zr_{50}Cu_{44.2}Al_5Nb_{0.8}$.

According to the literature, there are several ways to improve the plasticity of BMGs, such as: (1) deformation-induced nanocrystallisation (2) introducing a high Poisson's ratio element to the alloy system, (3) having a large free volume of the alloy and (4) introducing structure inhomogeneity [121]. The $Nb_{0.8}$ sample exhibits relatively good plasticity and the reason for the enhanced plasticity should be investigated. As shown in the XRD results, there are no crystalline structures in the as-cast 2 mm $Nb_{0.8}$ specimen. Following the compression test, the sample was checked by the HRTEM and is shown in Figure 6. 8. The fully amorphous feature is shown, and the corresponding SAED pattern exhibits a diffuse halo. This indicates that the fully amorphous feature is obtained before and after the deformation. There were no nanocrystals, ordered crystalline structures or phase separation formation. (It represents a small volume of material and may not be indicative of the whole sample).

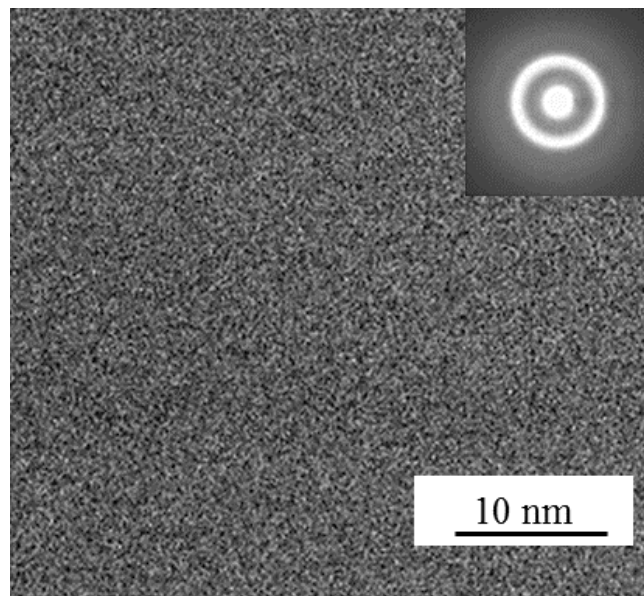


Figure 6.8: HRTEM images of the as-cast $Zr_{50}Cu_{44.2}Al_5Nb_{0.8}$ alloys with corresponding SAED.

For the fully amorphous metals, the free volume of the system can be examined. The free volume theory was introduced by Spaepen [158][159], which indicates that the shear banding process is initiated due to the free volume. The higher the free volume of the alloy system, the larger the atomic mobility. The initiation, interaction and branching of the shear bands become easier with a higher free volume. Thus, the plasticity of the alloys has a strong relationship with the free volume. The excess free volume will completely vanish when the BMGs are heated to a certain temperature [160], [161] The enthalpy change was used to reflect this process [162], [163]. For the BMG alloy systems, the area of the exothermic peak before the glass transition process in the DSC curve can be measured, which represents the enthalpy change of the alloys. The DSC built-in software was applied, and the measured values are shown in Table 6. 4.

Table 6.4: The change in enthalpy prior to the glass transition process and the fragility parameter of $Zr_{50}Cu_{45-x}Al_5Nb_x$ ($x = 0.2, 0.4, 0.6$ and 0.8 at. %) BMGs.

| | ΔH J/g | m |
|-------------------------|----------------|-------|
| Nb_{0.2} | 1.23 | 19.44 |
| Nb_{0.4} | 1.58 | 23.19 |
| Nb_{0.6} | 1.63 | 25.35 |
| Nb_{0.8} | 2.56 | 31.27 |

The results demonstrate that the Nb_{0.2} has the lowest free volume, the Nb_{0.2} and Nb_{0.6} have a similar value and the Nb_{0.8} exhibit the highest free volume of 2.56 J/g. Combining the mechanical test results, it is clear that a higher free volume leads to a higher density of the shear bands and further enhances the plasticity. A large free volume of the alloy will also enhance the formation of the vein shaped shear bands.

Amorphous materials are classified into two groups, ‘strong’ or ‘fragile’, according to the concept of fragility introduced by Angell [164]. The fragility parameter can be calculated using the equation:

$$m = \frac{E_g}{RT_g \ln 10} \quad (6.4)$$

The E_g value is obtained from the Kissinger plots and T_g is obtained from the DSC curve with 20 K/min. The m values for the four compositions are 19.44, 23.19, 25.35 and 31.27 respectively. The m values of the four samples also exhibit a trend which increases with increasing Nb content.

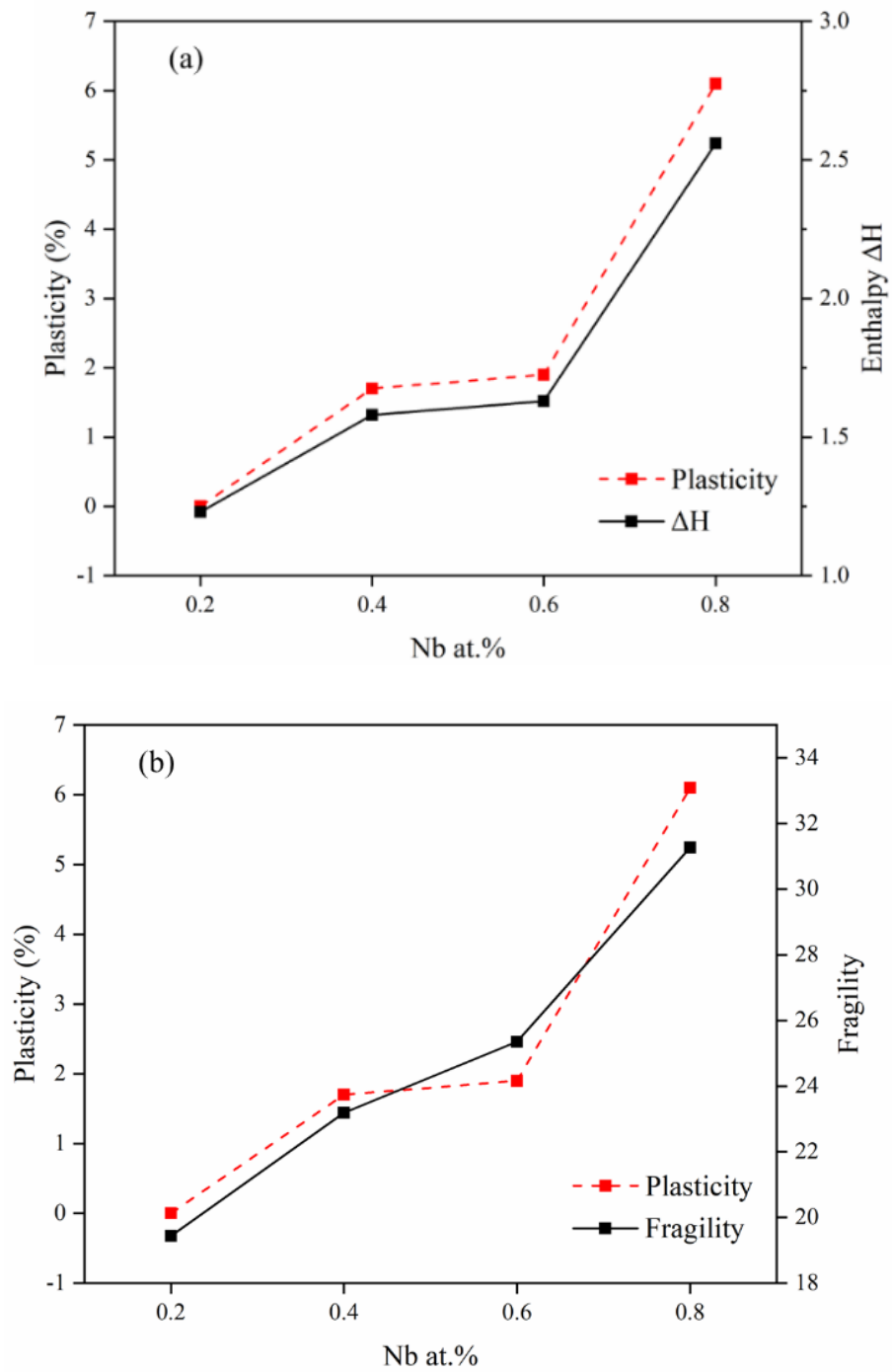


Figure 6.9: Correlation of plasticity with (a) change in enthalpy prior to the glass transition process

(b) fragility parameter of $Zr_{50}Cu_{45-x}Al_5Nb_x$ ($x = 0.2, 0.4, 0.6$ and 0.8 at. %) BMGs.

As shown in Figure 6. 9, both changes in enthalpy and fragility parameters exhibit the same trend as the plasticity. They show a near-linear function for the current four alloys. As

the change in enthalpy and fragility parameters are obtained from the DSC curves and the plasticity is obtained from the compression test, and these results exhibit a very similar trend, this further proves that the plasticity has a strong relationship with the free volume of the alloy systems. This phenomenon was also observed in some other ZrCu-based BMG systems [165][166].

The enhanced plasticity for the Nb_{0.8} alloy can be explained due to the Nb addition having a positive heat of mixing with the Cu elements and a medium atomic radius. The Nb element could cause repulsive interactions between the atoms. The atomic bonding structure will be changed when the Nb addition is introduced to the alloy system, which leads to the structure inhomogeneity and fluctuation of the free volume distribution. The nucleation and propagation of shear bands will be influenced during the deformation process. Secondary and tertiary shear bands will be generated. The shear band density is increased, and multi-shaped shear bands can be formed. The intersections and blocking between the shear bands will lead to an increase in plasticity. As can be seen from Figure 6. 7, with increasing shear band density, the movement of the shear bands becomes difficult and further resists the propagation of the shear bands, which finally leads to the enhanced plasticity.

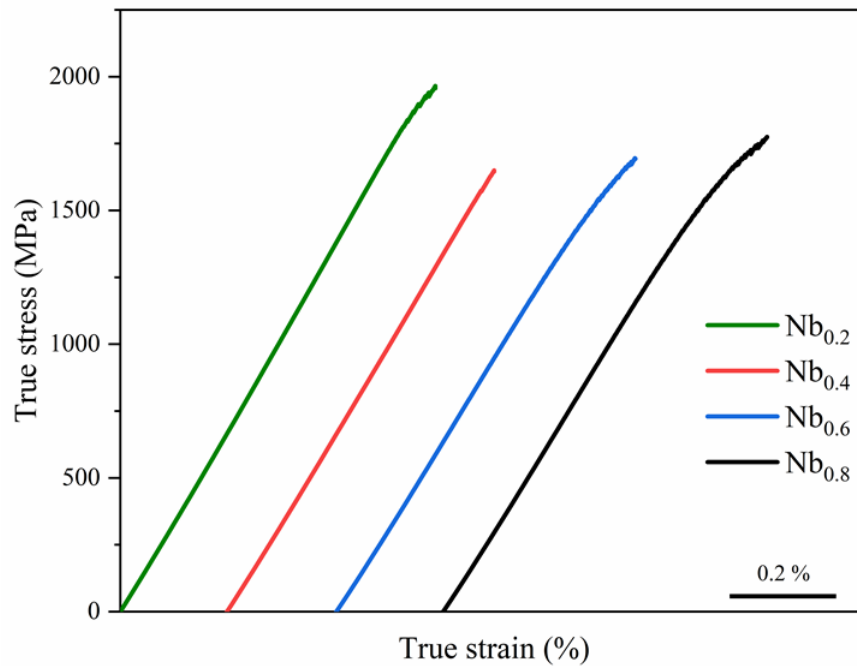


Figure 6. 10: The tensile test stress-strain curves of $Zr_{50}Cu_{45-x}Al_5Nb_x$ ($x = 0.2, 0.4, 0.6$ and 0.8 at. %) BMGs

Tensile tests were also applied to all the samples and the true stress-strain curves are shown in Figure 6. 10. The four samples exhibit very similar properties and the very high fracture strengths, which are 1993 MPa, 1720 MPa, 1726 MPa, and 1889 MPa respectively. All the specimens have exhibited plasticity $<0.1\%$ and no work-hardening ability during the tensile tests, and these are typical BMG tensile stress-strain curves. The variation of Nb addition has not contributed to the improvement of tensile properties, compared with the crystalline second phase enhanced BMGMCs. The fully amorphous microstructure cannot hinder the propagation of the large shear bands. Large shear band movement will propagate and develop until fracture of the material occurs.

6.4 Conclusions

In this chapter, the Nb element was introduced into the Zr-Cu-Al system, which has a positive mixing entropy with Cu. The GFAs, thermal stability and mechanical properties of the $Zr_{50}Cu_{45-x}Al_5Nb_x$ ($x = 0.2, 0.4, 0.6$ and 0.8 at. %) BMGs have been examined and investigated. The influence of minor Nb addition to the alloy system has been carefully studied. For the quaternary Zr-Cu-Al-Nb alloy system, it exhibits plastic strain up to 7.1 % when the Nb addition is 0.8. The $Nb_{0.4}$ to $Nb_{0.8}$ sample shows relatively good GFA with a critical diameter up to 5 mm. With suitable Nb addition, the GFA and mechanical properties can be enhanced at the same time. The non-isothermal results indicate that this alloy system has exhibited large activation energy for both the glass transition and the crystallisation process, which indicates good thermal stability of the alloy system. The improved GFA and plasticity are mainly due to the structural inhomogeneity of the amorphous phase, which is caused by introducing Nb to the alloy system. The results have indicated that the element with a positive heat mixing of with the main alloying element can also enhance the GFA and plasticity of the alloy system.

Chapter 7

Conclusion and Future Works

7.1 Conclusion

The aim of this thesis is to develop ZrCu-based BMGs or BMGMCs with improved compression and tensile properties. The main findings for the current works are summarised below.

- The alloying element effect to the base Zr-Cu-Al BMGMCs was investigated, which provided a guidance for preparing and designing medium/large sized TRIP reinforced BMGMCs. The single B2-CuZr phase as-cast sample size were increased due to the minor addition of Ag. A small amount of Ag will suppress the formation of brittle phase and stabilise the metastable B2-CuZr phase, which makes it easier to be retained during the rapid solidification process. A large amount of Ag will suppress the B2-CuZr phase formation and contribute to the formation of amorphous phase. The mechanical properties results demonstrate that a more homogenized structure with relatively small grain size is desired for the current Zr-Cu-Al based BMGMCs. The work provided a scope for designing single B2-CuZr phase structure with increased sample size.
- A new series of Zr-Cu-Al-Ag-Ti TRIP reinforced alloys were obtained based on the Zr-Cu-Al-Ag alloy system. The effects of Ti contents on the GFAs, microstructures and mechanical properties of the alloy systems were detailed studied. The addition of Ti

content enhanced the GFAs of the alloy system, the single B2-CuZr phase were obtained up to 6 mm casting size with suitable Ti contents. Transformations from single B2-CuZr phase to martensitic B19' phase are successfully observed and it is believed to cause work-hardening behaviour of the samples. The 6 mm $Zr_{49}Cu_{45}Al_4Ag_1Ti_1$ specimen exhibited work-hardening behaviour during both compression and tensile test. It shows a yield strength of 1321 MPa and fracture strength of 1563 MPa with a plastic strain of 2.3% under tension. It has the potential to be fabricated to larger sizes.

- Minor addition of Nb was introduced into the Zr-Cu-Al system, which has a positive mixing entropy with the Cu element. The GFAs, thermal stability and mechanical properties of the $Zr_{50}Cu_{45-x}Al_5Nb_x$ ($x = 0.2, 0.4, 0.6$ and 0.8 at. %) BMGs have been examined and investigated. For the quaternary Zr-Cu-Al-Nb alloy system, it exhibits plastic strain up to 7.1 % when the Nb addition is 0.8. The $Nb_{0.4}$ to $Nb_{0.8}$ sample shows relatively good GFA with a critical diameter up to 5 mm. With suitable Nb addition, the GFA and plasticity can be enhanced at the same time. The non-isothermal results indicate that this alloy system has exhibited large activation energy for both the glass transition and the crystallisation process, which indicates good thermal stability of the alloy system. The improved GFA and plasticity are mainly due to the structural inhomogeneity of the amorphous phase, which is caused by introducing Nb to the alloy system. The results have indicated that the element with a positive heat mixing of with the main alloying element can also enhance the GFA and plasticity of the alloy system.

7.2 Future work

- Perform nano-indentation tests to the B2-CuZr phase and glass matrix for the $Zr_{50}Cu_{45-x}Al_5Ag_x$ ($x = 0, 0.5, 1, \text{ and } 2 \text{ at.}\%$) alloy system which will provide a more detailed view of the mechanical properties of the different phases within this alloy system.
- Perform tensile tests for the rest of 6 mm $Zr_{50-x}Cu_{44}Al_5Ag_1Ti_x$ ($x=0.5, 1, 2, 3, 4$ and $5 \text{ at } \%$) alloys. Deformed samples should be examined by TEM and HRTEM. The nano-sized twin features obtained from $Zr_{49}Cu_{45}Al_4Ag_1Ti_1$ sample should be investigated to get deeper understanding of the martensitic transformation. The relationship between the volume fraction of the B2-CuZr and tensile properties should be further investigated.
- Increase the casting size above 6 mm and check if TRIP effect can still be obtained for the Zr-Cu-Al-Ag-Ti system.
- The design strategy should be further modified and try to obtain more TRIP reinforced BMGMCs based on this strategy.
- The strain rate effect to the Zr-Cu-Al-Nb alloys can be studied.
- More samples with large Nb additions can be prepared and tested. The GFAs and mechanical properties can be examined and compared with the current researches.

References

- [1] W. L. Johnson, "Bulk glass-forming metallic alloys: science and technology," *MRS Bull.*, vol. 24(10), pp. 42-53, 1999.
- [2] A. Inoue and C. Suryanarayana, "*Bulk Metallic Glasses*". CRC Press, 2017.
- [3] A.L. Greer, "Metallic Glasses," in *Physical Metallurgy: Fifth Edition*, Elsevier, vol. 1, p. 305, 2014.
- [4] M.F. Ashby and A.L. Greer, "Metallic glasses as structural materials," *Scr. Mater.*, vol. 54(3), pp. 321-326, 2006.
- [5] A. L. Greer, "Metallic glasses...on the threshold," *Materials Today*, vol. 12(1-2). pp. 14-22, 2009.
- [6] M. Chen, "A brief overview of bulk metallic glasses," *NPG Asia Materials*. vol. 3(9), p. 82, 2011.
- [7] R. Busch, W. Liu, and W. L. Johnson, "Thermodynamics and kinetics of the Mg₆₅Cu₂₅Y₁₀ bulk metallic glass forming liquid," *J. Appl. Phys.*, vol. 83(8), pp. 4131-4141, 1998.
- [8] H. W. Kui, A. L. Greer, and D. Turnbull, "Formation of bulk metallic glass by fluxing," *Appl. Phys. Lett.*, vol. 45(6), pp. 615-616, 1984.
- [9] X. H. Lin and W. L. Johnson, "Formation of Ti-Zr-Cu-Ni bulk metallic glasses," *J. Appl. Phys.*, vol. 78(11), pp. 6514-6519, 1995.
- [10] Q. Yu, X. D. Wang, H. B. Lou, Q. P. Cao, and J. Z. Jiang, "Atomic packing in Fe-based metallic glasses," *Acta Mater.*, vol. 102, pp. 116-124, 2016.
- [11] B. J. Yang, J. H. Yao, Y. S. Chao, J. Q. Wang, and E. Ma, "Developing aluminum-based bulk metallic glasses," *Philos. Mag.*, vol. 90(23), pp. 3215-3231, 2010.
- [12] J. D. Cao, N. T. Kirkland, K. J. Laws, N. Birbilis, and M. Ferry, "Ca-Mg-Zn bulk metallic glasses as bioresorbable metals," *Acta Biomater.*, vol. 8(6), pp. 2375-2383, 2012.

- [13] L. Ge, X. Hui, E. R. Wang, G. L. Chen, R. Arroyave, and Z. K. Liu, "Prediction of the glass forming ability in Cu-Zr binary and Cu-Zr-Ti ternary alloys," *Intermetallics*, vol. 16(1), pp. 27–33, 2008.
- [14] Q. K. Jiang, G.Q. Yang, L. Yang, X.D. Wang, K. Saksl, H. Franz, R. Wunderlich, H. Fecht and J.Z. Jiang, "La-based bulk metallic glasses with critical diameter up to 30 mm," *Acta Mater.*, vol. 55(13), pp. 4409-4418, 2007.
- [15] M. B. Gawande, A. Goswami, Fx. Felpin, T. Asefa, X.X. Huang. R. Silva, X.X. Zou, R. Zboril and Rs. Varma, "Cu and Cu-Based Nanoparticles: Synthesis and Applications in Catalysis," *Chemical Reviews*. vol. 116(6), pp. 3722-3811, 2016.
- [16] W. H. Wang, J. J. Lewandowski, and A. L. Greer, "Understanding the glass-forming ability of Cu₅₀Zr₅₀ alloys in terms of a metastable eutectic," *J. Mater. Res.*, vol. 20(9), pp. 2307-2313, 2005.
- [17] D. Ma, H. Tan, D. Wang, Y. Li, and E. Ma, "Strategy for pinpointing the best glass-forming alloys," *Appl. Phys. Lett.*, vol. 86(19), p. 191906, 2005.
- [18] Z. Evenson, I. Gallino, and R. Busch, "The effect of cooling rates on the apparent fragility of Zr-based bulk metallic glasses," *J. Appl. Phys.*, vol. 107(12), p. 123529, 2010.
- [19] C.A. Schuh, T.C. Hufnagel, and U. Ramamurty, "Mechanical behavior of amorphous alloys," *Acta Mater.*, vol. 55(12), pp. 4067-4109, 2007.
- [20] J.J. Lewandowski, W.H. Wang, and A. L. Greer, "Intrinsic plasticity or brittleness of metallic glasses," *Philos. Mag. Lett.*, vol. 85(2), pp. 77–87, 2005.
- [21] D. H. Kim, W. T. Kim, E. S. Park, N. Mattern, and J. Eckert, "Phase separation in metallic glasses," *Progress in Materials Science*.vol. 58(8), pp. 1103-1172, 2013.
- [22] D.C. Hofmann, J.Y. Suh, A. Wiest, G. Duan, M.L. Lind, M.D. Demetriou and W.L. Johnson, "Designing metallic glass matrix composites with high toughness and tensile ductility," *Nature*, vol. 451(7182), p. 1085, 2008.
- [23] D. C. Hofmann, "Shape Memory Bulk Metallic Glass Composites," *Science (80-.)*,

- vol. 329(5997), pp. 1294–1295, 2010.
- [24] Z. T. Wang, J. Pan, Y. Li, and C. A. Schuh, “Densification and strain hardening of a metallic glass under tension at room temperature,” *Phys. Rev. Lett.*, vol. 111(13), p. 135504, 2013.
- [25] P. B. Macedo and T. A. Litovitz, “On the relative roles of free volume and activation energy in the viscosity of liquids,” *J. Chem. Phys.*, vol. 42(1), pp. 245-256, 1965.
- [26] D. Turnbull and M. H. Cohen, “On the free-volume model of the liquid-glass transition,” *J. Chem. Phys.*, vol. 52(6), pp. 3038-3041, 1970.
- [27] A. Inoue, M. Yamamoto, H. M. Kimura, and T. Masumoto, “Ductile aluminium-base amorphous alloys with two separate phases,” *J. Mater. Sci. Lett.*, vol. 6(2), pp. 194-196, 1987.
- [28] H. Choi-Yim and W. L. Johnson, “Bulk metallic glass matrix composites,” *Appl. Phys. Lett.*, vol. 71(26), pp. 3808-3810, 1997.
- [29] K. Wang, T. Fujita, M.W. Chen, T.G. Nieh, H. Okada, K. Koyama, W. Zhang and A. Inoue., “Electrical conductivity of a bulk metallic glass composite,” *Appl. Phys. Lett.*, vol. 91(15), p. 154101, 2007.
- [30] J. Eckert, J. Das, S. Pauly, and C. Duhamel, “Mechanical properties of bulk metallic glasses and composites,” *J. Mater. Res.*, vol. 22(2), pp. 285–301, 2007.
- [31] S. Pauly, J. Das, J. Bednarcik, N. Mattern, K.B. Kim, D.H. Kim and J. Eckert., “Deformation-induced martensitic transformation in Cu-Zr-(Al,Ti) bulk metallic glass composites,” *Scr. Mater.*, vol. 60(6), pp. 431–434, 2009.
- [32] P. Gargarella, S. Pauly, K.K. Song, J. Hu, N.S. Barekar, M. Samadi khoshkhoo, A. Teresiak, H. Wendrock, U. Kuhn, C. Ruffing, E. Kerscher and J. Eckert., “Ti-Cu-Ni shape memory bulk metallic glass composites,” *Acta Mater.*, vol. 61(1), pp. 151-162, 2013.
- [33] Y. Wu, H. Wu, Z. Zhang, X. Hui, G. Chen, X. Wang and Z.P. Lv., “Formation of Cu-Zr-Al bulk metallic glass composites with improved tensile properties,” *Acta Mater.*,

- vol. 59(8), pp. 2928–2936, 2011.
- [34] W. Klement, R. H. Willens, and P. Duwez, “Non-crystalline structure in solidified Gold-Silicon alloys,” *Nature*, vol. 187(4740), pp. 869–870, 1960.
- [35] R. Pond and R. Maddin, “A Method of Producing Rapidly Solidified Filamentary Castings,” *Met Soc AIME-Trans*, vol. 245(11), pp. 2457-2476, 1969.
- [36] H. A. Davies and B. G. Lewis, “A generalised kinetic approach to metallic glass formation,” *Scr. Metall.*, vol. 9(10), pp. 1107-1112, 1975.
- [37] H. A. Davies, J. Aucote, and J. B. Hull, “The kinetics of formation and stabilities of metallic glasses,” *Scr. Metall.*, vol. 8(10), pp. 1179-1189, 1974.
- [38] H. A. Davies, “The kinetics of formation of A AuGeSi metallic glass,” *J. Non. Cryst. Solids*, vol. 17(2), pp. 266–272, 1975.
- [39] J. Schroers, B. Lohwongwatana, W. L. Johnson, and A. Peker, “Gold based bulk metallic glass,” *Appl. Phys. Lett.*, vol. 87(6), p. 06912, 2005.
- [40] A. J. Drehman, A. L. Greer, and D. Turnbull, “Bulk formation of a metallic glass: Pd₄₀Ni₄₀P₂₀,” *Appl. Phys. Lett.*, vol. 41, p. 716, 1982.
- [41] A. P. and W. L. Johnson, “A highly processable metallic glass: Zr_{41.2}Ti_{13.8}Cu_{12.5}Ni_{10.0}Be_{22.5},” *Appl. Phys. Lett.*, vol. 63(17), pp. 2342-2344, 1993.
- [42] W. Chen, Y. Wang, J. Qiang, and C. Dong, “Bulk metallic glasses in the Zr-Al-Ni-Cu system,” *Acta Mater.*, vol. 51(7), pp. 1899-1907, 2003.
- [43] A. Inoue, “Stabilization of metallic supercooled liquid and bulk amorphous alloys,” *Acta Mater.*, vol. 48(1), pp. 279-306, 2000.
- [44] Z.P. Lu, C.T. Liu, C.A. Carmichael, W.D. Porter, and S.C. Deevi, “Bulk Glass Formation in an Fe-Based Fe–Y–Zr–M (M = Cr, Co, Al)–Mo–B System,” *J. Mater. Res.*, vol. 19(3), pp. 921-929, 2004.
- [45] H. Ma, L. L. Shi, J. Xu, Y. Li, and E. Ma, “Improving glass-forming ability of Mg-Cu-Y via substitutional alloying: Effects of Ag versus Ni,” *J. Mater. Res.*, vol. 21(9), pp. 2204-2215, 2006.

- [46] S. Basak, R. Clarke, and S. R. Nagel, "Temperature dependence of the structure factor in Nb-Ni glasses," *Phys. Rev. B*, vol. 20, p. 4278, 1979.
- [47] J. P. Carini, S. Basak, S. R. Nagel, B. C. Giessen, and C. L. Tsai, "The thermoelectric power of the metallic glass $\text{Ca}_{0.8}\text{Al}_{0.2}$," *Phys. Lett. A*, vol. 81(9), pp. 525-526, 1981.
- [48] D. Turnbull, "Under What Conditions Can A Glass Be Formed," *Contemp. Phys.*, vol. 10, pp. 473-488, 1969.
- [49] F. C. Frank and J. S. Kasper, "Complex alloy structures regarded as sphere packings. I. Definitions and basic principles," *Acta Crystallogr.*, vol. 11, pp. 184-190, 1958.
- [50] F. C. Frank and J. S. Kasper, "Complex alloy structures regarded as sphere packings. II. Analysis and classification of representative structures," *Acta Crystallogr.*, vol. 12, pp. 483-499, 1959.
- [51] Y. J. Sun, D.D. Qu, Y.J. Huang, K.D. Liss, X.S. Wei, D.W. Xing and J. Shen., "Zr-Cu-Ni-Al bulk metallic glasses with superhigh glass-forming ability," *Acta Mater.*, vol. 57(4), pp. 1290-1299, 2009.
- [52] R. Busch and I. Gallino, "Kinetics, Thermodynamics, and Structure of Bulk Metallic Glass Forming Liquids," *Jom*, vol. 69(11), pp. 2178–2186, 2017.
- [53] R. Busch, J. Schroers, and W. H. Wang, "Thermodynamics and kinetics of bulk metallic glass," *MRS Bull.*, vol. 32(8), pp. 620-623, 2007.
- [54] T. A. Waniuk, R. Busch, A. Masuhr, and W. L. Johnson, "Equilibrium viscosity of the $\text{Zr}_{41.2}\text{Ti}_{13.8}\text{Cu}_{12.5}\text{Ni}_{10}\text{Be}_{22.5}$ bulk metallic glass-forming liquid and viscous flow during relaxation, phase separation, and primary crystallization," *Acta Mater.*, vol. 46(15), pp. 5229-5236, 1998.
- [55] A. Masuhr, T. A. Waniuk, R. Busch, and W. L. Johnson, "Time scales for viscous flow, atomic transport, and crystallization in the liquid and supercooled liquid states of $\text{Zr}_{41.2}\text{Ti}_{13.8}\text{Cu}_{12.5}\text{Ni}_{10}\text{Be}_{22.5}$," *Phys. Rev. Lett.*, vol. 82(11), pp. 2290-2293, 1999.
- [56] Z.P. Lu and C.T. Liu, "A new glass-forming ability criterion for bulk metallic glasses," *Acta Mater.*, vol. 50(13), pp. 3501-3512, 2002.

- [57] Z. P. Lu, Y. Li, and S. C. Ng, "Reduced glass transition temperature and glass forming ability of bulk glass forming alloys," *J. Non. Cryst. Solids*, vol. 270(1), pp. 103-114, 2000.
- [58] R. Busch, "Thermophysical properties of bulk metallic glass-forming liquids," *JOM*, vol. 52(7), pp. 39-42, 2000.
- [59] J. Torrens-Serra, S. Venkataraman, M. Stoica, U. Kuehn, S. Roth, and J. Eckert, "Non-isothermal kinetic analysis of the crystallization of metallic glasses using the master curve method," *Materials (Basel)*, vol. 4(12), pp. 2231-2243, 2011.
- [60] K. Song, X. Bian, J. Guo, X. Li, M. Xie, and C. Dong, "Study of non-isothermal primary crystallization kinetics of $\text{Al}_{84}\text{Ni}_{12}\text{Zr}_1\text{Pr}_3$ amorphous alloy," *Journal of Alloys and Compounds*, vol. 465(1), pp. L7-L13, 2008.
- [61] R. Böhmer, K. L. Ngai, C. A. Angell, and D. J. Plazek, "Nonexponential relaxations in strong and fragile glass formers," *J. Chem. Phys.*, vol. 99(5), pp. 4201-4209, 1993.
- [62] K. M. Cole, D. W. Kirk, C. V. Singh, and S. J. Thorpe, "Role of niobium and oxygen concentration on glass forming ability and crystallization behavior of Zr-Ni-Al-Cu-Nb bulk metallic glasses with low copper concentration," *J. Non. Cryst. Solids*, vol. 445-446, pp. 88-94, 2016.
- [63] Z. P. Lu and C. T. Liu, "Role of minor alloying additions in formation of bulk metallic glasses: A review," *Journal of Materials Science*, vol. 39(12), pp. 3965-3974, 2004.
- [64] A. Inoue and T. Zhang, "Fabrication of Bulky Zr-Based Glassy Alloys by Suction Casting Into Copper Mold," *Mater. Trans. JIM*, vol. 36, p. 1184, 1995.
- [65] O. Haruyama, Y. Nakayama, R. Wada, H. Tokunaga, J. Okada, T. Ishikawa and Y. Yokoyama, "Volume and enthalpy relaxation in $\text{Zr}_{55}\text{Cu}_{30}\text{Ni}_5\text{Al}_{10}$ bulk metallic glass," *Acta Mater.*, vol. 58(5), pp. 1829-1836, 2010.
- [66] W. Zhang, Q. Zhang, C. Qin, and A. Inoue, "Synthesis and properties of Cu-Zr-Ag-Al glassy alloys with high glass-forming ability," *Mater. Sci. Eng. B Solid-State Mater. Adv. Technol.*, vol. 148(1), pp. 92-96, 2008.

- [67] Q.K. Jiang, Q.K. Jiang, X.D. Wang, X.P. Nie, G.Q. Zhang, H. Ma, H. J. Fecht, J. Bendnarcik, H. Franz, Y.G. Liu, Q.P. Cao and J.Z.Jiang., “Zr-(Cu,Ag)-Al bulk metallic glasses,” *Acta Mater.*, vol. 56(8), pp. 1785-1796, 2008.
- [68] L. E. Tanner and R. Ray, “Physical properties of Ti₅₀Be₄₀Zr₁₀ glass,” *Scr. Metall.*, vol. 11(9), pp. 783-789, 1977.
- [69] H. Men, S. Pang, A. Inoue, and T. Zhang, “New Ti-based bulk metallic glasses with significant plasticity,” *Mater. Trans.*, vol. 46(10), p. 2218, 2005.
- [70] Y. C. Kim, W. T. Kim, and D. H. Kim, “A development of Ti-based bulk metallic glass,” *Mater. Sci. Eng. A*, vol. 375-377, pp. 127-135, 2004.
- [71] P. Gong, K. F. Yao, and Y. Shao, “Lightweight Ti-Zr-Be-Al bulk metallic glasses with improved glass-forming ability and compressive plasticity,” *J. Non. Cryst. Solids*, vol. 358(18–19), pp. 2620–2625, 2012.
- [72] L. Wang and A. Inoue, “Icosahedral and amorphous phases in melt-spun Ti-Zr-Ni-Cu alloys,” *Mater. Trans.*, vol. 42(12), p. 2637, 2001.
- [73] J. Eckert, J. Das, S. Pouly, and C. Duhamel, “Processing routes/ microstructure and mechanical properties of metallic glasses and their composites,” *Adv. Eng. Mater.*, vol.9(6), pp. 443-453, 2007.
- [74] C. C. Hays, C. P. Kim, and W. L. Johnson, “Improved mechanical behavior of bulk metallic glasses containing in situ formed ductile phase dendrite dispersions,” *Mater. Sci. Eng. A*, vol. 304, pp. 650-655, 2001.
- [75] Y. Li, S. J. Poon, G. J. Shiflet, J. Xu, D. H. Kim, and J. F. Löffler, “Formation of bulk metallic glasses and their composites,” *MRS Bull.*, vol. 32(8), pp. 624-628, 2007.
- [76] D. C. Hofmann, “Bulk Metallic Glasses and Their Composites: A Brief History of Diverging Fields,” *J. Mater.*, vol. 849, pp. 71-75, 2013.
- [77] Z. Wang, K. Gerogarakis, K.S. Nakayama, Y. Li, A.A. Tsarkov, G. Xie, D. Dudina, D.V. Louzguine-luzgin and A.R. Yavari., “Microstructure and mechanical behavior of metallic glass fiber-reinforced Al alloy matrix composites,” *Sci. Rep.*, vol. 6, p.

- 24384, 2016.
- [78] B. J. Kim, Y. S. Yun, W. T. Kim, and D. H. Kim, "Microstructure Evolution During Solidification of Cu–Zr–Ti Alloy Forming B2 Phase Particles Embedded in a Glassy Matrix," *Met. Mater. Int.*, vol. 24(5), pp. 926–933, 2018.
- [79] J. Z. Jiang, D. Hofmann, D. J. Jarvis, and H. J. Fecht, "Low-density high-strength bulk metallic glasses and their composites: A review," *Adv. Eng. Mater.*, vol. 17(6), pp. 761-780, 2015.
- [80] C. Fan and A. Inoue, "Ductility of bulk nanocrystalline composites and metallic glasses at room temperature," *Appl. Phys. Lett.*, vol. 77(1), pp. 46-48, 2000.
- [81] D. C. Hofmann, "Bulk Metallic Glasses and Their Composites: A Brief History of Diverging Fields," *J. Mater.*, vol. 2013, pp. 1–8, 2013.
- [82] C. C. Hays, C. P. Kim, and W. L. Johnson, "Microstructure controlled shear band pattern formation and enhanced plasticity of bulk metallic glasses containing in situ formed ductile phase dendrite dispersions," *Phys. Rev. Lett.*, vol. (84), p. 2901, 2000.
- [83] J. W. Qiao, T. Zhang, F. Q. Yang, P. K. Liaw, S. Pauly, and B. S. Xu, "A tensile deformation model for in-situ dendrite/metallic glass matrix composites," *Sci. Rep.*, Vol. 3. p. 2816, 2013.
- [84] Y. Wu, W.L. Song, J. Zhou, D. Cao, H. Wang, X.J. Liu, Z.P. Lv., "Ductilization of bulk metallic glassy material and its mechanism," *Wuli Xuebao/Acta Phys. Sin.*, vol. 66(17), pp. 1–18, 2017.
- [85] C. E. Borja, I. A. Figueroa, O. Lozada-Flores, M. Estrada, G.A. Lara-rodríguez, and J.A. Verduzco, "Glass formation, thermal and mechanical properties of ZrCuAlNi bulk metallic glasses," *Trans. Nonferrous Met. Soc. China (English Ed.)*, vol. 28(6), pp. 1157–1165, 2018.
- [86] P. Denis, C. M. Meylan, C. Ebner, A. L. Greer, M. Zehetbauer, and H. J. Fecht, "Rejuvenation decreases shear band sliding velocity in Pt-based metallic glasses," *Mater. Sci. Eng. A*, vol. 684, pp. 517–523, 2017.

- [87] A. L. Greer, "Metallic glasses on the threshold," *Mater. Today*, vol. 12(1–2), pp. 14–22, 2009.
- [88] X. D. Wang, H. B. Lou, Y. Gong, U. Vainio, and J. Z. Jiang, "Heterogeneities in CuZr-based bulk metallic glasses studied by x-ray scattering," *J. Phys. Condens. Matter*, vol. 23(7), pp. 075402, 2011.
- [89] P. E. Donovan, "A yield criterion for Pd₄₀Ni₄₀P₂₀ metallic glass," *Acta Metall.*, vol. 37(2), 445-456, 1989.
- [90] D. H. Kim, W. T. Kim, E. S. Park, N. Mattern, and J. Eckert, "Phase separation in metallic glasses," *Prog. Mater. Sci.*, vol. 58(8), pp. 1103–1172, 2013.
- [91] C. P. Peter Chou and D. Turnbull, "Transformation behavior of PdAuSi metallic glasses," *J. Non. Cryst. Solids*, vol. 17(2), pp. 169-188, 1975.
- [92] Y. Yokoyama, T. Yamasaki, P. K. Liaw, R. A. Buchanan, and A. Inoue, "Glass-structure changes in tilt-cast Zr-Cu-Al glassy alloys," *Mater. Sci. Eng. A*, vol. 449–451, pp. 621–626, 2007.
- [93] H. S. Chen, "Glass temperature, formation and stability of Fe, Co, Ni, Pd and Pt based glasses," *Mater. Sci. Eng.*, vol. 23(2), pp. 151-154, 1976.
- [94] J. He, H. Li, B. Yang, J. Zhao, H. Zhang, and Z. Hu, "Liquid phase separation and microstructure characterization in a designed Al-based amorphous matrix composite with spherical crystalline particles," *J. Alloys Compd.*, vol. 489(2), pp. 535-540, 2010.
- [95] Q. P. Cao, J. F. Li, Y. H. Zhou, A. Horsewell, and J. Z. Jiang, "Effect of rolling deformation on the microstructure of bulk Cu₆₀Zr₂₀Ti₂₀ metallic glass and its crystallization," *Acta Mater.*, vol. 54(16), pp. 4373-4383, 2006.
- [96] R. L. Freed and J. B. Vander Sande, "A study of the crystallization of two non-crystalline CuZr alloys," *J. Non. Cryst. Solids*, vol. 27(1), pp. 9-28, 1978.
- [97] X.H. Du, J.C. Huang, K.C. Hsieh, J.S.C. Jang, P.K. Liaw, H.M. Chen, H.S. Chou, Y.H. Lai., "Designing ductile Zr-based bulk metallic glasses with phase separated microstructure," *Adv. Eng. Mater.*, vol. 11(5), pp. 387-391, 2009.

- [98] S. S. Chen, H. R. Zhang, and I. Todd, "Phase-separation-enhanced plasticity in a $\text{Cu}_{47.2}\text{Zr}_{46.5}\text{Al}_{5.5}\text{Nb}_{0.8}$ bulk metallic glass," *Scr. Mater.*, vol. 72-73, pp. 47-50, 2014.
- [99] G. N. Greaves, A. L. Greer, R. S. Lakes, and T. Rouxel, "Poisson's ratio and modern materials," *Nature Materials*. vol. 10(11), p. 823, 2011.
- [100] J. S. Harmon, M. D. Demetriou, W. L. Johnson, and K. Samwer, "Anelastic to plastic transition in metallic glass-forming liquids," *Phys. Rev. Lett.*, vol. 99(13), p. 135502, 2007.
- [101] M.D. Demetriou, M.E. Launey, G. Garrett, J.P. Schramm, D.C. Hofmann, W.L. Johnson and R.O. Ritchie., "A damage-tolerant glass," *Nat. Mater.*, vol. 10(2), p. 123, 2011.
- [102] P. Yu and H. Y. Bai, "Poisson's ratio and plasticity in CuZrAl bulk metallic glasses," *Mater. Sci. Eng. A*, vol. 485(1), pp. 1-4, 2008.
- [103] L. Zhang, Y. Q. Cheng, A. J. Cao, J. Xu, and E. Ma, "Bulk metallic glasses with large plasticity: Composition design from the structural perspective," *Acta Mater.*, vol. 57(4), pp. 1154-1164, 2009.
- [104] J. H. Na, E. S. Park, Y. C. Kim, E. Fleury, W. T. Kim, and D. H. Kim, "Poisson's ratio and fragility of bulk metallic glasses," *J. Mater. Res.*, vol. 23(2), pp. 523-528, 2008.
- [105] W. Song, K. Song, Z. Liu, R. Li, Y. Wu, and Z. Lu, "TRIP-reinforced bulk metallic glass," *Mater. China*, vol. 33(5), pp. 300-311, 2014.
- [106] Y. Wu, Y. Xiao, G. Chen, C. T. Liu, and Z. Lu, "Bulk metallic glass composites with transformation-mediated work-hardening and ductility," *Adv. Mater.*, vol. 22(25), pp. 2770-2773, 2010.
- [107] S. Pauly, J. Das, J. Bednarcik, N. Mattern, K.B. Kim, D.H. Kim and J. Eckert., "Deformation-induced martensitic transformation in Cu-Zr-(Al,Ti) bulk metallic glass composites," *Scr. Mater.*, vol. 60(6), pp. 431-434, 2009.
- [108] B. Escher, I. Kaban, U. Kühn, J. Eckert, and S. Pauly, "Stability of the B2 CuZr phase

- in Cu-Zr-Al-Sc bulk metallic glass matrix composites,” *J. Alloys Compd.*, vol. 790, pp. 657–665, 2019.
- [109] S. Pauly, J. Das, C. Duhamel, and J. Eckert, “Effect of titanium on microstructure and mechanical properties of $\text{Cu}_{50}\text{Zr}_{50-x}\text{Ti}_x$ ($2.5 \leq x \leq 7.5$) glass matrix composites,” in *Metallurgical and Materials Transactions A: Physical Metallurgy and Materials Science*, 2008, vol. 39(8), pp. 1868–1873.
- [110] Y. Wu, H. Wang, X.J. Liu, X.H. Chen, X.D. Hui, Y. Zhang and Z.P. Lv., “Designing Bulk Metallic Glass Composites with Enhanced Formability and Plasticity,” *J. Mater. Sci. Technol.*, vol. 30(6), pp. 566–575, 2014.
- [111] G. Q. Liu, S. Z. Kou, C. Y. Li, Y. C. Zhao, and H. L. Suo, “Effect of minor Fe addition on glass forming ability and mechanical properties of $\text{Zr}_{55}\text{Al}_{10}\text{Ni}_{15}\text{Cu}_{30}$ bulk metallic glass,” *Trans. Nonferrous Met. Soc. China English Ed.*, vol. 22(3), pp. 590–595, 2012.
- [112] I.V. Okulov, U. Kuehn, J. Romberg, I. Soldatov, J. Freudenberger, L. Schultz, A. Eschke, C-G. Oertel, W. Skrotzki and J. Eckert., “Mechanical behavior and tensile/compressive strength asymmetry of ultrafine structured Ti-Nb-Ni-Co-Al alloys with bi-modal grain size distribution,” *Mater. Des.*, vol. 62 pp. 14-20, 2014.
- [113] W.L. Song, Y. Wu, H. Wang, X.J. Liu, H.W. Chem, Z.X. Guo and Z.P. Lv., “Microstructural Control via Copious Nucleation Manipulated by In Situ Formed Nucleants: Large-Sized and Ductile Metallic Glass Composites,” *Adv. Mater.*, vol. 28(37), pp. 8156-8161, 2016.
- [114] J. Schroers, “Processing of bulk metallic glass,” *Advanced Materials*. vol. 22(14), pp. 1566-1597, 2010.
- [115] M. Miller and P. Liaw, *Bulk metallic glasses: An overview*. Springer, Boston, MA, 2008.
- [116] G. Kumar, A. Desai, and J. Schroers, “Bulk Metallic Glasses: the smaller the better,” *Adv. Mater.*, vol. 23(4), pp. 461-476, 2011.
- [117] H. Wang, “Bulk metallic glass composites,” *J. Mater. Sci. Technol.*, vol. 329(5997),

- pp. 1294-1295, 2005.
- [118] J. Qiao, H. Jia, and P. K. Liaw, “Metallic glass matrix composites,” *Materials Science and Engineering R: Reports*. vol. 100, pp. 1-69, 2016.
- [119] F. F. Wu, K. C. Chan, S. S. Jiang, S. H. Chen, and G. Wang, “Bulk metallic glass composite with good tensile ductility, high strength and large elastic strain limit,” *Sci. Rep.*, vol. 4, pp. 1–6, 2014.
- [120] M. Ferry K.J. Laws, C. White, D.M. Miskovic, K.F. Shamlaye, W. Xu and O. Biletska., “Recent developments in ductile bulk metallic glass composites,” *MRS Commun.*, vol. 3(1), pp. 1-12, 2013.
- [121] Y. Wu, H. Wang, X.J. Liu, X.H. Chen, X.D. Hui, Y. Zhang and Z.P. Lv., “Designing Bulk Metallic Glass Composites with Enhanced Formability and Plasticity,” *J. Mater. Sci. Technol.*, vol. 30(6), 99. 566-575, 2014.
- [122] K. K. Song, S. Pauly, Y. Zhang, R. Li, S. Gorantla, N. Narayanan, U. Kuhn, T. Gemming and J. Eckert., “Triple yielding and deformation mechanisms in metastable $\text{Cu}_{47.5}\text{Zr}_{47.5}\text{Al}_5$ composites,” *Acta Mater.*, vol. 60(17), pp. 6000–6012, 2012.
- [123] T. Yamamoto, Y. Yokoyama, T. Ichitsubo, H. Kimura, E. Matsubara, and A. Inoue, “Precipitation of the ZrCu B2 phase in $\text{Zr}_{50}\text{Cu}_{50-x}\text{Al}_x$ ($x = 0, 4, 6$) metallic glasses by rapidly heating and cooling,” *J. Mater. Res.*, vol. 25(4), pp. 793–800, 2010.
- [124] N. Barekar, P. Gargarella, K. Song, S. Pauly, U. Kühn, and J. Eckert, “Effect of Al and Ag addition on phase formation, thermal stability, and mechanical properties of Cu-Zr-based bulk metallic glasses,” *J. Mater. Res.*, vol. 26(14), pp. 1702–1710, 2011.
- [125] B. B. Sun, Y.B. Wang, J. Wen, H. Yang, M.L. Sui, Q.J. Wang and E. Ma., “Artifacts induced in metallic glasses during TEM sample preparation,” *Scr. Mater.*, vol. 53(7), pp. 805-809, 2005.
- [126] M. Chen, “Mechanical Behavior of Metallic Glasses: Microscopic Understanding of Strength and Ductility,” *Annu. Rev. Mater. Res.*, vol. 38, pp. 445-469, 2008.
- [127] H. Choi-Yim, R. Busch, U. Köster, and W. L. Johnson, “Synthesis and

- characterization of particulate reinforced $Zr_{57}Nb_5Al_{10}Cu_{15.4}Ni_{12.6}$ bulk metallic glass composites,” *Acta Mater.*, vol. 47(8), pp. 2455-2462, 1999.
- [128] D. C. Hofmann, J.Y. Suh, A. Wiest, G. Duan, M.L. Lind, M.D. Demetrious and W.L. Johnson., “Designing metallic glass matrix composites with high toughness and tensile ductility,” *Nature*, vol. 451, no. 7182, pp. 1085–1089, 2008.
- [129] M. M. Khan, A. Nemati, Z. U. Rahman, U. H. Shah, H. Asgar, and W. Haider, “Recent Advancements in Bulk Metallic Glasses and Their Applications: A Review,” *Crit. Rev. Solid State Mater. Sci.*, vol. 43, no. 3, pp. 233–268, 2018.
- [130] K. K. Song, D. Y. Wu, S. Pauly, C. X. Peng, L. Wang, and J. Eckert, “Thermal stability of B2 CuZr phase, microstructural evolution and martensitic transformation in Cu-Zr-Ti alloys,” *Intermetallics*, vol. 67, pp. 177–184, 2015.
- [131] A. Takeuchi and A. Inoue, “Classification of bulk metallic glasses by atomic size difference, heat of mixing and period of constituent elements and its application to characterization of the main alloying element,” *Mater. Trans.*, vol. 46(12), p. 2817, 2005.
- [132] U. E. Klotz, C. Liu, P. J. Uggowitzer, and J. F. Löffler, “Experimental investigation of the Cu-Ti-Zr system at 800 °C,” *Intermetallics*, vol. 15(12), p. 1666-1671, 2007.
- [133] O. Taguchi, Y. Iijima, and Ken-ichi Hirano, “Reaction diffusion in the CuZr system,” *J. Alloys Compd.*, vol. 215, no. 1–2, pp. 329–337, 1994.
- [134] H. C. Sun, Z. Ning, G. Wang, W. Liang, S. Pauly, Y. Huang, S. Guo, X. Xue and J. Sun., “In-situ tensile testing of ZrCu-based metallic glass composites,” *Sci. Rep.*, vol. 8, no. 1, pp. 1–12, 2018.
- [135] W. L. Johnson, “Thermodynamic and kinetic aspects of the crystal to glass transformation in metallic materials,” *Progress in Materials Science*. vol. 30(2), pp.81-134, 1986.
- [136] X. L. Bian G. Wang, H.C. Chen, L. Yan, J.G. Wang, Q. Wang, P.F. Hu, J.L. Ren, K.C. Chan, N. Zheng, A. Teresiak, Y.L. Gao, Q.J. Zhai, J. Eckert, J. Beadsworth,

- K.A. Dahmen and P.K. Liaw., “Manipulation of free volumes in a metallic glass through Xe-ion irradiation,” *Acta Mater.*, vol. 106, pp. 66-77, 2016.
- [137] M. M. Trexler and N. N. Thadhani, “Mechanical properties of bulk metallic glasses,” *Progress in Materials Science*. vol. 55(8), pp. 759-839, 2010.
- [138] E. Ma, “Tuning order in disorder,” *Nature Materials*. vol. 14(6), pp. 547, 2015.
- [139] J. S. Kyeong, D. H. Kim, J. I. Lee, and E. S. Park, “Effects of alloying elements with positive enthalpy of mixing in Mg₆₅Cu₂₅Gd₁₀ bulk-forming metallic glasses,” *Intermetallics*, vol. 31, pp. 9-15, 2012.
- [140] S. Schmitz, W. Löser, H. Klauß, and B. Büchner, “Effect of elements with positive enthalpy of mixing on mechanical properties of bulk metallic glasses,” in *Journal of Alloys and Compounds*, vo. 509, pp. S131-135, 2011.
- [141] K. Jin and J. F. Löffler, “Bulk metallic glass formation in Zr-Cu-Fe-Al alloys,” *Appl. Phys. Lett.*, vol. 86(24), pp. 241-909, 2005.
- [142] X. Wang, Q. Cao, Y. Chen, K. Hono, C. Zhong, Q. Jiang, X. Nie, L. Chen, X. Wang, J. Jiang, “A plastic Zr-Cu-Ag-Al bulk metallic glass,” *Acta Mater.*, vol. 59(3), pp.1037-1047, 2011.
- [143] Z. Chen, J. Gao, Y. Wu, H. Wang, X. Liu, and Z. Lu, “Alloying effects of the elements with a positive heat of mixing on the glass forming ability of Al-La-Ni amorphous alloys,” *Sci. China Physics, Mech. Astron.*, vol. 57(1), pp.122-127, 2014.
- [144] Q. S. Zhang, W. Zhang, and A. Inoue, “Ni-free Zr-Fe-Al-Cu bulk metallic glasses with high glass-forming ability,” *Scr. Mater.*, vol.61(3), pp.241-244, 2009.
- [145] J. Zhang and Y. Zhao, “Formation of zirconium metallic glass,” *Nature*, vol. 430(6997), pp.332, 2004.
- [146] S. S. Chen and I. Todd, “Enhanced plasticity in the Zr-Cu-Ni-Al-Nb alloy system by in-situ formation of two glassy phases,” *J. Alloys Compd.*, vol. 646, pp. 973-977, 2015.
- [147] T. Wang, Y. Wu, J. Si, Y. Liu, and X. Hui, “Plasticizing and work hardening in phase

- separated Cu-Zr-Al-Nb bulk metallic glasses by deformation induced nanocrystallization,” *Mater. Des.*, vol. 142, pp.74-82, 2018.
- [148] U. Koster, “Crystallization Kinetics in Metallic Glasses,” *Key Eng Mater*, vol. (97), pp. 233-239, 1986.
- [149] D. W. Henderson, “Thermal analysis of non-isothermal crystallization kinetics in glass forming liquids,” *J. Non. Cryst. Solids*, vol. 30(3), pp.301-315, 1979.
- [150] L. C. Zhang, J. Xu, and J. Eckert, “Thermal stability and crystallization kinetics of mechanically alloyed TiC/Ti-based metallic glass matrix composite,” *J. Appl. Phys.*, vol. 100(3), 2006.
- [151] L. M. Zou, Y. H. Li, C. Yang, S. G. Qu, and Y. Y. Li, “Effect of Fe content on glass-forming ability and crystallization behavior of a $(\text{Ti}_{69.7}\text{Nb}_{23.7}\text{Zr}_{4.9}\text{Ta}_{1.7})_{100-x}\text{Fe}_x$ alloy synthesized by mechanical alloying,” *J. Alloys Compd.*, vol. 553, pp.40-47, 2013.
- [152] V. R. V Ramanan and G. E. Fish, “Crystallization kinetics in Fe-B-Si metallic glasses,” *J. Appl. Phys.*, vol. 53(3), pp.2273-2275, 1982.
- [153] G. Kumar, T. Ohkubo, T. Mukai, and K. Hono, “Plasticity and microstructure of Zr-Cu-Al bulk metallic glasses,” *Scr. Mater.*, vol. 57(2), pp.173-176, 2007.
- [154] S. Guo and C. T. Liu, “Phase stability in high entropy alloys: Formation of solid-solution phase or amorphous phase,” *Prog. Nat. Sci. Mater. Int.*, vol. 21(6), pp.433-446, 2011.
- [155] Z. P. Lu and C. T. Liu, “Glass formation criterion for various glass-forming systems,” *Phys. Rev. Lett.*, vol. 91 pp. 115505 2003.
- [156] D. Cao, Y. Wu, X. J. Liu, H. Wang, X. Z. Wang, and Z. P. Lu, “Enhancement of glass-forming ability and plasticity via alloying the elements having positive heat of mixing with Cu in $\text{Cu}_{48}\text{Zr}_{48}\text{Al}_4$ bulk metallic glass,” *J. Alloys Compd.*, vol. 777, pp. 382–391, 2019.
- [157] G. Cao, K. Liu, G. Liu, H. Zong, H. Bala, and B. Zhang, “Improving the glass-forming ability and the plasticity of Zr-Cu-Al bulk metallic glass by addition of Nb,”

- J. Non. Cryst. Solids*, vol. 513, pp. 105–110, 2018.
- [158] F. Spaepen, “A microscopic mechanism for steady state inhomogeneous flow in metallic glasses,” *Acta Metall.*, vol. 25(4), pp. 407-415, 1977.
- [159] M. Heggen, F. Spaepen, and M. Feuerbacher, “Creation and annihilation of free volume during homogeneous flow of a metallic glass,” *J. Appl. Phys.*, vol. 97(3), 2005.
- [160] A. van den Beukel and J. Sietsma, “The glass transition as a free volume related kinetic phenomenon,” *Acta Metall. Mater.*, vol.38(3), pp. 383-389, 1990.
- [161] P. Tuinstra, P. A. Duine, J. Sietsma, and A. van den Beukel, “The calorimetric glass transition of amorphous Pd₄₀Ni₄P₂₀,” *Acta Metall. Mater.*, vol.43, pp. 2815, 1995.
- [162] K. K. Song, P. Gargarella, S. Pauly, G. Z. Ma, U. Kühn, and J. Eckert, “Correlation between glass-forming ability, thermal stability, and crystallization kinetics of Cu-Zr-Ag metallic glasses,” *J. Appl. Phys.*, vol. 112, p. 6, 2012.
- [163] M. E. Launey, J. J. Kruzic, C. Li, and R. Busch, “Quantification of free volume differences in a Zr₄₄Ti₁₁Ni₁₀Cu₁₀Be₂₅ bulk amorphous alloy,” *Appl. Phys. Lett.*, vol.91(5), 2007.
- [164] L. M. Martinez and C. A. Angell, “A thermodynamic connection to the fragility of glass-forming liquids,” *Nature*, vol.410(6829), pp. 663, 2001.
- [165] S. Mandal and A. J. Kailath, “Enhanced Plasticity of Cu-Zr-Ti Bulk Metallic Glass and Its Correlation with Fragility,” *Metall. Mater. Trans. A Phys. Metall. Mater. Sci.*, vol. 50, no. 1, pp. 199–208, 2019.
- [166] Dong, Q., Y.J. Pan, J. Tan, X.M. Qin, C.J. Li, P. Gao, Z.X. Feng, M. Calin and J. Eckert. “A comparative study of glass-forming ability, crystallization kinetics and mechanical properties of Zr₅₅Co₂₅Al₂₀ and Zr₅₂Co₂₅Al₂₃ bulk metallic glasses,” *J. Alloys Compd.*, vol. 785, pp. 422–428, 2019.

